BOUNDARY CONDITION ASSESSMENT AND GEOMETRICAL ACCURACY ENHANCEMENT FOR COMPUTATIONAL HAEMODYNAMICS

MICHAEL EDWARD MCELROY

A thesis submitted in partial fulfilment of the requirements of the Manchester Metropolitan University for the degree of Doctor of Philosophy

Division of Mechanical Engineering

School of Engineering

The Manchester Metropolitan University

March 2017

ABSTRACT

Cardiovascular diseases cause over 47 % of all deaths in Europe each year. Computational fluid dynamics provides the research community with a unique opportunity to investigate cardiovascular diseases with the intent of enabling optimised, patient-specific medical therapies. Incorporating physiologically accurate geometries and boundary conditions into computational fluid dynamics simulations can be difficult tasks and are a concern for researchers. This thesis analyses the impact various inlet and outlet boundary conditions can have on the outcome of a simulation. It also presents a novel, semi-automated process that prepares accurate geometrical models for haemodynamic simulations.

Firstly, rabbit and human aorta models were used to analyse the impacts of boundary conditions on haemodynamic metrics used for understanding cardiovascular disease pathology. Comparisons were made between traction free, Murray's Law, three-element Windkessel, and Murray's Law/*in vivo* data hybrid outlet boundary conditions. Steady-state, transient, fully-developed and plug-type inlet boundary conditions were also investigated. Results showed that when advanced models such as the three-element Windkessel are unavailable, the Murray's Law based outlet returns the most physiologically accurate haemodynamics. Results also showed that prescribing a transient simulation and a fully-developed flow at the inlet are not required when the focus is only on the flow within the aorta and around the intercostal branches.

Secondly, a sensitivity test was conducted on the simulation of Left Ventricular Assistive Device (LVAD) configurations. The effects of flow ratios between the LVAD and aortic root on haemodynamic metrics were quantified. The general irregular sensitivity of the subclavian and carotid arteries to flow ratios indicates that the perfusion and wall shear stress-based haemodynamic metrics within these arteries cannot be accurately predicted unless the flow ratios are incorporated into the preoperative planning of the optimal LVAD configuration.

Finally, a semi-automated reconstruction process combining magnetic resonance angiography and optical coherence tomography data was developed. The process was successful in its ability to create an accurate geometry in a relatively short time. This forms the foundation on which more sophisticated methods can be developed.

ACKNOWLEDGEMENTS

I dedicate this thesis to my parents

for their support and encouragement throughout my journey

TABLE OF CONTENTS

LIST OF FIGURES

LIST OF TABLES

NOMENCLATURE

Symbols

$\vec{\tau}_W$	Wall shear stress vector, Pa
$\dot{m}$	Mass flow rate, kg·s⁻¹
Δt	Timestep size, s
C	Compliance of proximal vessels, m⁴·s²·kg⁻¹
D	Diameter, m
p	Pressure, Pa
P_n	Pressure recalculated for each outlet to be assigned as a boundary condition value at the start of the subsequent coefficient loop, Pa
P_{n-1}	Corresponding boundary pressure read from the end of the previous timestep, Pa
Q_n	Corresponding boundary volumetric flow rate read from the end of the current coefficient loop, m³·s⁻¹
Q_{n-1}	Corresponding boundary volumetric flow rate read from the end of the previous timestep, m³·s⁻¹
r	Radius, m
R_d	Distal vessel resistance, kg·m⁻⁴·s⁻¹
R_p	Proximal vessel resistance, kg·m⁻⁴·s⁻¹
T	Duration of cardiac cycle, s
t	Time, s
$\boldsymbol{u}$	Velocity vector, m·s⁻¹
u	Velocity, m·s⁻¹
α	Womersley number, -
β	Anastomosis azimuthal angle, °
δ	Distance from anastomosis to the innominate artery, m
μ	Dynamic viscosity, Pa·s, N·s·m⁻², kg·m⁻¹·s⁻¹

Φ   Inclination angle, º

Acronyms

AAo	Ascending Aorta
AR	Aortic Root
BC	Boundary Condition
CAD	Computer-Aided Design
CFD	Computational Fluid Dynamics
CPB	Cardiopulmonary Bypass
CPU	Central Processing Unit
CT	Computed Tomography
CTA	Computed Tomographic Angiography
CVD	Cardiovascular Disease
DAo	Descending Aorta
DICOM	Digital Imaging and Communications in Medicine
HF	Heart Failure
IGES	Initial Graphics Exchange Specification
IVUS	Intravascular Ultrasound
LAD	Left Anterior Descending coronary artery
LCCA	Left Common Carotid Artery
LDL	Low Density Lipoprotein
LSA	Left Subclavian Artery
LVAD	Left Ventricle Assist Device
LVAD/AR-FR	Left Ventricle Assist Device to Aortic Root Flow Ratio
ML	Murray's Law
MRA	Magnetic Resonance Angiography
MRI	Magnetic Resonance Imaging
OCT	Optical Coherence Tomography

OSI	Oscillatory Shear Index
PC-MRI	Phase-Contrast-Magnetic Resonance Imaging
RCCA	Right Common Carotid Artery
RRT	Relative Residence Time
RSA	Right Subclavian Artery
STL	STereoLithography file format
TAFR	Time-Averaged Flow Rate
TAo	Thoracic Aorta
TAV	Time-Averaged Velocity
TAWSS	Time-Averaged Wall Shear Stress
VBA	Visual Basic Applications
VMTK	Vascular Modelling Toolkit
VTP	Visualisation Toolkit Polygonal Data
WSS	Wall Shear Stress

Terms

Anastomosis	A connection made surgically between adjacent blood vessels or artificial vascular grafts.
Atheroma	Degeneration of arterial walls caused by accumulated fat deposits.
Atherosclerosis	Disease of the arteries characterised by the deposition of fatty material within the intima.
Boundary Condition	A parameter which describes the physiological conditions (haemodynamic or structural) acting at the boundaries of a modelled segment, representing the interaction of the model with its distal compartments.
DICOM	Digital Imaging and Communications in Medicine is a standard for handling, storing, printing, and transmitting information in medical imaging.

16

Fourier Series	A way to represent a function as the sum of a number of simple sine waves.
Haemodynamic metrics	A physical phenomenon which is derived from haemodynamics in order to comprehend physiological impact of haemodynamics.
Haemodynamics	The flow of blood.
Heart Failure	Failure of the heart to pump blood effectively.
Hyperlipidemia	An abnormally high concentration of fats or lipids in the blood.
In vitro	A process performed outside a living organism.
In vivo	A process performed within a living organism.
Intima	The innermost layer of a vein or artery.
Ischemia	An inadequate blood supply to an organ or part of the body.
Isosurfaces	A surface that represents a constant value of a variable within a volume of space.
Isothermal	Temperature remains constant in the system.
LDL	A class of lipoproteins of relatively low density, the main function of which is to transport cholesterol to tissues.
Lumen	The inside space of an artery.
Malperfusion	An unusual form of perfusion.
Monocyte	A large white blood cell, as part of the immune system.
Newtonian flow	A flow type in which the viscous stresses are linearly proportional to the local strain rate.
Pathology	The science of the causes and effects of diseases.
Perfusion	The passage of blood through a vessel or specific organ.
Platelet	A disc-shaped cell fragment without a nucleus, found in large numbers in blood and involved in clotting.
Segmentation	The process of medical images being converted into computer representations.

Steady-State	An unvarying condition in which a physical condition is equated to a single instance.
Stenosis	The abnormal narrowing of a passage in the body.
Thrombosis	The local clotting of the blood in a part of the circulatory system.
Thrombus	A blood clot formed within the vascular system of the body and impeding blood flow.
Traction Free	In terms of boundary condition, it is similar to assuming the vessel is cut and exposed to atmospheric conditions.
Transient	A time-dependent simulation that simulated the entire cardiac cycle.
Truncate	To shorten or reduce something. In the computer aided cardiovascular reconstruction process, this refers to the omitting of the downstream arterial tree at a certain point in the cardiovascular system.
Womersley Number	A dimensionless number in biofluid mechanics to express the relationship between pulsatile frequency and viscous effects of the flow.
Zero pressure	In terms of boundary condition, it is similar to assuming the vessel is cut and exposed to atmospheric conditions.

Software Packages

ANSYS-CFX Version 15.0 & 17.1 (ANSYS Inc., Canonsburg, PA, USA) - A computational fluid dynamics software package, specifically for fluid flow.

ANSYS-Fluent Version 15.0 & 17.1 (ANSYS Inc., Canonsburg, PA, USA) - A computational fluid dynamics software package, able to model a variety of physics including flow and heat transfer.

ANSYS-ICEM CFD Version 14.5 (ANSYS Inc., Canonsburg, PA, USA) - A software package used for CAD and mesh generation.

ANSYS-Meshing Version 15.0 & 17.1 (ANSYS Inc., Canonsburg, PA, USA) - A software package which is able to perform complex meshing processes in preparation for computational fluid dynamic simulations.

ANSYS-Post Version 15.0 & 17.1 (ANSYS Inc., Canonsburg, PA, USA) - A software package for post-processing simulation results, it is capable of producing variable contours, streamlines, amongst various other types of images and data tables.

Ensight Version 10.1.6 (CEI Inc., Research Triangle Park, NC, USA) - An advanced software package for post-processing simulation results, it is capable of producing variable contours, streamlines, amongst various other types of images and data tables. Python scripts can be used with this package to incorporate user defined functions.

QAngio XA 3D by Medis (Leiden, Netherlands) - Analytical software solution for the reconstruction of a coronary artery from two angiographic projections at least 25 degrees apart, either from a biplane acquisition or from two monoplane acquisitions.

QCU-CMS by Medis (Leiden, Netherlands) – A computer programme that enables quantification of intravascular ultrasound and optical coherence tomography studies through the semi-automated detection of the lumen, stent, and vessel contours.

SOLIDWORKS 2016 (SOLIDWORKS Corp. Concord, MA) - A solid modelling computer-aided design and computer-aided engineering computer program.

Vascular Modeling Toolkit (VMTK) (http://www.vmtk.org/) - A collection of libraries and tools for 3D reconstruction, geometric analysis, mesh generation and surface data analysis for image-based modelling of blood vessels.

Programming Languages

Fortran   A high-level (closer to human language and further from machine language) computer programming language used especially for scientific calculations.

Python   A high-level (closer to human language and further from machine language) general-purpose programming language.

VBA   A programming language developed by Microsoft that allows the creation of user-defined functions and the automation of specific computer processes and calculations.

CHAPTER 1

INTRODUCTION

1.1 Overview of the Chapter

A brief overview of, i) relevant Cardiovascular Diseases (CVDs), ii) how Computational Fluid Dynamics (CFD) is used to understand CVD pathology and iii) the processes commonly undergone during the CFD process to simulate haemodynamics and the particulars of making CFD useful for understanding CVDs will be outlined within the introduction. More detailed and specific introductions and justifications for the aims and objectives of this thesis will be given in their corresponding chapters, as the issues addressed in each chapter significantly differ enough to justify splitting the introductions and justifications of the work into their corresponding chapters.

1.2 Cardiovascular Disease Pathology

CVD causes over 4 million (47 %) of all deaths in Europe each year [1]. Common examples of CVD include angina, myocardial infarction, peripheral vascular disease, stroke and Heart Failure (HF) [2]–[5]. Currently the main pathologies of concern in CVDs are atherosclerosis and thrombosis, and there is potential to assist more patients if these problems can be eliminated [6]. Therefore, from a clinical point of view, assessment of these CVDs potentially plays a key role in choosing one medical device or therapy over another for an individual patient [7]. Before approaching the work undertaken in this thesis, it is first important to gain a broad understanding of relevant CVD pathologies. The main CVDs of concern within each chapter of this thesis include atherosclerosis and thrombosis, each of these CVDs will now be briefly described separately.

1.2.1 Atherosclerosis

Atherosclerosis is the build-up of fatty substances, such as cholesterol within the wall of arteries and is known as a fundamental cause of CVDs [8]. These fatty substances are often referred to as plaque or atheroma. Plaque causes the affected arteries to narrow (known as a stenosis), which creates higher velocities around the stenosis and hence activates platelets and induces thrombosis [9], [10]. This process can ultimately cause a fatal lack of blood flow to the heart and brain [8], [10]. The formation of atheroma begins when Low Density Lipoprotein (LDL) in the bloodstream passes through the endothelial layer within the vessel wall and accumulates between the intima and media layer. The

accumulation is dependent on the concentration of LDL in the bloodstream and the condition of the endothelium. Whilst between the intima and media layer, the LDL oxidises, oxidised LDL is toxic and causes inflammation. Monocytes respond by engulfing the oxidised LDL and become foam cells. When the foam cells die, they release their lipid content, creating what is known as a lipid core or plaque. As this sequence repeats itself, the plaque increases in size, ultimately protruding into the lumen, hence reducing the artery's cross-sectional area [11]. A patient is at increased risk of suffering from atherosclerosis if they have hypertension, smoking habits, hyperlipidemia, diabetes, social stress, a sedentary lifestyle, or a viral infection [12].

Atherosclerosis development is known to be associated with local flow conditions as well as biological factors (LDL behaviour etc), with plaques most frequently developing in close proximity to bifurcation sites [13], [14]. This thesis will focus on the local haemodynamic effects on atherosclerosis and ignore the effects of the biological factors, as they are not within the scope of this work. In terms of local flow conditions, low and oscillatory endothelial shear stress is widely accepted to be associated with atherosclerosis development [15]–[19]. This theory will be used as a basis of analysing performance throughout the thesis.
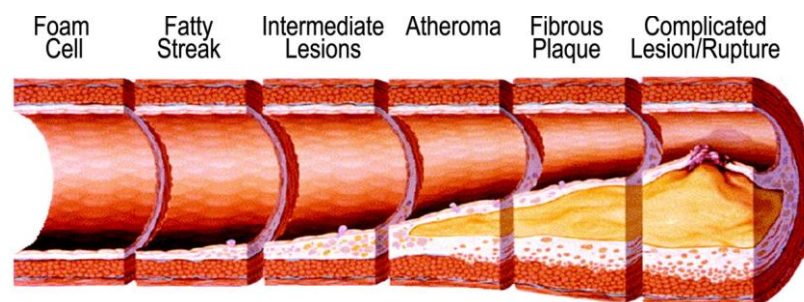
Figure 1.1 – Illustration of the development of atherosclerosis within an artery, this image has been adapted from Koenig et al [20].

1.2.2 Thrombosis

Thrombosis is the formation of a blood clot (thrombus) within the cardiovascular system, it involves the adherence of circulating platelets to sites of endothelial injury or atherosclerotic plaque rupture [8], [21]. Arterial thrombosis is a potentially fatal condition as it can lead to ischemic attacks, strokes, neurological events, heart attacks and impairment of kidney and liver function [21]–[25]. Thrombosis can be characterised by the Virchow's triad: the nature of the surface, the condition of the blood and the local flow conditions [7]. Similarly to atherosclerosis, this thesis will again focus on the local flow conditions and ignore the other two aspects of Virchow's triad, as they are not within

the scope of this work. In terms of flow conditions, it is widely believed that slow, stagnant or recirculating flow and low shear stresses promote thrombosis [26], [27].
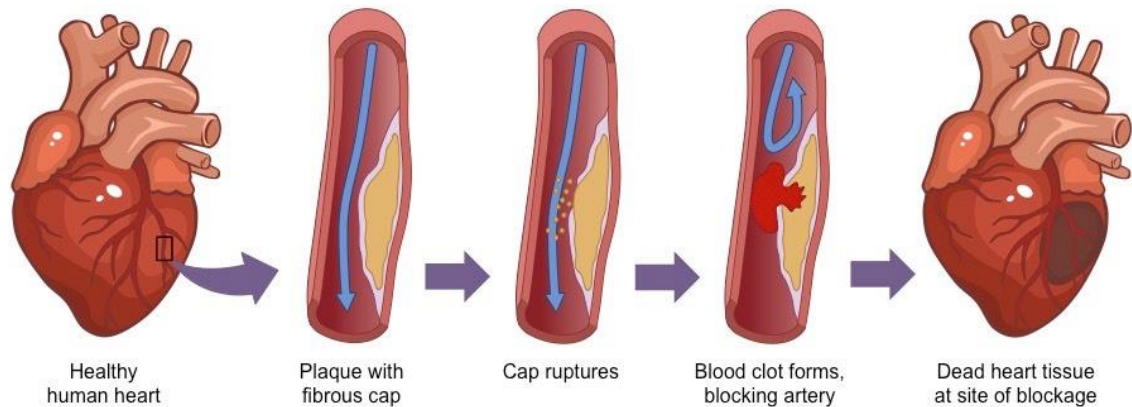
Figure 1.2 – Illustration of the development of a thrombus within a coronary artery, leading to a myocardial infarction [28].

1.3   Cardiovascular Diseases and CFD

Simulating blood flow through the use of patient-specific imaging began in the late 1990s [29]–[31]. Advances in vascular biology, biomechanics, medical imaging and computational techniques including CFD have provided the research community with a unique opportunity to investigate diseases and complications of carotid arteries [32], [33], coronary arteries [34], the aorta [35], aortic dissections [36]–[38], cerebral circulation [39]–[41] and aneurysms [42]. The implementation of CFD also now plays an important role in the development of medical devices [43]. The increasing power-to-cost ratio of computers and the advent of methods for subject-specific modelling of cardiovascular mechanics have made CFD-based modelling sometimes even more reliable than methods based solely on *in vivo* or *in vitro* measurements [44].

In the application of investigating CVD pathology, the process of performing CFD analysis will now be briefly described:

Problem Definition. The goals of an investigation and the subsequent area of interest within the cardiovascular system is defined.

Geometry Construction. Once the area of interest is defined, the patient is usually subjected to 3D Magnetic Resonance Imaging (MRI), Computed Tomography (CT) or ultrasound in order to obtain raw geometrical data [43]. The DICOM file type is usually made up of many slices of cross-sections of the area of interest taken in the X, Y and Z planes. This file is used as a basis to create a 3D volume using advanced reconstruction algorithms. Vascular Modeling Toolkit (VMTK) (http://www.vmtk.org/) offers a variety

of advanced reconstruction algorithms that are able to differentiate between the contrast of neighbouring volume cells within the DICOM data. These algorithms are able to detect boundaries between high and low contrast volume cells and replace the boundaries with surfaces. These surfaces are then manipulated to represent the area of interest. This is a semi manual process that ultimately produces a surface mesh which is checked for possible errors, corrected, and then exported as an STL file type. The STL file is then reverse engineered in a CAD package to produce a clean (more effective for CFD simulations) geometry file. The IGES file is the preferred final file type as it allows for the geometry to be easily manipulated to incorporate medical devices such as bypass grafts etc.

Mesh Generation. The geometrical file (IGES) is then imported into the programme 'ANSYS-Meshing (ANSYS Inc., Canonsburg, PA, USA)', where various meshing techniques can be implemented to create an adequate mesh for the problem at hand.

Boundary Conditions. During the geometrical reconstruction process, the arterial tree is truncated. This means that at certain locations in the geometry, a cut is made to omit the downstream (or upstream if it will represent an inlet) vessels. This cut is then replaced with a plane which represents the cross-section of the lumen at that location. This surface will later be prescribed a realistic Boundary Condition (BC). This process is performed to simplify the geometry and constrain the fluid domain to the area of interest, as including unnecessary vessels in the geometry will increase computational demand with no true benefit. Each truncation point needs to be prescribed a velocity or pressure value. A steady or pulsatile velocity is usually defined at the inlet depending on the requirements of the problem. Ideally, a patient-specific flow rate will enable an accurate velocity waveform to be applied at the inlet. The acquisition of patient-specific inlet and outlet BCs can often be difficult in cardiovascular problems due to the sparsity of relevant data. When patient-specific data is sparse, often a generic zero pressure is applied to the outlet boundary, this is however limited in its ability to represent realistic haemodynamics. Therefore, more advanced methods can be implemented in replacement of patient-specific flow rates or pressure (which will be described in detail in Section 1.4).

The aforementioned BCs are prescribed during the pre-processing stage and are inputted into the pre-processor ANSYS-CFX Version 17.1 (ANSYS Inc., Canonsburg, PA, USA) or ANSYS-Fluent Version 17.1 (ANSYS Inc., Canonsburg, PA, USA).

Solving Method. Following the above steps, the computer is then left to run the simulation using a relevant solution scheme. During this time, the computer attempts to

come to an approximate solution of the governing fluid flow equations (Navier-Stokes). Time for the solving process to finish can vary significantly depending on various factors. These factors often include, i) whether the simulation is steady-state or transient, ii) the number of elements included in the mesh, iii) the computational power of the machine the simulation is running on, iv) whether the simulation is run on one Central Processing Unit (CPU) or multiple, v) the number of cardiac cycles accounted for in a transient simulation, vi) the number of coefficient loops within each timestep, and vii) the convergence criteria.

Post-Processing. A result file is produced once the simulation is completed. This results file is imported into a post-processing package, such as ANSYS-Post (ANSYS Inc., Canonsburg, PA, USA) or Ensight 10.1.6 (CEI Inc., Research Triangle Park, NC, USA) to allow images and data to be extracted for analysis.

1.4   Proposed Methodology

In this section, specific methods that are used frequently throughout the thesis are described in more depth. This will provide the reader with a broad understanding of the processes undergone during each project. Some processes outlined in Section 1.3 will be omitted from this section as they are better described in their corresponding chapters.

1.4.1   CFD Solver

During CFD simulations, the computer aims to solve the equations which govern fluid flow at each node within the mesh. In both steady-state and transient simulations, blood flow is defined as a three-dimensional, incompressible, isothermal, Newtonian and laminar flow. In reality, blood is a non-Newtonian fluid, which must be accounted for when investigating small vessels. However, it is often neglected when investigating haemodynamics within larger vessels where the effects are less prominent [45]. The Navier-Stokes equations are used as the basis for most CFD problems [46].

In the CFD simulations in this thesis, the blood flow is defined as a three-dimensional, incompressible, isothermal, Newtonian and laminar flow, whose governing equations are:

Continuity equation,

$$\nabla \cdot \boldsymbol{u} = 0$$

(1.1)

and Navier–Stokes equation,

$$\rho \frac{\partial \boldsymbol{u}}{\partial t} + \rho(\boldsymbol{u} \cdot \nabla)\boldsymbol{u} = -\nabla p + \mu \nabla^2 \boldsymbol{u}$$

<div align="right">(1.2)</div>

where $\boldsymbol{u}$ is the velocity vector, t is the time, p is pressure, μ is the dynamic viscosity, and ρ is the density of the blood.

The governing fluid dynamics equations are solved numerically using a hybrid finite-element/finite-volume code (ANSYS-CFX-Version 15.0), using a fully implicit second-order backward Euler differencing scheme. The convergence criterion (a normalised residual, obtained based on the imbalance in the linearised system of discrete equations) is set to 10^{-6} in this study. A commercial visualisation tool, Ensight 10.1.6 was used to post-process the results.

1.4.2   Steady-State vs Transient Simulations

Throughout the thesis, both steady-state and transient cases are used to investigate haemodynamics. Steady-state simulations are equivalent to a snapshot of the flow, thus making the solving process much simpler and quicker. The BCs needed to be implemented during a steady-state simulation are also often much simpler than in a transient case.

Transient simulations offer the benefit of being able to capture the haemodynamics throughout the entire cardiac cycle. A Fourier series transform is used to represent the pulsatile velocity inlet of the model and is implemented into the pre-processing stage of CFD, this is known as a transient or pulsatile velocity profile. The cardiac cycle is then split up into a number of timesteps, approximately 800 timesteps per cardiac cycle can be expected typically. The computer solves the governing equations at each timestep, once the convergence criteria or an iteration threshold is reached, the solver moves to the next timestep until the simulation is finished.

Transient simulations present significant benefits compared to steady-state simulations as they are able to capture important flow characteristics that are otherwise unavailable in steady-state simulations. More advanced haemodynamic parameters such as Time-Averaged Wall Shear Stress (TAWSS) and Oscillatory Shear Index (OSI) are also able to be extracted from a transient simulation, which is otherwise impossible for steady-state simulations. These advanced haemodynamic parameters will be described in more detail in Section 1.4.5. The main drawback of running transient simulations, however, is the complexity of setting the simulation up and the solution time required. The simulation

time for transient simulations are often many times greater than that of steady-state simulations, depending on how many cardiac cycles are accounted for.

1.4.3   Inlet Boundary Conditions

During the geometrical reconstruction process of the area of interest, the arterial tree needs to be truncated (split at a certain point), and replaced with a flow BC. Imposing the correct BC that will represent physiological flow is important for investigating CVD pathology. Often, incorporating a fully-developed profile at the inlet and outlets is important. This can be achieved either numerically by applying a velocity profile based on an equation, or by affixing a flow extension to the inlet and outlets. This allows the flow to be fully-developed by the time it reaches the true inlet or outlet, thus creating a more realistic simulation.

1.4.4   Outlet Boundary Conditions

Appropriate truncation locations need to be positioned in the model in order to capture physiological downstream conditions whilst being efficient with the computational domain size. Outlet truncation points are usually positioned after the first few generations of large arteries [47]. The types of outlet BCs used in this thesis will now be described separately.

Traction Free. Considered one of the simplest BCs to apply in a simulation, a 'traction free' or 'zero pressure' condition is applied to each outlet individually and defined as an 'opening' to allow for flow reversal at the boundary if it occurs. This BC is used in various models due to its simplicity and when patient-specific *in vivo* measured flow rates are not readily available [43], [48], [49]. The traction free BC is similar to assuming the vessel is cut and exposed to atmospheric conditions and hence neglects the resistive effects of downstream vessels [50].

Murray's Law. Murray's Law (ML) states that flow in a vessel is proportional to the diameter of the vessel lumen cubed:

$$\dot{m} \propto D^3$$

(1.3)

This leads to the application of 'flow splits' (also known as 'flow percentage' or 'flow ratio'), referring to the percentage of flow assigned to an outlet boundary dependent on the total inlet flow rate. Murray's Law (ML) [51], [52] can substitute or be used in conjunction with incomplete *in vivo* data. Recently the prescription of flow splits has replaced the traction free (or zero pressure) outlet BC when the diameter of the vessel is

26

known or due to existing data [53]–[56]. For example, Vincent et al. [53] combined ML with *in vivo* data by Barakat et al. [57] to create a realistic simulation of haemodynamics through a complex cardiovascular geometry. The *in vivo* data comprised of measured flow rates at a portion of the total vessels included in the geometry. A percentage of the equivalent inlet mass flow rate value is assigned individually to each vessel outlet. The mass flow rate percentages are based on Eq. (1.3). The mass flow rate per outlet is converted to its velocity counterpart by accounting for the outlet cross-sectional area. This value is then assigned as a velocity normal to the boundary and defined as an 'outlet'.

Three-Element Windkessel. More advanced models can also be applied at the outlets in order to capture the resistance and compliance effects of the proximal and distal vessels in the arterial tree from corresponding outlets. The three-element Windkessel [58] has become one of the most widely used and accepted lumped parameter model of the circulatory system as it tends to produce realistic aortic pressures and flows [59], [60]. It has had particular success in the study of haemodynamics following the insertion of a Left Ventricular Assist Device (LVAD), and is still being used in the latest CFD-based cardiovascular research to date [36], [45], [59], [61]–[68]. Therefore, a three-element Windkessel model has been developed in this thesis in order to be applied to aortic simulations which are able to capture physiologically realistic haemodynamics, this method is specifically used in Chapters 3 & 4.

When the three-element Windkessel is incorporated into the simulation, the 3D domain is coupled to a three-element Windkessel model (see Figure 1.3 and Figure 1.4 for an illustration of the concept). The implementation of the three-element Windkessel is derived from Eq. (1.4) [59].

$$P_n = \frac{C \cdot P_{n-1} \cdot R_d + Q_n \cdot R_d \cdot \Delta t + Q_n \cdot R_p \cdot \Delta t + C \cdot Q_n \cdot R_d \cdot R_p - C \cdot Q_{n-1} \cdot R_d \cdot R_p}{\Delta t + C \cdot R_d} \tag{1.4}$$

Eq. (1.4) is coupled to each outlet separately, in concept, this equation essentially represents applying a zero dimensional circuit diagram to each outlet which is able to capture the resistance and compliance of the vessels in the arterial tree. Eq. (1.4) is implemented by coupling a Fortran subroutine with ANSYS CFX which is called at the end of every coefficient loop, where P_n is a pressure recalculated for each outlet and is assigned as a BC value at the start of the following coefficient loop. P_{n-1} is the corresponding boundary pressure read from the end of the previous timestep. Q_n is the corresponding boundary volumetric flow rate read from the end of the current coefficient loop. Q_{n-1} is the corresponding boundary volumetric flow rate read from the end of the

previous timestep. R_p and R_d represent proximal and distal vessel resistances respectively. The compliance (C) represents an artery's ability to store and then release flow during systole and diastole respectively, analogous to a capacitor in an electrical circuit [59], [69], [70]. Δt is the timestep size. The boundary specific resistance and compliance parameter values where obtained by *in vivo* measurements collected by La Disa et al. [63] and are given in Table 1.1.

A main subroutine is called at the end of every coefficient loop and was used for extracting the variables Q_n, Q_{n-1}, P_{n-1}, and Δt from the 3D domain and then implementing them into Eq. (1.4) to determine the P_n value for each boundary. Five values (each value for a separate outlet boundary) of P_n are then saved to text files, these files are subsequently read by five other subroutines when the solver is inputting the BCs during the subsequent coefficient loop. During the Windkessel implementation, flow rates (Q_n and Q_{n-1}) are initialised with values of zero. P_n and P_{n-1} are initialised with absolute pressures of 9.24 kPa. The reference pressure is set to 8.24 kPa.

Table 1.1 – Three-element Windkessel model parameter values for the outlet boundaries. R_p represents the proximal resistance, R_d represents the distal resistance and C represents the compliance of the proximal vessels. Values were obtained via LaDisa et al. [63] and converted into SI units.

	C ($m^4 \cdot s^2 \cdot kg^{-1}$)	R_p ($kg \cdot m^{-4} \cdot s^{-1}$)	R_d ($kg \cdot m^{-4} \cdot s^{-1}$)
Right Subclavian Artery	$9.1490 \cdot 10^{-10}$	$1.0110 \cdot 10^8$	$1.7038 \cdot 10^9$
Right Common Carotid Artery	$6.0720 \cdot 10^{-10}$	$1.5230 \cdot 10^8$	$2.5670 \cdot 10^9$
Left Common Carotid Artery	$6.0720 \cdot 10^{-10}$	$1.5230 \cdot 10^8$	$2.5670 \cdot 10^9$
Left Subclavian Artery	$7.4770 \cdot 10^{-10}$	$1.2370 \cdot 10^8$	$2.0847 \cdot 10^9$
Thoracic Aorta	$4.6231 \cdot 10^{-9}$	$2.0000 \cdot 10^7$	$3.3720 \cdot 10^8$
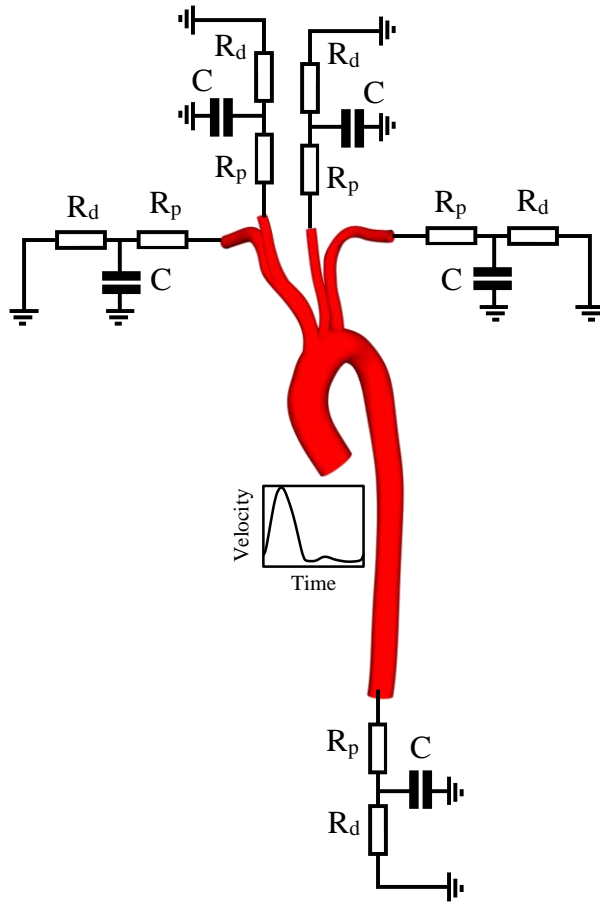
Figure 1.3 – Illustration of how the 3D domain is coupled to the three-element Windkessel model.
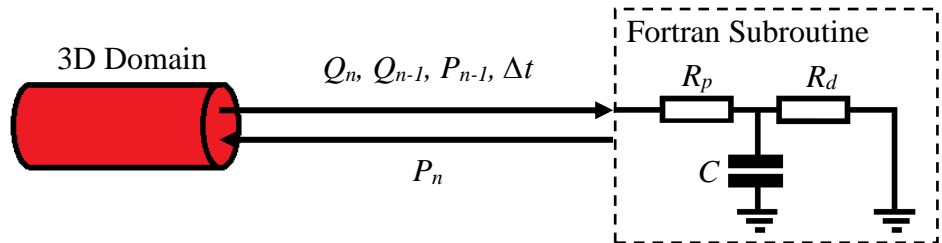
Figure 1.4 – Illustration of how the 3D domain is coupled to the 0D circuit via a Fortran subroutine.

1.4.5 Haemodynamic Metrics

The localisation of various vascular wall modifications (including atherosclerosis and thrombosis) have been extensively studied and are related to different local haemodynamic metrics [14], [71]–[76]. These haemodynamic parameters can be directly derived from the flow velocity fields obtained by CFD simulations.

A variety of haemodynamic metrics have been proposed in the literature in an attempt to associate haemodynamics with vascular wall modification [77]. However. given the

number of metrics available, it can be confusing when deciding which metrics are important to include in studies and which are redundant [77]. The parameters chosen for this thesis include WSS, TAWSS [78], OSI [78] and RRT [77], calculated according to Eqs. (1.5)-(1.8), which are the most studied and widely accepted metrics within the literature, as will be discussed later in this section.

$$WSS = \tau_w = -\mu\left(\frac{\partial u}{\partial r}\right)_{wall} \tag{1.5}$$

$$TAWSS = \frac{1}{T}\int_0^T |\vec{\tau}_w|\, dt \tag{1.6}$$

$$OSI = \frac{1}{2}\left(1 - \frac{\left|\int_0^T \vec{\tau}_w\, dt\right|}{\int_0^T |\vec{\tau}_w|\, dt}\right) = \frac{1}{2}\left(1 - \frac{|\vec{\tau}_{mean}|}{TAWSS}\right) \tag{1.7}$$

$$RRT = \frac{1}{\frac{1}{T}\left|\int_0^T \vec{\tau}_w\, dt\right|} = \frac{1}{(1 - 2\times OSI)\times TAWSS} \tag{1.8}$$

In the above equations, $\vec{\tau}_w$ is the WSS vector and T is the time period of the flow cycle.

These parameters have been chosen because, i) localised distribution of low-WSS and high-OSI strongly correlate with the locations of atheroma [78], [79], ii) platelet activation may be induced by the combination of large exposure time and high shear stress [80]–[83], iii) stagnant and recirculating flow regions can cause platelet aggregation and thrombosis [84].

Each haemodynamic metric will be discussed below separately. Each haemodynamic metric is evaluated using the commercial visualisation tool, Ensight 10.1.6 along with various Python scripts.

Wall Shear Stress. The most common haemodynamic metric, known as WSS, refers to the frictional stress exerted by the blood flow on the vessel wall [16], [71], [85]. Although pathology of atherosclerosis is complex in its nature, flow induced shear stress on the vessel wall has been identified as an essential factor in atherosclerosis development [85]. In a cohort of 22 CFD practitioners, all of the participants used WSS as a tool for assessing the risk of aneurysm rupture, hence illustrating the wide acceptance of this metric as crucial for investigating cardiovascular pathology to date [14], [86]. As shown in Eq. (1.5), the shear stress is proportional to the velocity gradient at the vessel wall and fluid viscosity.

Time-Averaged Wall Shear Stress. In most cardiovascular problems, it is important to account for the pulsatility of the blood flow as it allows true representation of the nature of haemodynamics throughout the entire cardiac cycle and allows for more advanced haemodynamic metrics to be extracted. This leads to the advent of TAWSS, which is calculated by averaging the WSS value at each node in the computational domain, as shown in Eq. (1.6) [77], [78]. Despite the benefits of TAWSS in understanding vessel wall modification, the specific relationship between TAWSS and atherosclerosis is still a topic of debate between researchers. It was first suggested that high WSS protected the vessel wall and that atherosclerotic lesions occur in regions of low WSS [87]. More recent works of Peiffer et al. [19] reviewed several papers and concluded that low WSS is in fact accepted as being related to the deposition of atherosclerotic lesions. Directly correlating TAWSS with atherosclerotic lesion deposition is however not yet considered to be a fully-robust concept, it is still currently of interest to develop more advanced relationships between haemodynamic metrics and the risk of atherosclerotic lesions [14].

Oscillatory Shear Index. A dimensionless metric which represents the changes in WSS direction has been introduced [78], [88]. This metric is calculated according to Eq. (1.7) [77]. Its value can fluctuate between 0 and 0.5, with 0 representing uni-directional flow, and 0.5 representing purely oscillatory flow over the cardiac cycle. Regions with high values of OSI have previously been suggested to coincide with early atherosclerotic lesions [89]. Furthermore, regions with low values of TAWSS usually also experience high values of OSI, due to the nature of how OSI is calculated (TAWSS is the denominator), hence the term 'low and oscillatory shear' being a common term that is used in proposed theories of regions prone to vascular modification [19]. However, this theory is not yet accepted to be completely robust, as presented in a review by Peiffer et al. [19]. Furthermore, a limit to this parameter is that it is unable to represent the magnitudes of shear stress.

Relative Residence Time. Himburg et al. [90] showed that residence time of particles near the arterial wall is proportional to a combination of TAWSS and OSI. High values of RRT have shown a strong correlation with the localisation of atherosclerotic plaque within a small cohort of mice [91]. By interpreting Eq. (1.8), it is possible to appreciate that as OSI approaches its limit of 0.5, RRT magnitude begins to increase significantly. Meaning that at sites where particles are oscillating a lot, the residence time of the particles in that region will be high, thus suggesting the potential development of atherosclerosis and thrombosis [91], [92]. This makes RRT a useful metric in studying

the effect of haemodynamics on vascular wall modification [90]. RRT has been shown to be in close correlation to TAWSS, but inverted and with a more understandable connection to the biological mechanisms underlying atherosclerosis [77], [90]. RRT is a usually a relative value, with the reference value being around the inlet of the domain where the RRT is expected to be at its lowest. Hence, it is usually normalised to provide a better understanding of the metric.

Perfusion. Perfusion is another haemodynamic metric that is important to calculate when investigating haemodynamics, particularly in the study of optimising LVAD configurations (as used in Chapter 4). A LVAD extracts blood entering the failing left ventricle, the blood passes through an axial pump and is expelled via an outflow conduit which is anastomosed to the Ascending Aorta (AAo). Perfusion to the aorta is usually unphysiological when a patient has an implanted LVAD, and hence can run the risk of ischemic attacks [93]–[96]. Ischemic stroke due to malperfusion however does tend to differ from patient to patient with an implanted LVAD, as shown in a study of 956 patients with an implanted LVAD [96]. Therefore, patient-specific optimisation of these devices is crucial to ensure adequate perfusion to all organs of each patient.
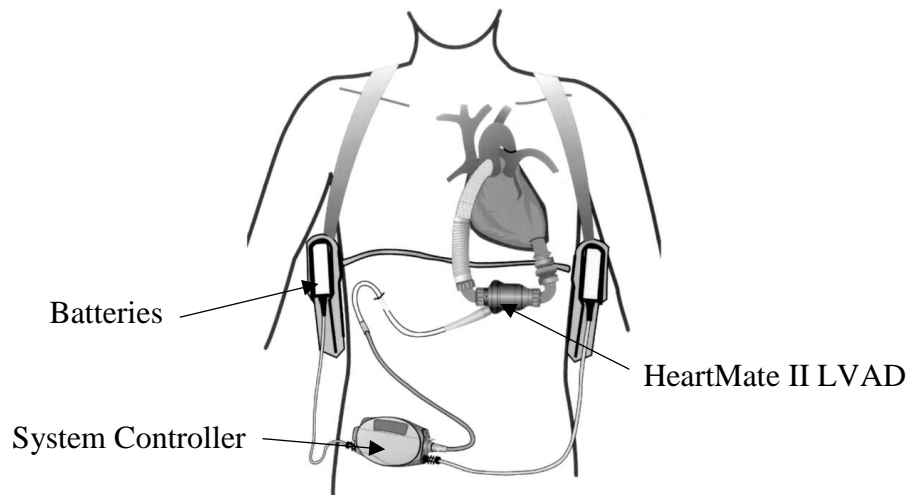
Figure 1.5 – Illustration of an implanted HeartMate II LVAD. The image is adapted from Griffith et al [97].

1.5   Aim

In the research branch of studying CVDs using CFD, two areas have been identified as being important to enhancing the understanding of CVD pathology. There is a need to better understand the impact various BCs can have on simulation results. There is also a need to improve the accuracy of coronary artery geometrical models for investigating coronary artery disease pathology. These two areas concern the need to improve CFD as

a tool to understand CVDs. Hence, the aim of this thesis is to improve CFD as a tool to understand CVDs.

1.6 Objectives

In order to achieve the aim of this thesis, it is broken down into the following four objectives:

1. Quantify the impact widely used conventional inlet and outlet BCs have on aortic haemodynamics.
2. Quantify the impact conventional and advanced outlet BCs have on aortic haemodynamics.
3. Determine whether HF severity needs to be incorporated into the preoperative planning of LVAD configurations.
4. Develop a novel geometrical reconstruction method for the accurate 3D representation of coronary arteries, which are to be used for associating haemodynamic metrics with coronary artery diseases.

1.7 Contribution to Knowledge

The main contributions to knowledge of this thesis are:

- The quantification of the impact the most widely-used inlet and outlet BCs have on various haemodynamic metrics used for predicting the localisation of CVDs within aorta models. Previous studies in the literature do not appear to present findings in a clear way for CFD practitioners to easily understand when they are deciding on the most physiologically accurate BCs to use in their simulations.
- The investigation on the necessity of incorporating heart failure severity during preoperative planning of LVAD configurations, as HF severity is often neglected in relevant studies.
- The development of a novel method of reconstructing coronary artery geometries to an accuracy that has not been achieved until now. The reconstruction is in preparation for CFD simulations to associate haemodynamic metrics with risk of atherosclerotic lesion erosion and rupture.

1.8 Organisation of Thesis

Each chapter will begin with a brief review of the relevant literature regarding the corresponding chapter and will justify the necessity of the chapter, followed by the methodology used and the results of the specific study.

Chapter 2 will begin the thesis by quantifying the impact various conventional inlet and outlet BCs have on aortic haemodynamics within a subject-specific rabbit aorta. Effects of various inlet and outlet BCs on haemodynamics have been studied in the literature, however these studies do not use such an accurate subject–specific model with corresponding *in vivo* data for validation. Nor have these studies presented the findings in a clear way for CFD practitioners to easily understand when they are deciding on the most physiologically accurate BCs to apply in their simulations.

Chapter 3 builds on the lessons learned in Chapter 2 by incorporating a more advanced outlet boundary method known as the three-element Windkessel. The parameters required to implement the three-element Windkessel model were unavailable for the rabbit aorta geometry. Therefore, the traction free, ML and three-element Windkessel based outlet methods are studied in this chapter using a patient-specific model of a 23 year old female aorta. A Fortran subroutine is developed in this chapter to enable the incorporation of the three-element Windkessel model into ANSYS-CFX.

Now that a firm understanding is in place of the most physiologically accurate outlet BCs to apply in the study of aortic haemodynamics, this knowledge is applied to further the understanding of the computational study of LVADs. Specifically, Chapter 4 investigates the necessity of incorporating HF severity during preoperative planning of LVAD configurations, as HF severity is often neglected in relevant studies.

The previous chapters focus on the impact various types of computational BCs can have on the outcome of CFD investigations of aortic CVDs. Chapter 5 shifts the focus to the accuracy enhancement of the reconstruction of coronary artery vessels for CFD simulation applications. This chapter addresses the need for more accurate geometrical reconstruction techniques in order to begin associating haemodynamic metrics with atherosclerotic rupture and thrombus development. Reconstructing such an accurate geometry has been a difficult and complex challenge to date for researchers which has not been achieved until now. A novel semi-automated and more accurate reconstruction technique is development in this chapter.

Finally, Chapter 6 ends the thesis by concluding the work studied and recommends potential future work.

CHAPTER 2

IMPACT OF CONVENTIONAL INLET/OUTLET BOUNDARY CONDITIONS ON HAEMODYNAMIC METRICS

2.1 Introduction

For over a decade, patient-specific haemodynamic modelling using CFD has grown to become an essential tool in the study of CVDs [49], [98]. The application of CFD in this area has grown motivated by both clinical and scientific needs to understand and predict CVDs associated with flow features that cannot easily be extracted via standard experimental techniques [49]. Some of the current metrics extracted from the haemodynamic flow features to predict CVD behaviour include, WSS, TAWSS, OSI and RRT [45], [46], [72], [73], [75].

With the increased use of CFD, comes a growing need to understand the impact and influence of the various inlet and outlet BCs that can be applied. The BCs are generally only clinically identifiable to a low degree of accuracy, and as such, any numerically calculated haemodynamic metric is subject to an unknown degree of certainty. In essence, without careful consideration of the sensitivity to relevant parameters to these BCs, it is difficult to draw firm conclusions from the predictive capability of these numerical tools [99]. Particular attention and research is currently paid to BCs, as they are of critical importance to the haemodynamics within the Thoracic Aorta (TAo) [43], [49], [100], [101].

Whenever possible, incorporation of fully-personalised, non-invasive *in vivo* measurements of time-dependent flow rates, flow ratios or pressure waveforms are necessary for subject-specific analysis of aortic haemodynamics [102]. However, it can be difficult to obtain these physiological measurements for the many inlets and outlets that the cardiovascular system may have [49], [103]. When this is the case, there are complex 0D or 1D methods such as the 3-Element Windkessel [104] which attempt to capture the resistance of the proximal and distal arteries of the boundary as well as the capacitance of the downstream vessels. These resistance and capacitance values are based on measured blood pressure and flow rates, however, acquiring these model parameters can be a difficult task, often due to practical difficulties in the acquisition of pressure and flow data of all required sites, or the measurement data available is insufficient for

accurately estimating these model parameters [104]. Hence, despite more reliable methods existing, it is still common amongst the cardiovascular research community to use simpler outlet BCs such as zero pressure [38], [50], [86], [105]–[109], flow ratios based on ML [86] and the combination of flow ratios based on ML and *in vivo* data [53], [56]. To put this into some perspective, during the 2013 intracranial aneurysm rupture challenge, 12 of 26 participating CFD groups defined zero pressure at all outlets, 12 applied flow splits (either arbitrary values or based on ML), whilst 2 implemented a 3-Element Windkessel model [86].

ML [51], [52] can substitute or be used in conjunction with incomplete *in vivo* data. ML states that flow in a vessel is proportional to the diameter of the vessel lumen cubed, refer to Eq. (1.3). This leads to the application of 'flow splits' (also known as 'flow percentage' or 'flow ratio'), referring to the percentage of flow assigned to an outlet boundary dependent on the inlet flow rate. Recently the prescription of flow splits have replaced the traction free (or zero pressure) outlet BC when the diameter of the vessel is known or due to existing data [53]–[56]. For example, Vincent et al. [53] combined ML with *in vivo* data by Barakat et al. [57] to create a realistic simulation of haemodynamics through a complex cardiovascular geometry.

Despite the work by Morbiducci et al. [100], Gallo et al. [102], Cito et al. [99] and those reviewed by Taylor & Figueroa [43] and Caballero [49], there appears to be a lack of a comparison between the effects of outlet BCs based on, i) zero pressure, ii) flow ratios based on ML, and iii) the combination of flow ratios based on ML and *in vivo* data using a complex aorta model.

Therefore, the objective of this chapter is to assess the impact of using the most widely-used and relatively simple to implement inlet and outlet BCs on various haemodynamic metrics used for predicting the localisation of CVDs on a complex aorta model.

2.2   Method

2.2.1   Geometrical Model

The precise geometry of a rabbit aortic arch and descending TAo is studied here (created and studied by Vincent et al. [53] and has also been used in a number of other studies [54], [56], [110]. The geometry starts from the AR (i.e., sinotubular junction) and includes the innominate, left subclavian and intercostal branches (Figure 2.1). The geometry is that of a male New Zealand white rabbit aged 18 months, weighing 3.25 kg. By studying such a complex aortic structure, one is able to gain a better understanding of the impact certain

BCs will have on the haemodynamics within similar aorta models, including the human aorta.
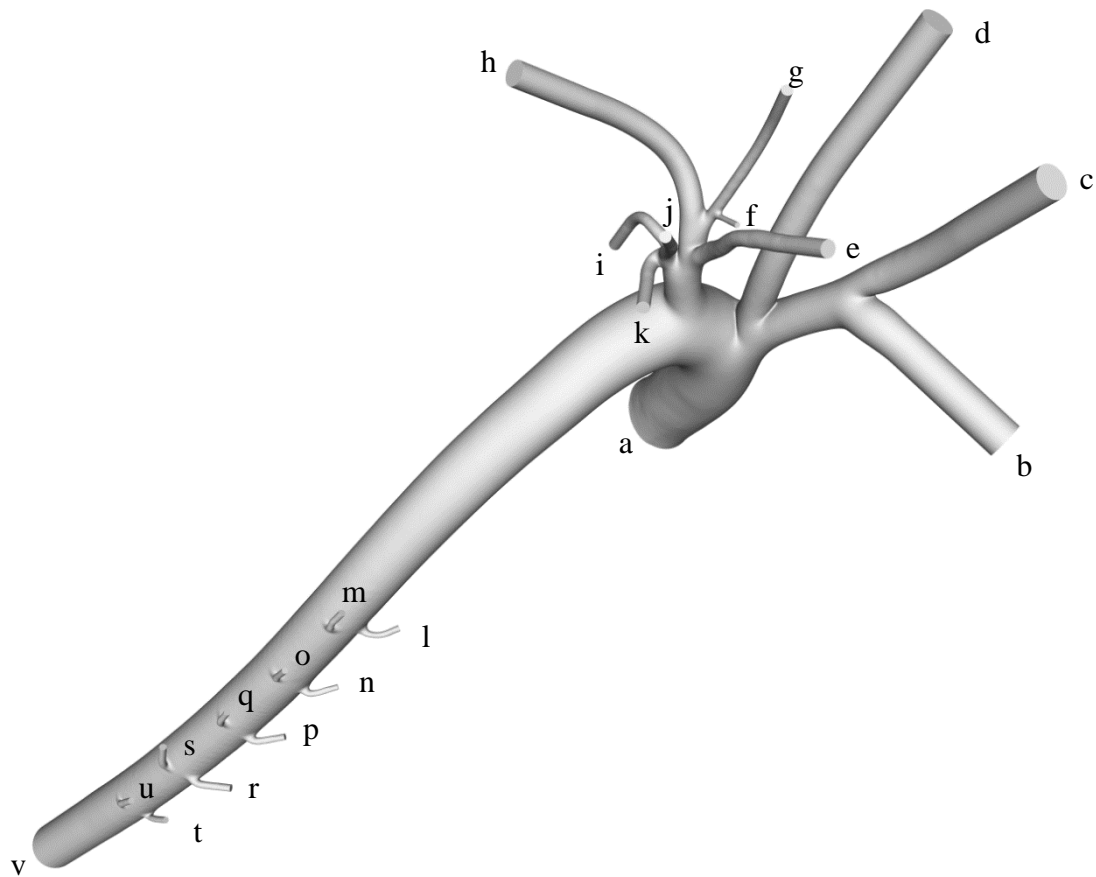
Figure 2.1 - Schematic of the present rabbit aorta configuration. (a) Inlet: AR (sinotubular junction); (b)-(d) Outlets: right subclavian, right and left common carotid arteries; (e)-(k) left subclavian arteries; (l)-(u) intercostal arteries, and (v) outlet: abdominal aorta.

2.2.2 Computational Domain

The geometry was meshed using ANSYS-ICEM CFD Version 14.5 (ANSYS Inc., Canonsburg, PA, USA). The mesh was based on a finite volume hybrid mesh consisting of tetrahedral elements within the core region and prism layers (3 elements thick) near the wall to allow for large spatial velocity gradients (see Figure 2.2). While all the meshes used in this study consists of ≈4 million elements, in the case of 'Test 4' (see Table 2.1), an extension region consisting of ≈1 million elements was affixed to the inlet of the original mesh to allow flow to fully develop.

(a)	(b)
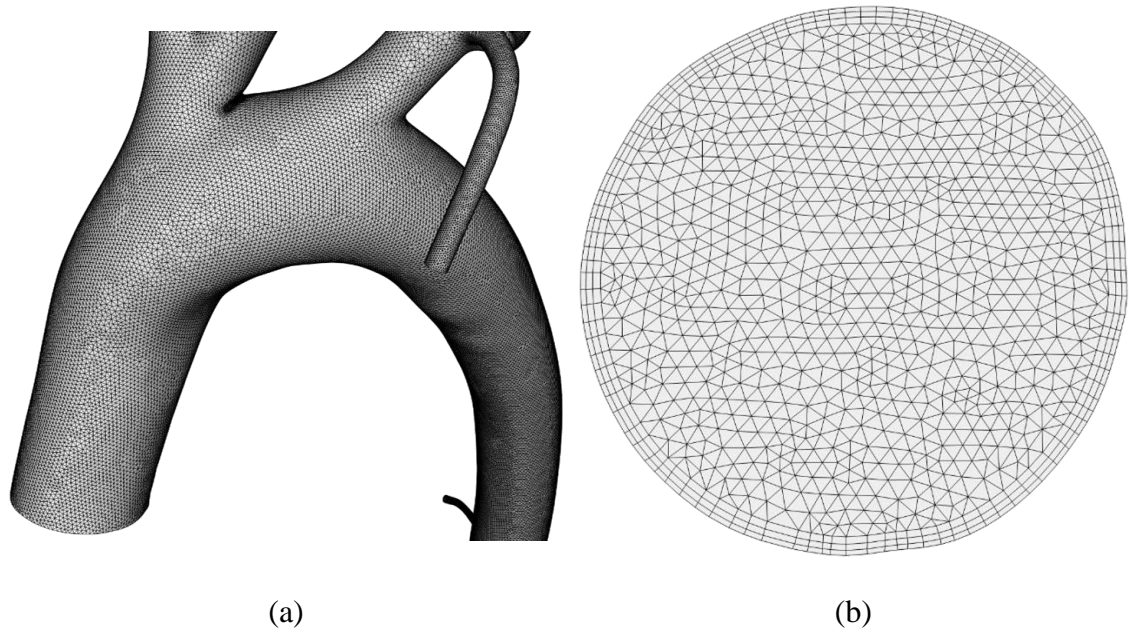
Figure 2.2 - Schematic of the mesh used for the present simulations. (a) View of the mesh through the ascending and DAo; (b) Cross-sectional image of the mesh at the aorta root inlet.

2.2.3 Numerical Procedure

In both the steady-state and pulsatile simulations, the blood flow is defined as a three-dimensional, incompressible, isothermal, Newtonian and laminar flow. Dynamic viscosity (μ) and density (ρ) of the blood are set to 4.043 $g{\cdot}m^{-1}{\cdot}s^{-1}$ and 1044 $kg{\cdot}m^{-3}$, respectively [53], [54]. The governing equations are solved numerically using ANSYS-CFX Version 15.0, using a fully implicit second-order backward Euler differencing scheme. The convergence criterion is set to $1{\cdot}10^{-6}$ in this study. Commercial visualisation tool, Ensight 10.1.6 was used to post-process the results.

2.2.4 Boundary Conditions

In the present configuration, no-slip BC is applied to all walls. A rigid wall model is also assumed, which has been shown to be a valid assumption [111].

In the present work, seven test cases are studied based on the combination of inlets, outlets and pulsatility of the flow, as shown in Table 2.1. Details of how each of these BCs are prescribed in all test cases are given below, (also refer to Table 2.2).

Table 2.1 - Summary of the cases studied in the present work.

	Inlet BC		Outlet BC			Pulsatile Dynamics	
	Uniform Velocity Profile	Non-uniform (Fully-developed Profile)	ML	*In vivo*+ML	Traction Free	Steady-State	Unsteady (Pulsatile)
Test 1	●		●			●	
Test 2	●			●		●	
Test 3	●				●	●	
Test 4		●	●			●	
Test 5	●		●				●
Test 6	●			●			●
Test 7	●				●		●

Table 2.2 - Derivation of BCs for various tests. For the *in vivo*+ML case, 7.1 % and 14.7 % of flow entered the left subclavian and innominate artery respectively as results by Barakat et al. [57] indicate. It was also assumed that 2 % of flow entered the intercostal branches in total, as previously considered by Kazakidi et al. [119], but is otherwise an arbitrary value. For all subsequent arteries, the flow was predicted using ML. For the ML case, the flow rate through each individual outlet was proportional to its corresponding area only.

Boundary Name		Diameter (mm)	Boundary Condition		
			Flow Split (%)		Traction Free
			ML	*In vivo*+ML	
Aortic Root	(a)	5.84	100	100	-
Right Subclavian Artery	(b)	2.61	13.63	6.80	
Right Common Carotid Artery	(c)	2.23	8.47	4.22	Zero pressure
Left Common Carotid Artery	(d)	2.13	7.37	3.68	
Left Subclavian Arteries	(e)	1.08	0.97	1.17	
	(f)	0.36	0.04	0.04	
	(g)	0.72	0.29	0.35	
	(h)	1.63	3.32	4.00	Zero pressure
	(i)	0.82	0.43	0.52	
	(j)	0.75	0.32	0.39	
	(k)	0.88	0.53	0.64	
Intercostal Artery	(l)	0.45	0.07	0.13	
	(m)	0.51	0.10	0.19	
	(n)	0.41	0.05	0.10	
	(o)	0.48	0.09	0.16	
	(p)	0.48	0.09	0.16	
	(q)	0.51	0.10	0.19	Zero pressure
	(r)	0.57	0.15	0.28	
	(s)	0.59	0.16	0.30	
	(t)	0.53	0.12	0.22	
	(u)	0.56	0.13	0.26	
Abdominal Aorta	(v)	4.36	63.59	76.20	Zero pressure

Inlet (Steady-state)

- **Uniform Velocity:** A uniform velocity of ≈20 cm·s^{-1} was applied over the entire boundary (i.e., at the AR), with a corresponding Reynolds number of 300 based on the inlet diameter and velocity, consistent with other studies [53], [54]

- **Non-Uniform (Fully-Developed Profile):** In order to generate a parabolic profile, an extension region of length 20D (where D is the diameter of the inlet cross-sectional area) was affixed to the inlet (a) (refer to Figure 2.1). A uniform velocity was then applied to the new 'pseudo' inlet, allowing the flow to become fully-

developed as it reaches the original inlet (a) location. This method was used as a substitution for incorporating a parabolic profile at the inlet, in line with the method used by Do et al. [44].

Outlet (Steady-state & Transient)

- **Murray's Law:** A percentage of the equivalent inlet mass flow rate value was assigned individually to each vessel outlet. For the steady-state simulations, the outlet flow rates were calculated from the mean inlet flow rate. For the transient simulations, the outlet flow rates were re-calculated at the start of each timestep. The mass flow rate percentages were based on ML. The mass flow rate per outlet was converted to its velocity counterpart by accounting for the outlet cross-sectional area. This value was then assigned as a velocity normal to the boundary and defined as an 'outlet'.

- *In vivo*+**ML:** When the total flow out of an arterial bundle (e.g. left subclavian arteries) was known due to the *in vivo* data [57], but the flow through the individual artery within said bundle was not, ML was implemented for the individual vessel, and scaled accordingly to satisfy the *in vivo* data. For the steady-state simulations, the outlet flow rates were calculated from the mean inlet flow rate. For the transient simulations, the outlet flow rates were re-calculated at the start of each timestep.

- **Traction Free***:* A 'traction free' or 'zero pressure' condition was applied to each outlet individually and defined as an 'opening' to allow for flow reversal at the boundary if it occurs. This BC is used in various models due to its simplicity and when patient specific *in vivo* measured flow rates are not readily available [43], [48], [49]. The traction free BC is similar to assuming the vessel is cut and exposed to atmospheric conditions and hence neglects the resistive effects of downstream vessels [50].

Pulsatile Dynamics

- **Steady-State:** Tests 1-4 have been conducted using steady-state conditions. Steady-state calculations allow quick comparison of different inlet and outlet BCs.

- **Unsteady (Pulsatile):** The present geometry corresponds to a rabbit with a heartbeat period of 0.322s and a cardiac output of 4.385g/s. The outlet mass flow rate at each time step was calculated by multiplying the inlet mass flow rate at that moment in time by the flow percentage of the respective outlet. The effects of having pulsatile flow conditions are evaluated in Tests 5-7, where the time period (T) was taken to be

0.322s with a time-step size of 0.001s. This time period to time-step ratio is assumed to be adequate as it is much greater than that used in other relevant transient studies [56], [112]. Unsteady simulations were ran for four cardiac cycles, the results were recorded during the final cycle. The results are recorded at the end of every third time-step and a Womersley number (α) of 6.552 was calculated through:

$$\alpha = \frac{D}{2}\left(\frac{2\pi\rho}{\mu T}\right)^{1/2} \tag{2.1}$$

In cases resulting in $\alpha \gg 1$, it is assumed that it is important to account for unsteady nature of the flow [53]. To obtain a time-dependent, uniform velocity profile to be applied to the inlet, the velocity profile measured at the AAo location of a similar rabbit studied by Avolio et al. [113] was used (shown in Figure 2.3).
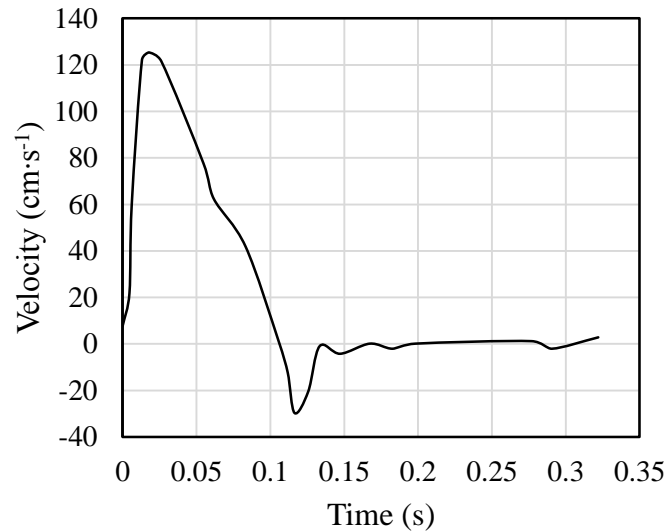
Figure 2.3 - Velocity profile applied at the AR in the unsteady (pulsatile) simulations. The velocity profile is approximately the shape of the '*in vivo* acquired' velocity waveform present in the AAo of a male New Zealand white rabbit with weight of 3.2 kg, heartbeat period of $\approx$0.322 s and a cardiac output of $\approx$4.385 g·s^{-1}, taken from Avolio et al. [113].

2.3   Results & Discussion

The localisation of various lesions including atherosclerosis and thrombosis have been extensively studied and are related to different local haemodynamic metrics [71]–[75]. These haemodynamic parameters can be directly derived from the flow velocity fields obtained by CFD simulations. Whilst the performance of these parameters on predicting the localisation of atheroma is important in this study, the focus is on the sensitivity of these parameters to the BCs prescribed during the numerical simulation.

The parameters chosen for the present analyses include WSS, TAWSS [78], OSI [78] and RRT [77]. These parameters have been chosen because i) localised distribution of low-WSS and high-OSI strongly correlate with the locations of atheroma [78], ii) platelet activation may be induced by the combination of large exposure time and high shear stress [80]–[83], iii) stagnant and recirculating flow regions can cause platelet aggregation and thrombosis [84]. Figure 2.4 and Figure 2.5 show the distributions of the above metrics, respectively, for the aortic arch and in an unfolded lumen within the vicinity of the intercostal branches. Figure 2.5 should be interpreted so that the vertical axis represents distance along the aorta (with blood flow from top to bottom) and the horizontal axis represents the circumferential distance.
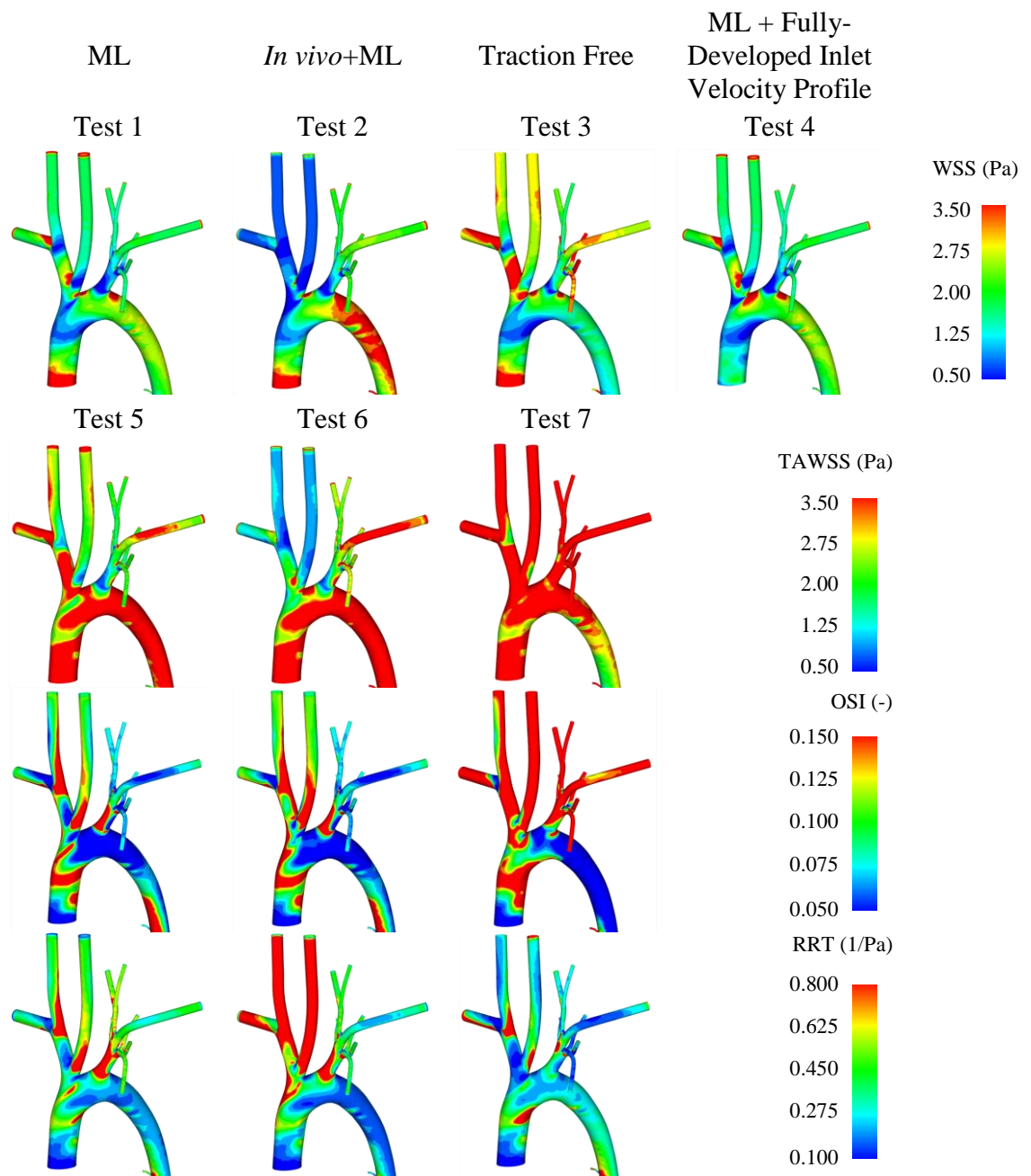
Figure 2.4 - Distributions of different haemodynamic parameters calculated for the aortic arch and descending thoracic aorta, viewed from outside the vessel.
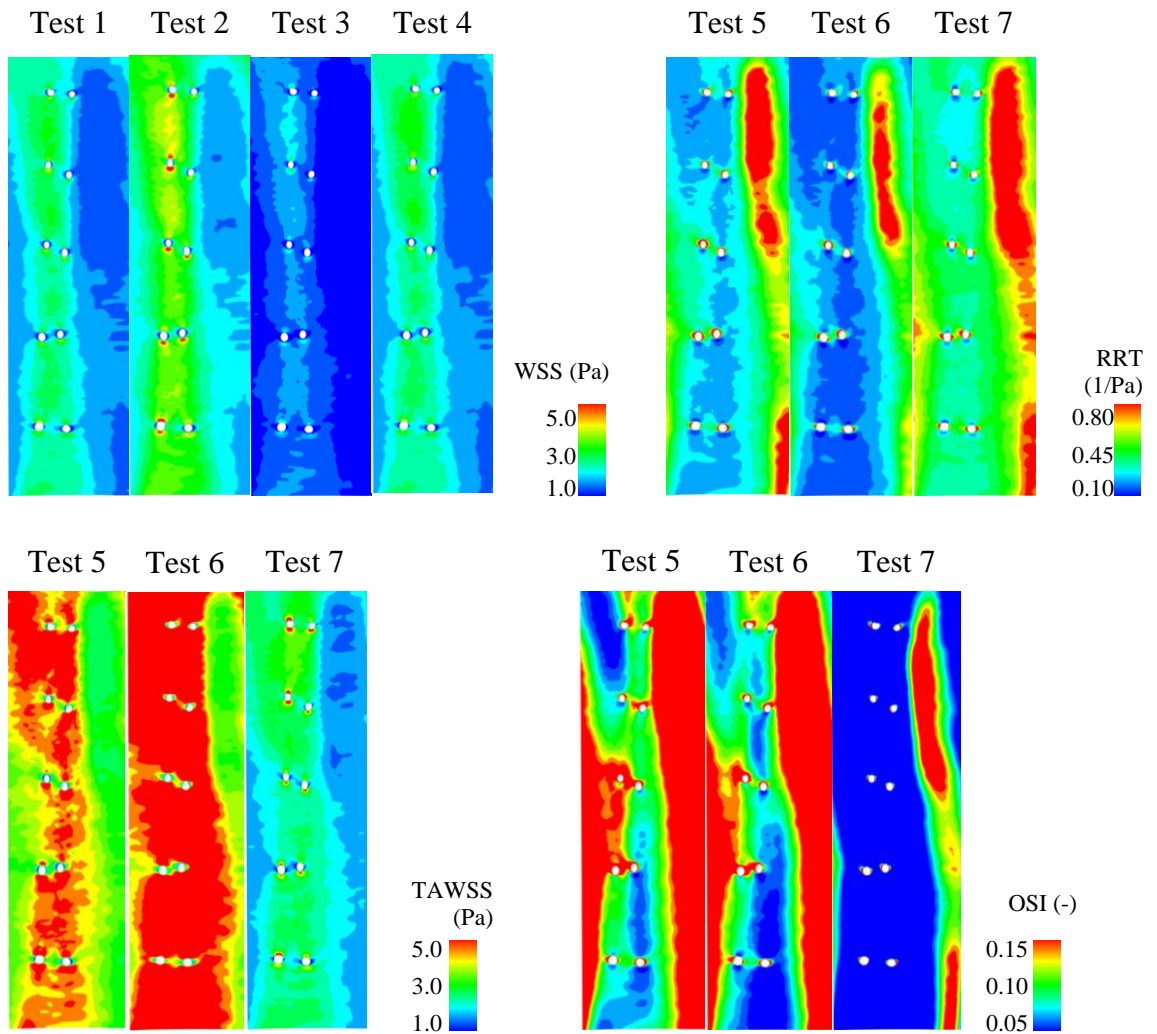
Figure 2.5 - Distributions of different haemodynamic parameters calculated for a section of the DAo containing the intercostal branch ostia. This section has been opened ventrally and shown *En face*. The vertical axis represents distance along the aorta (with blood flow from top to bottom) and the horizontal axis represents the circumferential distance.

In order to quantify the changes in these haemodynamic parameters, area-weighted average values in a number of locations are selected, as shown in Figure 2.6. These locations were monitored to quantify how haemodynamic metrics are affected by each BC, thus numerically highlighting the regions most affected by the prescribed BCs.
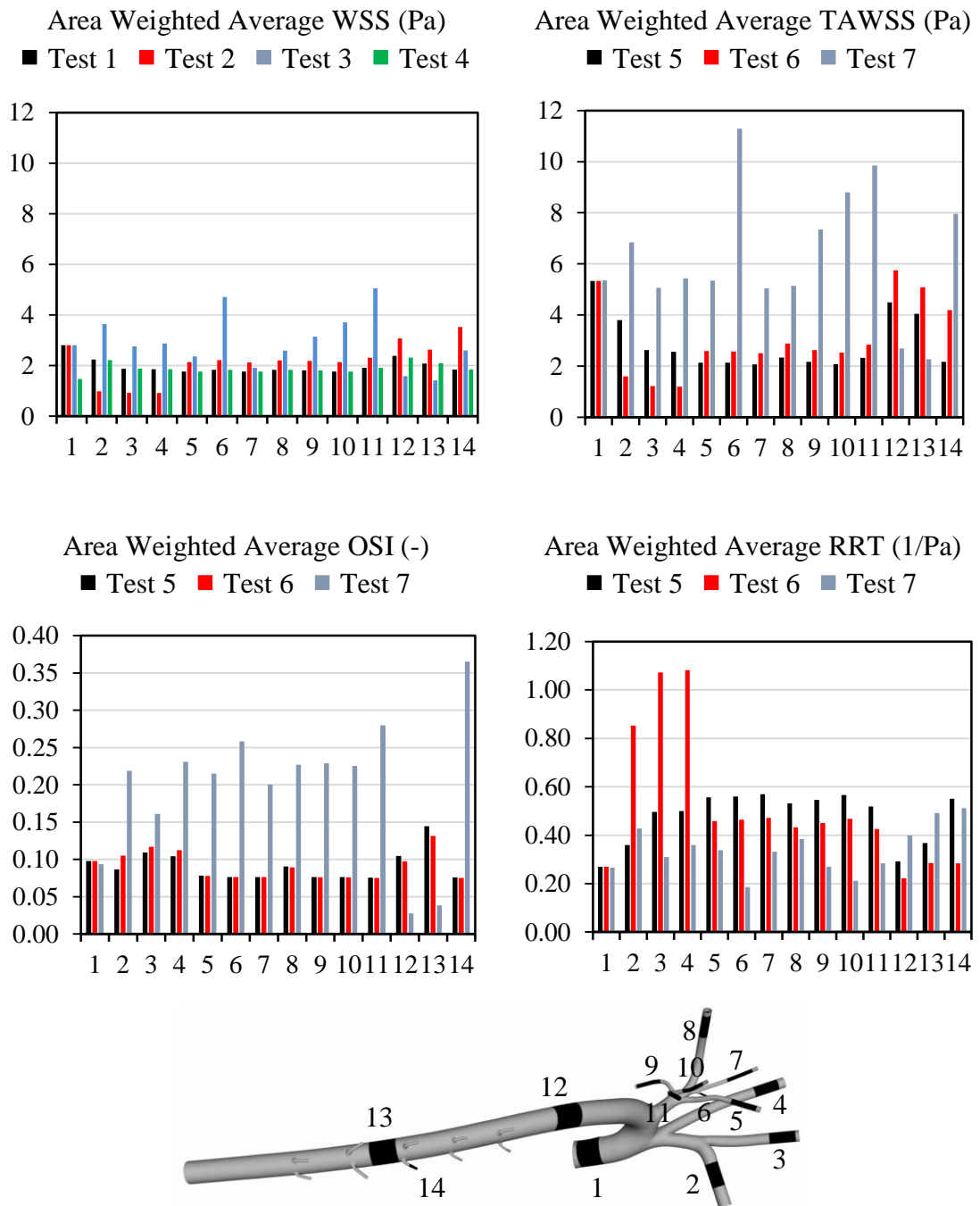
Figure 2.6 - Charts of area-weighted averages of metrics evaluated over various locations illustrated at the bottom of the image.

Each haemodynamic metric will be discussed below separately.

2.3.1 Wall Shear Stress

In Figure 2.4, when changing the outlet BC from ML to *in vivo*+ML (Test 1 to Test 2), only small discrepancies can be seen in the WSS distributions within the ascending aorta as well as the aortic arch. However, the right subclavian, right and left common carotid arteries experienced a drop in WSS magnitude from Test 1 to Test 2. Large differences also appeared in the upper section of the descending aorta, showing that the WSS

magnitude lost in Test 2 within the right subclavian, right and left common carotid arteries is compensated by the higher WSS distribution within the descending aorta. Using the popular traction free BC (Test 3) results in approximately a 75 % increase in the WSS within all the side branches connected to the aortic arch when compared against Test 1. Whilst WSS generally decreases by approximately 34 % within the descending aorta for Test 3 compared to Test 1. By changing the inlet BC from uniform velocity flow rate to fully-developed inlet (Test 1 to Test 4) whilst maintaining the same outlet BCs, the WSS distribution close to the aortic root decreases by approximately 50%. The discrepancies throughout the rest of the geometry between Test 1 and Test 4 are mainly insignificant.

The discrepancies between Tests 1-4 are also obvious in , where the WSS distributions are compared for a section of the DAo containing the intercostal branches. In general, Tests 1 and 4 produce somewhat similar WSS distributions. Whilst Test 2 experiences higher magnitude axial streaks, mainly between the intercostal branches than the other tests. The axial streaks in Test 3 are the least pronounced of all four tests.

Comparing the area-weighted average WSS for Tests 1-4, Figure 2.6 immediately shows the over estimation of WSS in the smaller diameter aortic arch branches (locations 2-4, 6, 8-11) when using the traction free BC (Test 3) compared to the other tests.

2.3.2   Time-Averaged Wall Shear Stress

The effects of pulsatility applied at the inlet can be examined by comparing the TAWSS distributions of Tests 5-7 to Test 1-3 in Figure 2.4 and Figure 2.5. The effects of changing the outlet BC on TAWSS maps (Tests 5-7) in Figure 2.4 and Figure 2.5 are somewhat similar to what was observed in WSS distributions in Tests 1-3 (see Section 3.1).

However, incorporating pulsatility into the simulation led to the TAWSS magnitudes generally being higher (+70%) than their WSS counterpart. Moreover, when changing from steady state to pulsatile dynamics, the traction free boundary condition experiences a further increase in TAWSS within the smaller diameter vessels (locations 5-11 and 14).

The axial TAWSS streaks within the areas shown in are again similar to those found in WSS distributions, with no extra important features becoming present by incorporating pulsatility into the simulations. The magnitudes of TAWSS were however greater than their WSS counterpart as previously discussed.

2.3.3 Validation

Figure 2.7 shows the comparison between the WSS and TAWSS distributions around the intercostal branches within the thoracic aorta of the rabbit studied during this work and the red oil dye distribution within the thoracic aorta of a mature cholesterol-fed rabbit [114]. Similar to the configuration used in the present numerical simulations, the *in vivo* data corresponds to a New Zealand white rabbit and the red oil dye has been used to identify early stage atherosclerotic lesions. Note that the *in vivo* data only contains four out of five intercostal pairs as the third pair was excised from the dataset for a different study. The *in vivo* data shows distinctive axial streaks of lipid/fatty deposition (i.e., representing the localisation of CVD); thus one may assume that the BCs that produces the closest WSS distribution to these streaks may be considered to be more physiologically accurate (assuming that atherosclerosis deposition is correlated to low WSS [18]). Tests 1 & 5 (ML) produce the closest comparison to the *in vivo* data, with three out of the six monitored regions showing strong correlations. Therefore, as far as this specific study is concerned and given the relatively small *in vivo* data sample size, the ML outlet BC appears to produce the closest relationship between WSS distribution and lipid deposition. On the other hand, Tests 2 & 6 (*in vivo*+ML) fail to capture two main zones of lipid deposition (i.e., Sections 'b' and 'd' in Figure 2.7), while the traction free BC returns the least accurate predictions. This comparison against the *in vivo* data appears to suggest that for this study, partially incorporating *in vivo* measured flow ratios (Tests 2 & 6) does not necessarily return the best results.

Similarity						
	a	b	c	d	e	f	Total
Test 1	3	0	2	2	3	3	**13**
Test 2	2	0	2	0	3	3	**10**
Test 3	1	1	2	2	1	2	**9**
Test 5	1	0	2	3	3	3	**12**
Test 6	2	0	2	0	3	2	**9**
Test 7	1	2	2	2	0	2	**9**

0 = No correlation
3 = Strong correlation
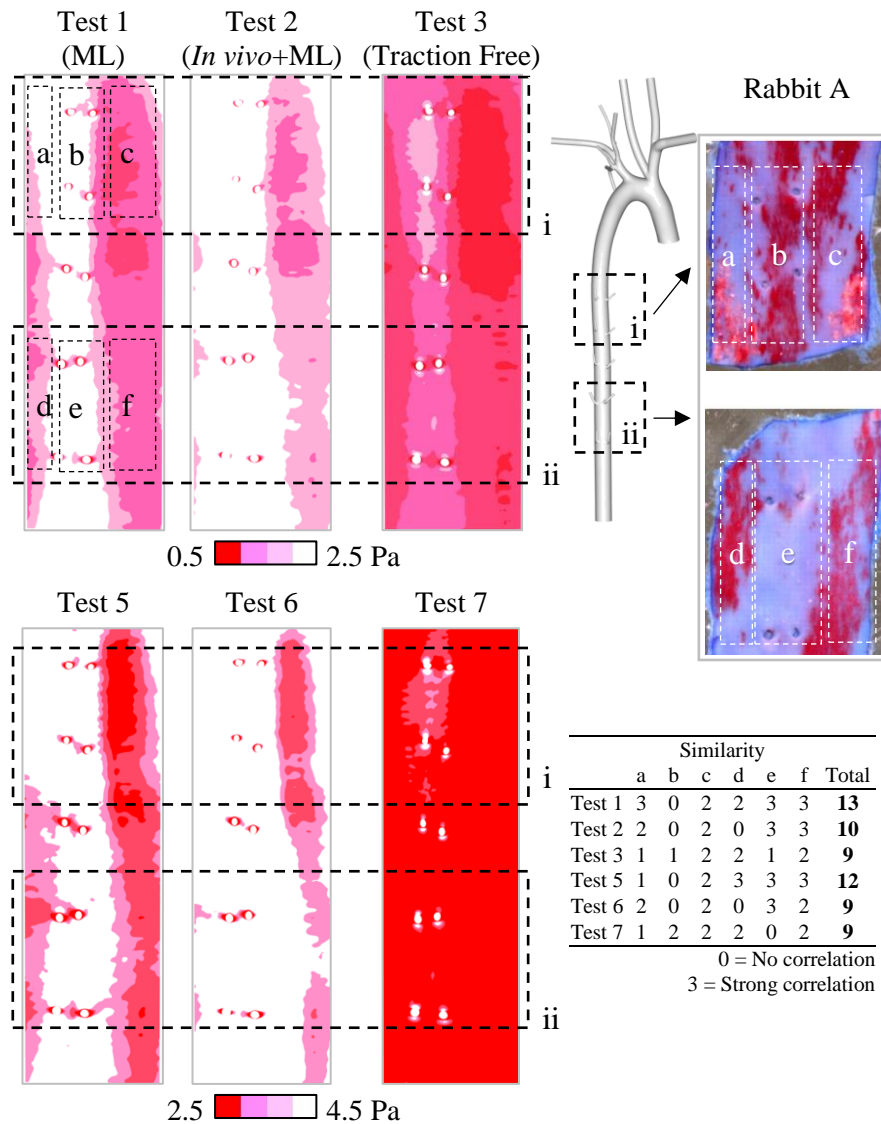
Figure 2.7 - (Left): WSS distribution around the intercostal branches within the thoracic aorta of the rabbit studied during this study using three different outlet BCs. (Right): *En face* sections from the thoracic aorta of two mature cholesterol-fed rabbits stained with red oil dye to identify early stage atherosclerotic lesions. These images are taken from Vincent et al. [53] who adapted the data from the original work of Cremers et al. [114]. These sections are shown with the endothelial surface facing upward.

2.3.4   Oscillatory Shear Index

The discrepancies in the OSI maps and area-weighted average values in Figure 2.4 - Figure 2.6 between Test 5 and Test 6 are mostly negligible, with a minor decrease in OSI within the right subclavian, right and left common carotid arteries for Test 6. However, when the traction free BC is used (Test 7), the OSI increases significantly ($\approx$+160%) in the aortic arch branches compared to Tests 5&6. On the other hand, as shown in Figure 2.6, the average OSI tends to be reduced by approximately 70% in the descending aorta (locations 12 & 13), while there is almost no difference in OSI within the aortic root

(location 1). This is because the changes in haemodynamics generally only occur close or distal to the first peripheral branches.

2.3.5 Relative Residence Time

RRT distributions shown in Figure 2.4 for Tests 5&6 are similar, except for some of the RRT magnitudes for Test 6 being generally 120 % greater than Test 5 within the right subclavian, right and left common carotid arteries (locations 2-4 in Figure 2.6). Furthermore, the RRT distribution discrepancies between Test 5&6 within the descending aorta were negligible. The traction free BC has resulted in significant under estimation of RRT within the aortic arch branches. This under estimation is directly linked to the over estimation of TAWSS in the same branches (with RRT being inversely proportional to TAWSS – see Eq. (1.8). The discrepancies between Tests 5-7 are also evident in the RRT maps in , where changing the outlet BC results in marked differences in areas surrounding the intercostal branches.

2.3.6 Effects of Uniform/Fully-Developed Inlet

The present results indicate that, unless the distribution of haemodynamic metrics within the aortic root and ascending aorta regions are of significance (e.g. studying flow entering coronary arteries), the effect of fully-developed flow can be ignored in order to save on computational time. The inaccuracy of time-averaged haemodynamic metric distributions due to constant mass flow inlet BC quickly depreciates, supporting the findings of Peiffer et al. [56]. This knowledge is useful as an accurate representation of fully-developed flow exiting the aortic valve would be complex and difficult to obtain.

2.3.7 Effects of Outlet Boundary Condition

The present results demonstrate that the traction free outlet BC results in significantly different haemodynamic metric distributions when compared to the BCs based upon ML and/or *in vivo* data. When observing WSS, TAWSS, and to some extent OSI, in general it was the larger arteries that were the least affected by the outlet BC, whereas within the smaller arteries the outlet BC had a significant effect. Suggesting that either the ML or *in vivo*+ML BC can be used when the focus is on these haemodynamic metrics within larger vessels, but care must be taken when the attention is on the smaller vessels. On the contrary, the discrepancies in metric distributions shown around the intercostal branches and through the descending aorta suggested that it is still important to consider how the outlet BCs are applied.

2.3.8 Effects of Pulsatility

Despite the advantages of steady-state calculations, blood flow is naturally pulsatile and assuming a steady-state condition for the present configuration, one would not be able to calculate important shear rate-related haemodynamic metrics (discussed in Section 3) and truly unsteady flow phenomena cannot be captured.

The effect of different pulsatile velocity profiles at the inlet have previously been studied. For instance Xiang et al. [115] found minimal effect on WSS and OSI distributions within patient specific aneurysms, as long as mean flow rate is unchanged. However, to the authors' knowledge, the effects of pulsatile flow through a complex aorta geometry has not yet been quantified in which the inlet profile remains a constant and the outlet BC is the variable. Vincent et al. [53] chose to ignore the possible effects due to pulsatility after calculating a Womersley number substantially over the threshold in which pulsatile effects can be ignored, consequently, their conclusions were based on steady-state results. The results in the present study demonstrate that both WSS and TAWSS share similar patterns, while TAWSS generally has higher magnitudes. The similarity between WSS and TAWSS distribution in this study is in agreement with the findings for aneurysm models [116]. This suggests that it is not necessary to run transient simulations when only considering WSS within the aorta or its neighbouring arteries. However, pulsatile flow is still crucial for capturing other metrics such as TAWSS, OSI and RRT (which are widely believed to be linked to the development of CVDs) as they are time-dependent metrics. By observing the streaks in the in vivo images by Cremers et al. [114], it is likely that the pulsatility of the flow has insignificant impact on predicting atherosclerotic lesion deposition when only using WSS as an indicator.

2.4 Limitations & Future Work

Various outlet BC models which are accepted as more physiologically accurate have been ignored during this study. Namely the Windkessel model [58], [104], structured tree model [47], complex Windkessel model [117] and multiscale models [118]. Despite these models being able to further reduce modelling error, they are often complex to incorporate into simulations and have therefore been omitted from this study.

This work studies the effects of outlet BCs within a rabbit aorta configuration. Therefore, the conclusions are only explicitly applicable to this specific configuration. However, this work provides an initial and indirect understanding of the effects outlet BCs could have on human aorta haemodynamics on which further studies can develop.

The future direction of this work will involve comparing commonly used outlet BCs against a larger number of more physiologically accurate outlet BC models. Extending this work to incorporate a large and diverse cohort of human aorta configurations and performing a statistical analysis would improve the relevance of this work.

2.5   Summary

In the present study, using advanced CFD codes and through comparison with *in vivo* data, the impact of various inlet and outlet BCs on predicting the localisation of CVDs were assessed for an accurately-represented rabbit aorta configuration. One of the main findings to emerge from the present study was that prescribing a transient simulation and a fully-developed flow at the inlet are not required when the focus is only on the flow within the aorta and around the intercostal branches. Also, assuming the widely-accepted low WSS theory of Caro et al. [18], it was found that the ML-based outlet BC returns the most physiologically accurate results, when compared against *in vivo* data.

CHAPTER 3

COMPARISON BETWEEN SIMPLE AND ADVANCED OUTLET BOUNDARY CONDITIONS ON HAEMODYNAMIC METRICS

3.1 Introduction

The previous chapter focused on using common inlet and outlet BCs. However, the previous chapter did not investigate a more advanced outlet BC known as the three-element Windkessel, due to the lack of required R_p, R_d and C parameters for the corresponding geometry.

Using i) traction free (zero pressure), ii) flow ratios based on ML and iii) back pressures based on a three-element Windkessel model have all become common methods of implementing outlet BCs. Despite advanced models such as the three-element Windkessel being shown to produce more physiological haemodynamics, the previous two methods are still being used to date. There appears to be a lack of clear quantification of the difference in aortic haemodynamics between these three methods.

As an extension to the previous chapter, the common traction free and ML BC have been applied to an aorta model which has the data required to also implement a three-element Windkessel model to gain a further understanding of the effect of outlet BCs on aortic haemodynamics.

Therefore, the objective of this chapter is to assess the impact of using some widely-used outlet BCs on various haemodynamic metrics used for predicting the localisation of CVDs on a complex aorta model. Specifically the traction free, ML and three-element Windkessel based models.

3.2 Method

3.2.1 Geometrical Model

A patient-specific model of a 23-year old female with normal aortic function and an AR diameter of 20 mm is used in this study (as shown in Figure 3.1). The patient specific geometry was produced using SimVascular software package (https://simtk.org) to process gadolimium-enhanced Magnetic Resonance Angiography (MRA) image data [63]. The geometry starts from the AR, includes the RSA, RCCA, Left Common Carotid

Artery (LCCA), Left Subclavian Artery (LSA) and finishes at the TAo. Studying such a geometry is beneficial for understanding the correct BCs to use in LVAD, Cardiopulmonary Bypass (CPB), aortic dissection and aortic aneurysm studies.

(a)   (b)   (c)
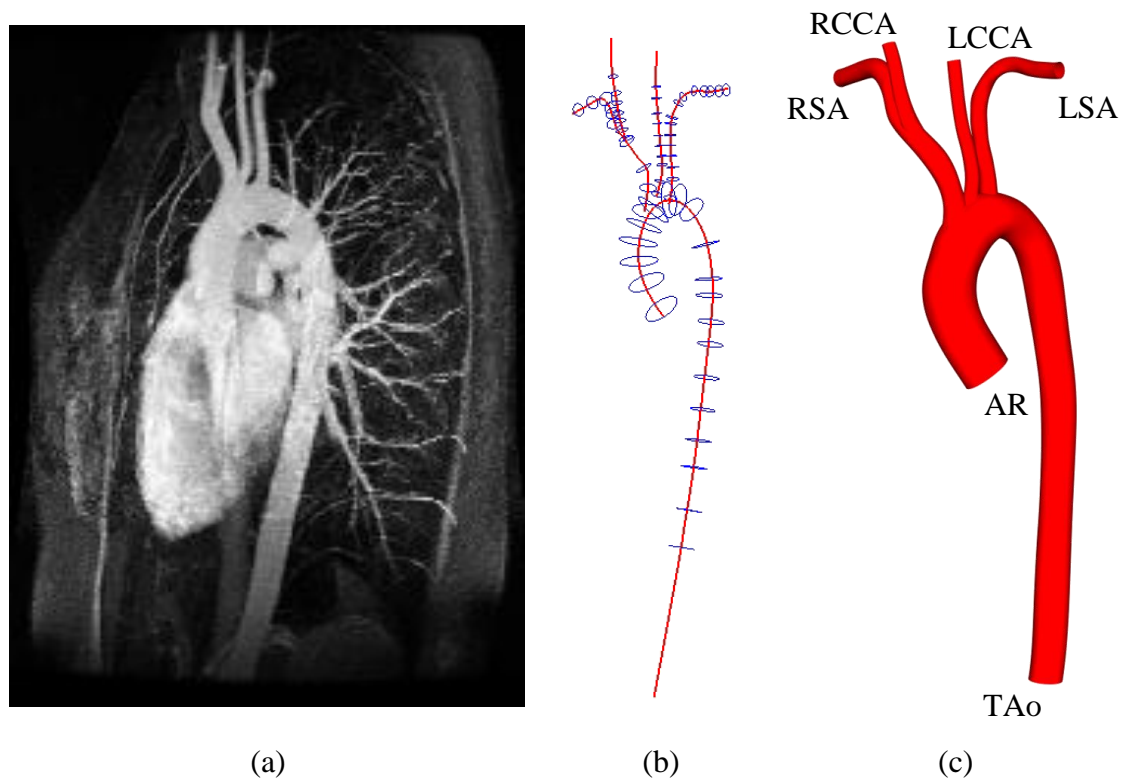
Figure 3.1 - Schematic of the present configuration of a 23 year old female aorta with normal aortic function. (a) Patient-specific volumetric image data obtained via Gadolimium-enhanced MRA technique [63]. (b) Centrelines and cross-sections used to reconstruct the geometry [63]. (c) Surface model reconstructed in preparation for CFD simulations.

3.2.2 Computational Domain

The geometry was meshed using ANSYS-Meshing Version 17.1 (ANSYS Inc., Canonsburg, PA, USA). The mesh was based on a finite volume hybrid mesh consisting of tetrahedral elements within the core region and prism layers (3 elements thick) near the wall to allow for large spatial velocity gradients. In order to ensure the accuracy of the simulations, a series of six steady-state computations with various mesh refinement levels (ranging from 2.3 to 5 million elements) were conducted to ensure mesh independency. A flow rate of 3.192 L·min^{-1} was applied to the AR and a traction free outlet BC was applied to the outlets. The results were compared by measuring the spatial mean WSS over regions of the RSA, LCCA and TAo. Refinement from ≈2.3 million to ≈3.3 million elements resulted in a maximum change in spatial mean WSS of ≈0.5 % over the

monitored regions. A one-dimensional velocity profile was also monitored at a point through the AAo, where the peak velocity changed by 1 % from 2.3 to 3.3 million elements and was insignificantly affected with further mesh refinement. Therefore, the mesh of ≈3.3 million elements was considered adequate, and hence used for further simulations in this study.

3.2.3   Boundary Conditions

Three tests are studied in this work. In all tests, a no-slip BC is applied to all walls and a rigid wall model is assumed, which has been shown to be a valid assumption [61], [111]. Details of the inlet and outlet BCs will be described next.

Inlets. For all tests, a uniform velocity profile was imposed at the inlets. The patient-specific Phase Contrast-Magnetic Resonance Imaging (PC-MRI) waveform by LaDisa et al. [63] was applied to the AR, as shown in Figure 3.2.
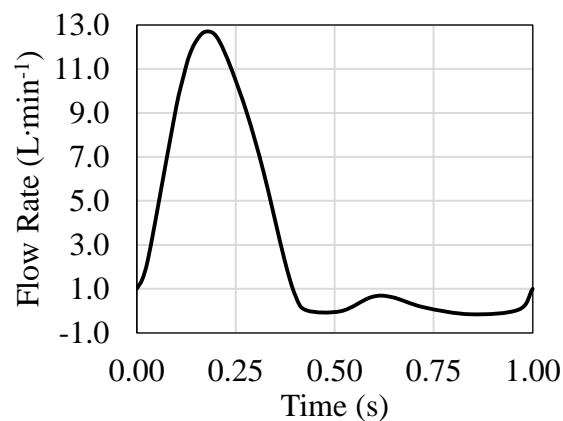
Figure 3.2 – Inlet flow rate profile adapted from the patient specific PC-MRI waveforms obtained via La Disa [63].

Outlets. For Test 1, a 'traction free' or 'zero pressure' condition was applied to each outlet individually and defined as an 'opening' to allow for flow reversal at the boundary if it occurs. This BC is used in various models due to its simplicity and when patient-specific *in vivo* measured flow rates are not readily available [43], [48], [49]. The traction free BC is similar to assuming the vessel is cut and exposed to atmospheric conditions and hence neglects the resistive effects of downstream vessels [50].

For Test 2, a percentage of the equivalent inlet mass flow rate value was assigned individually to each vessel outlet, refer to Table 3.1. The mass flow rate percentages were based on ML. The mass flow rate per outlet was converted to its velocity counterpart by

accounting for the outlet cross-sectional area. This value was then assigned as a velocity normal to the boundary and defined as an 'outlet'.

Table 3.1 - Derivation of BCs for the ML case, the flow rate through each individual outlet is proportional to its corresponding area.

Boundary Name	Diameter (mm)	Flow ratio (%)
AR	20.14	100.00
RSA	7.53	10.76
RCCA	5.54	4.29
LCCA	5.18	3.51
LSA	5.63	4.48
TAo	14.51	76.96

For Test 3, the three-element Windkessel is implemented to account for the physiological back pressures produced within the arterial system based on the resistance and compliance of the proximal and distal vessels (refer to Section 1.4.4 for a more detailed explanation).

3.2.4   Numerical Procedure

The CFD solver ANSYS-CFX (Version 17.1) was used for the simulations. Blood was defined as a three-dimensional, incompressible and isothermal fluid. Dynamic viscosity and density of the blood are set to 0.004 Pa·s and 1060 kg·m^{-3}, respectively [120]. Each simulation is ran for 4 cardiac cycles (4 s) with a timestep size of 1.25 ms and 10 coefficient loops per timestep, this proved adequate in order to allow the boundary flow rate and pressure waveforms to converge, see Figure 3.3. The results are recorded during the final cardiac cycle. The commercial visualisation tool, Ensight 10.1.6 was used to post-process the results.
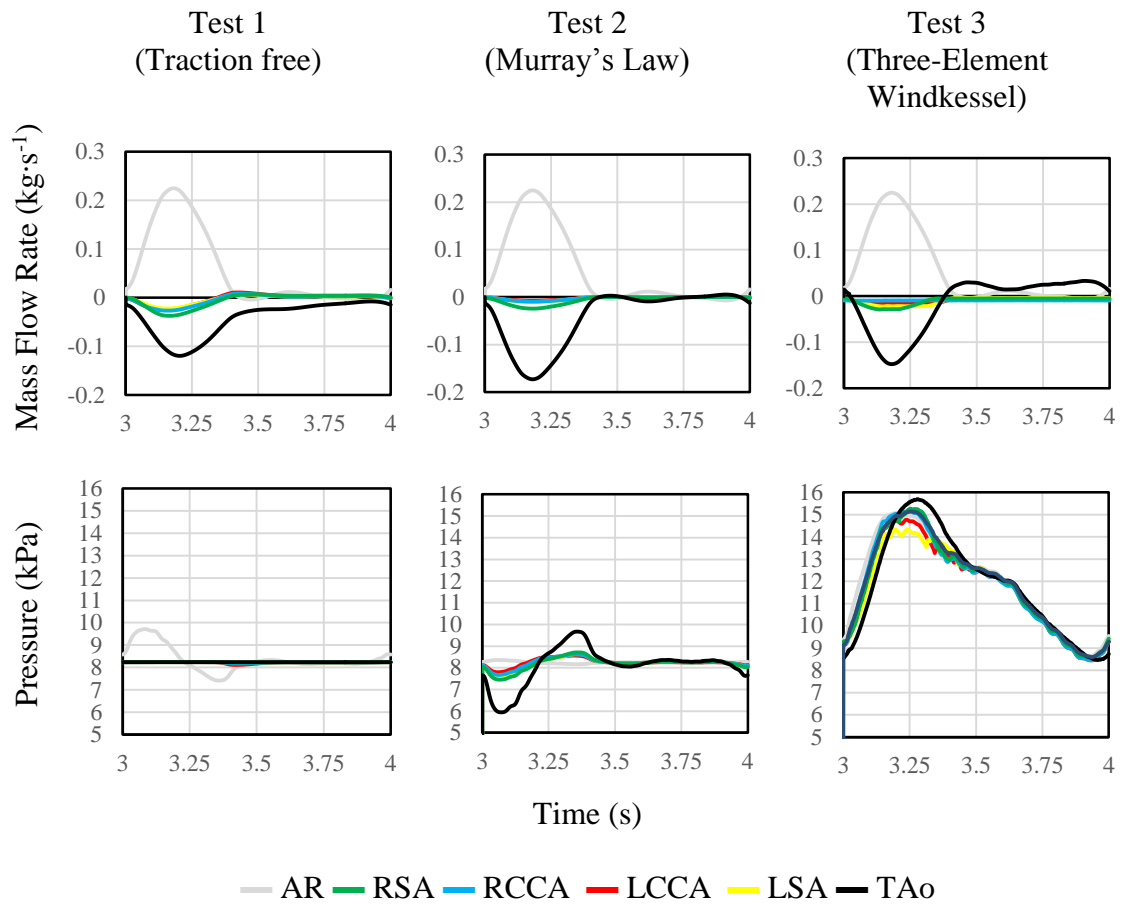
Figure 3.3 − The top and bottom rows represent the mass flow and pressure history waveforms respectively for all tests, both are recorded during the final cardiac cycle. For Test 3, the fourth period results correlate to producing a physiologically realistic blood pressure of 15131/8781 Pa (113/66 mmHg).

3.3 Results & Discussion

The three-element Windkessel BC is currently believed to be the one of the most physiologically accurate in terms of being able to capture downstream conditions [104]. Hence, the other two methods studied here will be compared against the Windkessel method (Test 3) as a reference.

3.3.1 Time-Averaged Velocity

In this section, the effects of the outlet BC on the perfusion of the aorta and its branches are examined. In order to measure the aortic perfusion, Time-Averaged Flow Rate (TAFR) and Time-Averaged Velocity (TAV) are calculated over the final cardiac cycle in order to examine the perfusion of vessels and general haemodynamics. Figure 3.3 and Figure 3.4 provide a quantitative approach to assessing the TAFR, whilst Figure 3.5 shows a more qualitative illustration of TAV streamlines.
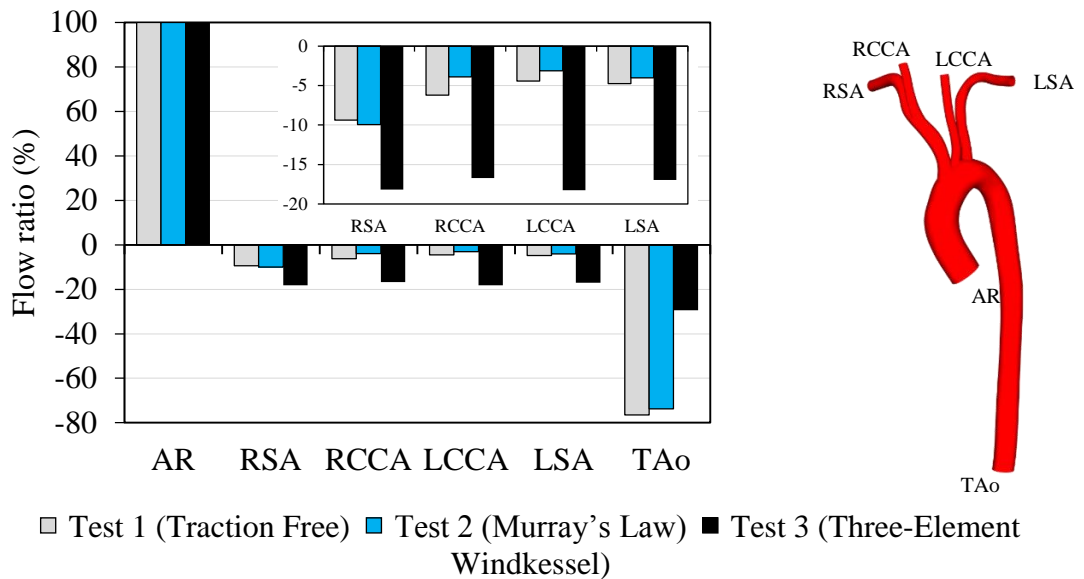
Figure 3.4 – Ratio (%) between the TAFR through the corresponding artery and the total TAFR through the system. Positive and negative ratios represent inlets and outlets, respectively.
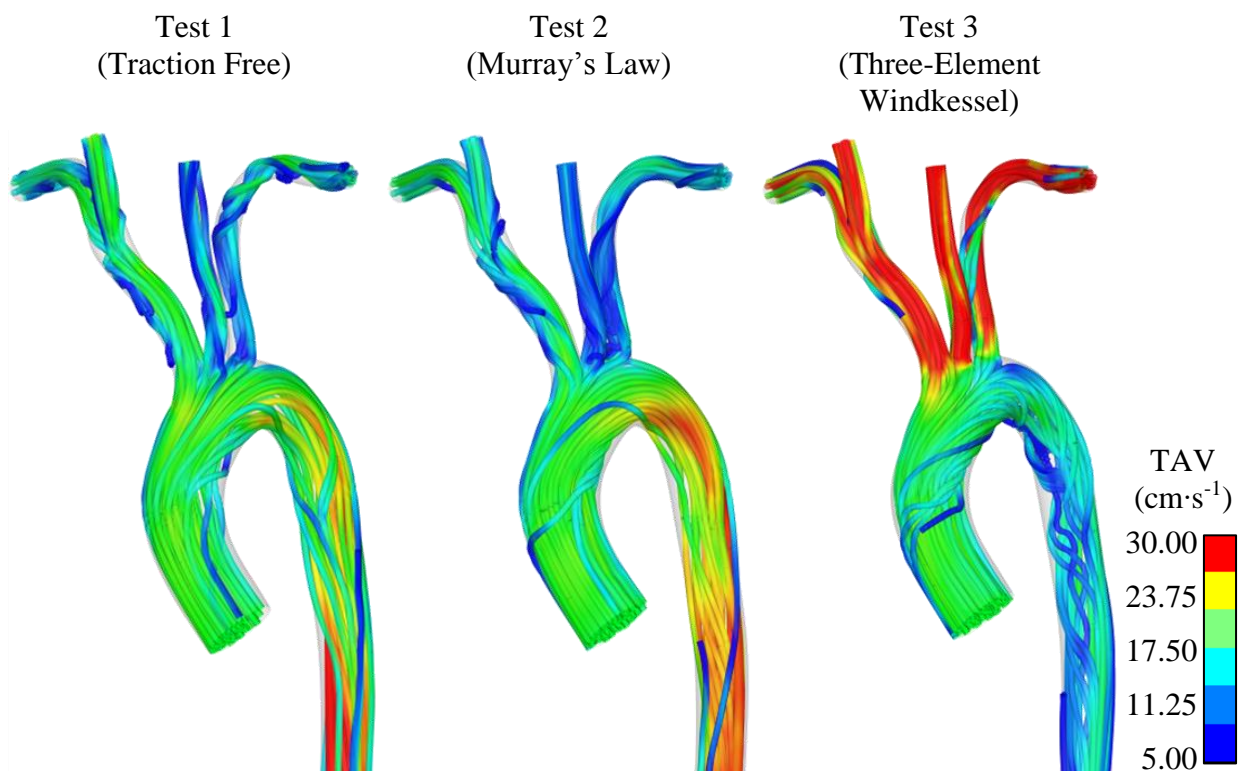
Figure 3.5 – Time-averaged blood flow velocity streamlines coloured by TAV.

The results generally show that none of the outlet BCs studied produced the same results, there is slight discrepancy between the traction free and ML BC, whilst the three-element Windkessel produced significantly different results.

Subclavian and Carotid Arteries. Outlets RSA, RCCA, LCCA and LSA all experienced approximately 33 % of the flow experienced by these arteries in Test 3, therefore suggesting that the flow to the subclavian and carotid arteries are significantly underestimated when using the traction free and ML BCs. There was minimal discrepancy between the TAFR between Test 1 and Test 2. However, Test 2 resulted in the lowest perfusion of the subclavian and carotid arteries with the exception of the RCCA, which experienced a slight 6 % increase from Test 1. The underestimation of perfusion experienced by the subclavian and carotid arteries in Test 1 and Test 2 is most likely because the ML BC creates too much of a restriction on flow rate, which does not account for the geometrical effects on the flow. For example, the momentum of the flow from the AR would ideally force a much larger percentage of flow through the subclavian and carotid arteries. However, the boundary restriction on the predefined velocity due to ML does not allow the perfusion of these arteries to increase based on the geometrical effects. This effect is similar for the traction free BC. The three-element Windkessel however, includes a pressure feedback which is able to account for the geometrical effects. The three-element Windkessel BC is able to allow an equilibrium between the geometrical, resistance and compliance effects of the system, hence preventing the flow at each vessel escalating too high.

Aorta. Tests 1 and 2 both experienced approximately 256 % of flow rate within the TAo when compared against that experienced by Test 3. This almost three-fold increase in perfusion is most likely caused by the previous insufficient perfusion experienced in the subclavian and carotid arteries for Test 1 and 2. Test 1 and 2 again have little discrepancy between the perfusion of the TAo, with Test 1 perfusion being approximately 4 % greater than Test 2.

Being able to accurately predict the perfusion of arterial branches in aortic simulations is important as the risk of ischemic stroke differs substantially for patients with an implanted 'HeartMate II' LVAD [96]. Therefore, in order to be able to apply CFD effectively in the pre-operative planning of LVADs and other devices, it is important to incorporate physiologically accurate BCs.

3.3.2 Time-Averaged Wall Shear Stress

Figure 3.6 visually shows the distributions of the metrics. In order to quantify the changes in these haemodynamic metrics, area-weighted average values in a number of locations are selected, as shown in Figure 3.7. These locations were monitored to quantify how

haemodynamic metrics are affected by each BC, thus numerically highlighting the regions most affected by the prescribed BCs.

Test 1
(Traction Free)

Test 2
(Murray's Law)

Test 3
(Three-Element
Windkessel)
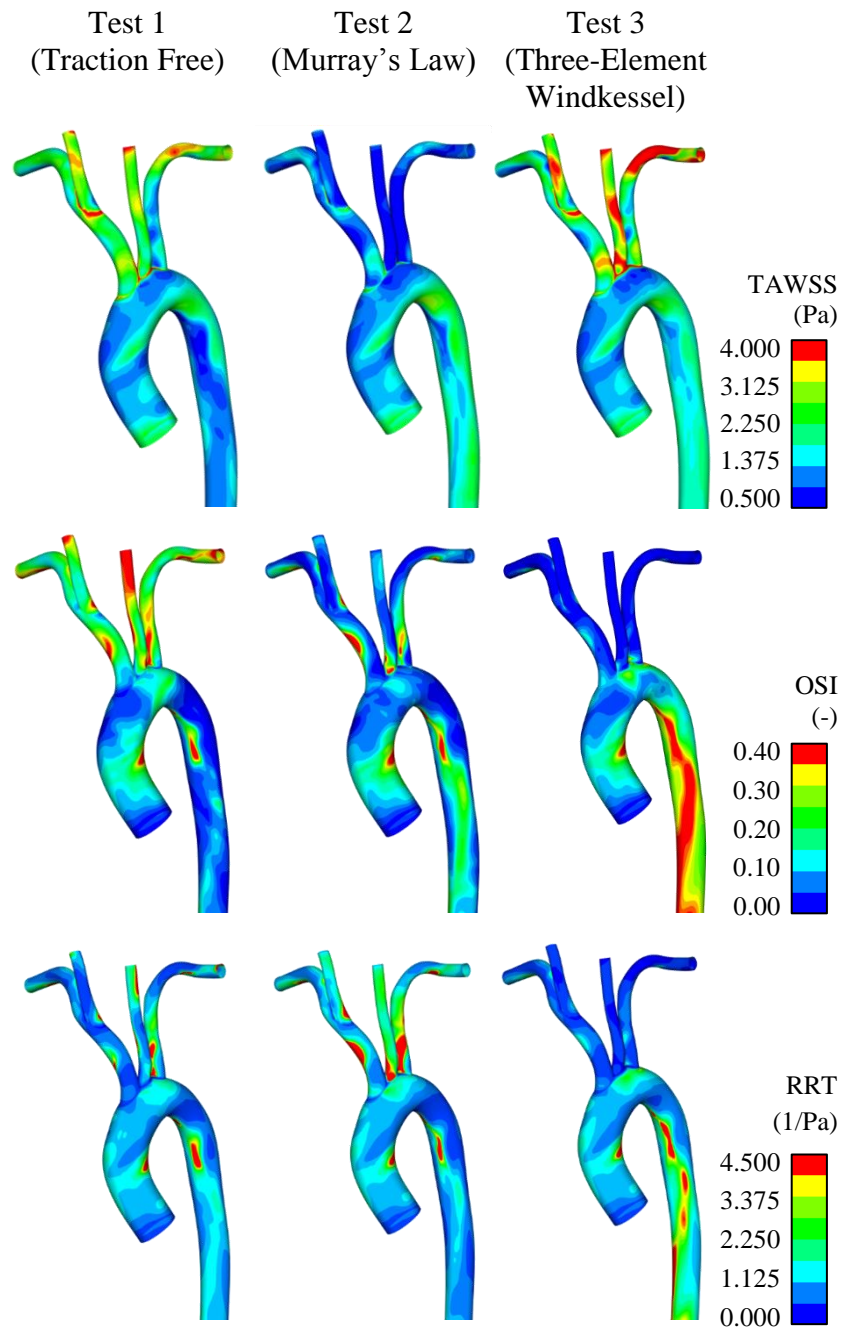
Figure 3.6 - Distributions of various haemodynamic parameters calculated for the aortic arch and descending thoracic aorta, viewed from outside the vessel.
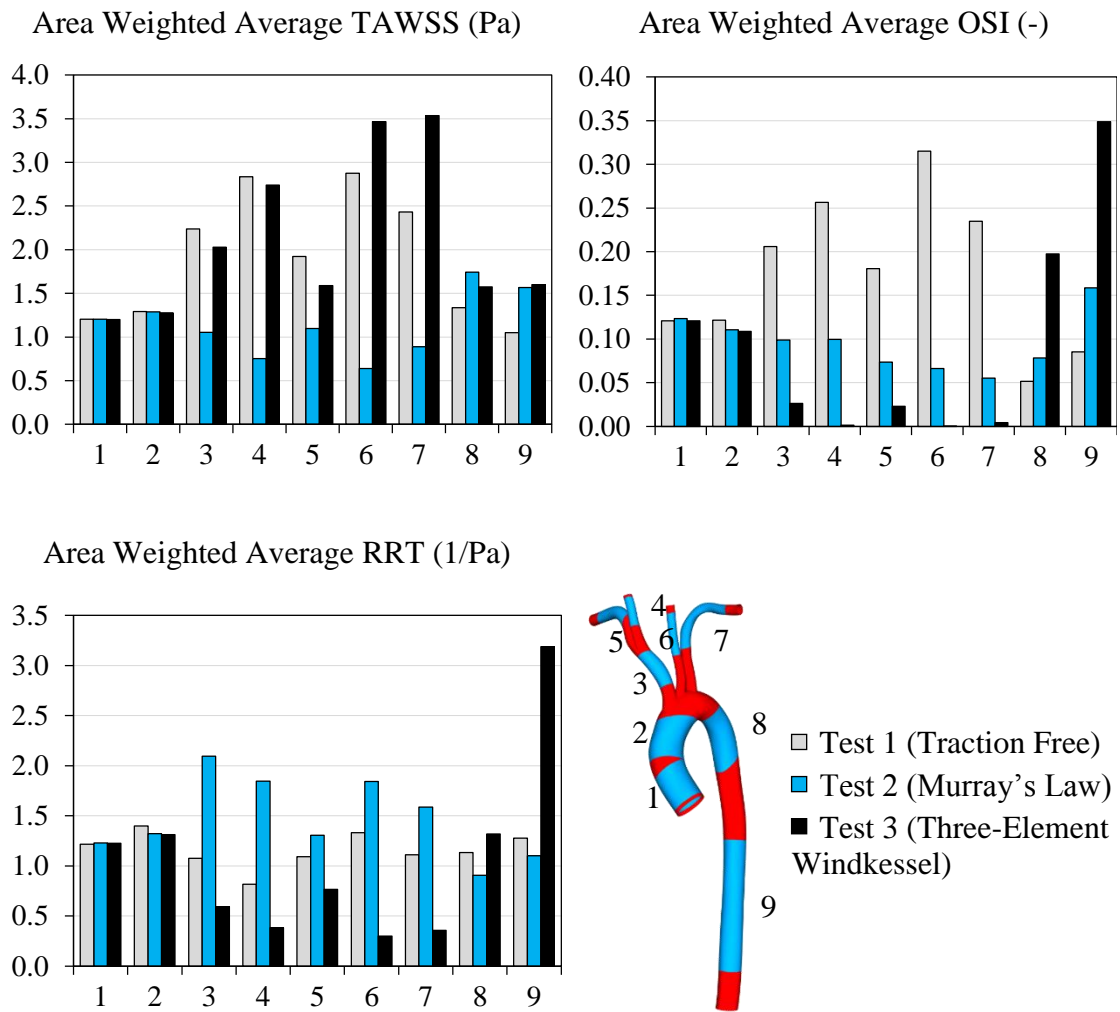
Figure 3.7 - Charts of area-weighted averages of metrics evaluated over various locations illustrated in the bottom right corner.

Each haemodynamic metric will be discussed below separately.

Aorta. As shown in both Figure 3.6 and Figure 3.7, the TAWSS within the AAo (locations 1 and 2) was almost completely unaffected by the outlet BC applied. The TAWSS within the DAo (location 8) was relatively unaffected by the outlet BC, with the traction free and ML BCs producing 15 % lower and 11 % higher TAWSS respectively than the Windkessel BC. In the TAo (location 9), the traction free BC resulted in a decrease in TAWSS of approximately 34 % compared to the Windkessel BC, whilst the ML BC resulted in distributions similar to that of the Windkessel BC.

Subclavian and Carotid Arteries. The TAWSS generally within the subclavian and carotid arteries is similar for the traction free and Windkessel BC, with a maximum discrepancy of -31 % within the LSA. The ML BC however differed significantly in TAWSS from the Windkessel test, with a minimum and maximum discrepancy of -31 % and -81 % within the RSA and LCCA respectively. Thus suggesting that when only

61

investigating the TAWSS metric, the traction free BC is more reliable than the ML BC in producing realistic TAWSS distributions, and produces slightly less pronounced distributions than the Windkessel BC.

3.3.3 Oscillatory Shear Index

Aorta. Similarly to TAWSS, the OSI within the AAo (locations 1 and 2) was almost completely unaffected by the outlet BC applied. The OSI distribution is significantly altered within the DAo and TAo by the applied BC. The OSI distribution becomes more pronounced progressing through Test 1 to Test 3, with Test 3 (three-element Windkessel) experiencing significantly greater regions of OSI with a distinctive axial streak of high OSI down the TAo. This is further supported by the mass flow rate waveforms illustrated in . Notice how the TAo mass flow rate in Test 1 is negative throughout the cardiac cycle, and the other two tests experiencing changes in TAo flow rate from negative to positive. This will be because the Windkessel model allows for the flow to more freely experience reverse flow at the outlet boundaries.

Subclavian and Carotid Arteries. The traction free BC produced significantly overestimated distributions of OSI within the subclavian and carotid arteries. The ML BC also produces over estimated distributions, to a much lesser extent however. These results show that the Windkessel BC produces much lower distributions of OSI in the subclavian and carotid arteries due to its ability to auto-regulate the flow. The Windkessel BC also produces much higher OSI within the TAo than the other two commonly used BCs.

3.3.4 Relative Residence Time

Aorta. Again, the RRT distribution within the AAo was relatively unaffected by the prescribed outlet BC. The DAo was also relatively unaffected. The TAo experienced similar distributions between the traction free and ML BC, however, the Windkessel BC experienced much more elevated RRT within this region (over 2 times greater than both the previous two BCs). Therefore suggesting that the Windkessel BC is better able to capture the stagnant and recirculating flow regions within the TAo than the other two BCs.

Subclavian and Carotid Arteries. Significant discrepancies were again observed within the subclavian and carotid arteries between the outlet BCs applied, with the Windkessel BC producing significantly lower distributions than the previous two BCs. These results suggest that the traction free ($\approx$+160 %) and ML ($\approx$+315 %) BC significantly overestimate the RRT within the subclavian and carotid arteries.

3.4 Limitations & Future Work

Various outlet BC models which are accepted as more physiologically accurate have been ignored during this study. Namely the structured tree model [47], complex Windkessel model [117] and multiscale models [118], which generally account for the behaviour of more vessels within the cardiovascular system than the three-element Windkessel model. Despite these models being able to further reduce modelling error, they are often complex to incorporate into simulations due to the nature of their numerical models, and have therefore been omitted from this study.

The future direction of this work involves comparing commonly used outlet BCs against these more advanced outlet BC models. As well as extending the investigation to a diverse range of human aorta configurations in order to improve the relevance of this work.

3.5 Summary

In the present study, the impact of various commonly used outlet BCs on predicting the localisation of CVDs were assessed for an accurately-represented human female aorta configuration. Three outlet BCs are investigated, traction free, ML and the three-element Windkessel model. The results were compared against the Windkessel model. The results suggest that, i) only when investigating TAWSS, the traction free BC will produce similar distributions to the more advanced three-element Windkessel BC, ii) with the exception of TAWSS, the shear stress based haemodynamics metric distributions varied significantly from test to test, suggesting that the traction free and ML BCs should be avoided whenever possible, iii) OSI was the most affected by the prescribed outlet BC, with the three-element Windkessel producing negligible OSI within the subclavian and carotid arteries compared to the other BCs, and significantly more pronounced axial streaks within the TAo, iv) the three-element Windkessel is better able to capture stagnant and recirculating flow than the other two BCs due to the freedom it allows the flow at the outlets.

CHAPTER 4

IMPACT OF HEART FAILURE SEVERITY ON OPTIMAL VENTRICULAR ASSIST DEVICE CONFIGURATIONS

4.1 Introduction

During the implantation of a LVAD, the inflow cannula connects the left ventricle to the LVAD, while the outflow cannula is anastomosed to the right anterior of the AAo. Although LVADs demonstrate significant survival improvements, they are also associated with postoperative complications, such as thromboembolic events and ischemic stroke due to abnormal haemodynamics [96], [121]. Design and placement of cannulas during both LVAD and Cardio-Pulmonary Bypass (CPB) often varies from surgeon to surgeon, despite both having significant effects on haemodynamics. A number of parameters to consider during cannula placement have been well studied to date, including cannula tip design [60], [93], [122]–[124], cannula insertion angle [93]–[95], [122], [123], [125]–[131] and the effects between pulsatile or continuous flow from the LVAD or CPB machines [132].

Despite there currently being a wide range of research surrounding the aforementioned parameters, to the authors' knowledge, there appears to be no emphasis on the haemodynamic effect of the Flow Ratio (FR) between the LVAD cannula outlet and Aortic Root (LVAD/AR-FR). This ratio varies from case to case depending on different parameters such as the level of HF and the amount of physical activity of the patient. The exact contribution of the remnant native cardiac output to the aortic flow is generally unknown at any given time, however, it can vary from patient to patient anywhere between approximately $5 - 30$ % based on the average cardiac output of 5.08 L·min^{-1} [107], [133]. For example, the 'Heartmate II' LVAD has a built-in feature that syncs the rotor speed with the inlet-outlet pressure differential (due to beating of the heart), thus, the quicker the heart beats, the quicker the LVAD pumps blood [97].

There is scope for work that defines whether or not it is necessary to incorporate the LVAD/AR-FR into the preoperative planning of an LVAD configuration, in order to accurately improve the effects on the cardiovascular system post implantation.

Therefore, the objective of this chapter is to quantify the cardiovascular effects associated with the common range of LVAD/AR-FRs using CFD. In the current study, a parametric

analysis of different LVAD/AR-FRs are examined and compared against a reference solution. A three-element Windkessel model is used in order to accurately capture the physiological back-pressure response of the outlets. Metrics of the perfusion, as well as shear stress based parameters are assessed and discussed, showing the importance of including LVAD/AR-FR in the LVAD performance studies as well as preoperative LVAD planning.

4.2 Method

4.2.1 Geometrical Model

The most common and successful second generation pump worldwide as bridge to transplant and destination therapy is the 'HeartMate II' (Thoratec Corp, Pleasanton, CA, USA) [134]–[136]. The HeartMate II is a continuous flow device connected in parallel to the cardiovascular system by an inlet graft fixed to the apex of the left ventricle, and a 10mm outflow graft anastomosed to the AAo [134], [137]. However, there is a large disparity of Heartmate II patient-specific configurations in the literature in terms of outflow cannula centre line path and anastomosis angle [107]. This has therefore lead to researchers in the field using simplified geometries which tend to capture the common configuration features, such as the anastomosis location, cannula diameter and a simplified cannula centre line path restricted to one plane [120], [138]. The cannula to AAo anastomosis inclination angle for patients with a Heartmate II can also vary significantly (between 29 and 78 degrees) [139]. However, studies have concluded that a shallow anastomosis inclination angle (Φ) of 30 degrees results in the minimum number of thrombi reaching the carotid and vertebral arteries, hence reducing risk of stroke, as well as reducing recirculation zones and low Wall Shear Stresses (WSS) [120], [126], [138]. The simplified cannula centreline path used by Osorio et al. [120] with an inclination angle of ≈30 degrees (Φ) was reconstructed and implemented into this study and is anastomosed to the AAo approximately 10 mm (δ) from the innominate artery, see Figure 4.1. An azimuthal angle of ≈17º (β) is implemented in order to minimise the jet effect from the cannula blocking flow from entering the aortic arch branches, this angle is similar to patient-specific azimuthal angles found in the literature [106], [107]. The cannula geometry (10 mm diameter) is digitally anastomosed to a patient-specific model of a 23-year old female with normal aortic function and an AR diameter of 20 mm. The patient specific geometry was produced using SimVascular software package (https://simtk.org) to process gadolimium-enhanced MRA image data [63].

65
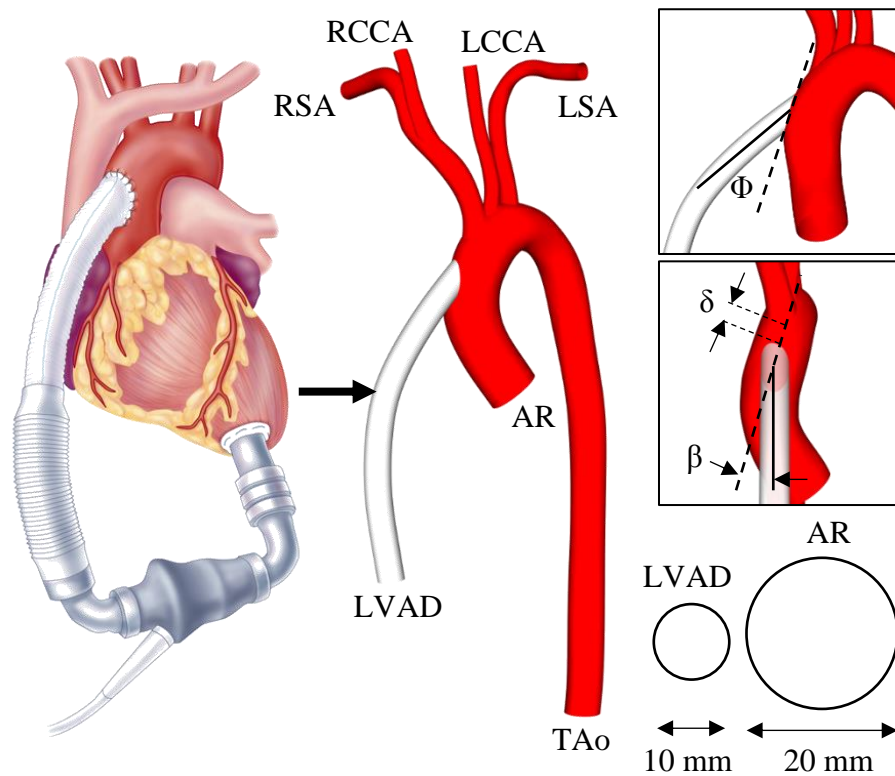
Figure 4.1 – A typical 'HeartMate II' configuration is illustrated on the left hand side of this figure and has been taken from Hobbs & Boyle [142]. The right hand side is a schematic of the present configuration consisting of an aorta (that of a 23-year old female) with normal aortic function with an LVAD outflow graft connected to the AAo. Inlets: AR and LVAD outflow graft. Outlets: RSA, RCCA, LCCA, LSA and TAo. Inclination angle, $\Phi \approx 30°$. Azimuthal angle angle, $\beta \approx 17°$. Distance from innominate artery, $\delta \approx 10$ mm, similar to that used by Osorio et al. [120].

4.2.2   Computational Domain

The geometry was meshed using ANSYS-Meshing (Version 17.1). The mesh was based on a finite volume hybrid mesh consisting of tetrahedral elements within the core region and prism layers (3 elements thick) near the wall to allow for large spatial velocity gradients. In order to ensure the accuracy of the simulations, a series of six steady-state computations with various mesh refinement levels (ranging from 2.3 to 5 million elements) were conducted to ensure mesh independency. In these simulations, input flow rates from the AR and cannula were 30 and 70 % of the total flow rate, respectively. The results were compared by measuring the spatial mean WSS over regions of the anastomosis and the RSA, LCCA and TAo. Refinement from ≈2.3 million to ≈3.3 million elements resulted in a maximum change in spatial WSS of 0.48 %. A one-dimensional velocity profile was also monitored at a point, 20 mm distal of the anastomosis, where the peak velocity changed by 1 % from 2.3 to 3.3 million elements and was insignificantly

affected with further mesh refinement. Therefore, the mesh of ≈3.3 million elements was considered adequate and used for the cannula and aorta configurations. For a control model, in which there is no cannula, no mesh independency test was conducted. However, a finer mesh with almost equal element count of ≈3.3 million elements (due to the less complex domain shape) was deemed adequate, and hence chosen.

4.2.3 Boundary Conditions

As shown in Table 4.1, seven tests are studied in this work. 'Test 0' is used as a representative of normal aortic haemodynamics for comparison purposes, which does not include a cannula. 'Tests 1-6' represent a patient with an implanted LVAD suffering from various extents of HF. In all tests, a no-slip BC is applied to all walls and a rigid wall model is assumed, which has been shown to be a valid assumption [61], [111]. Details of the inlet and outlet BCs are shown in Table 4.1 and Figure 4.2 and will be described next.

Table 4.1 – Summary of cases studied in the present work. Constant LVAD cannula flow rates were obtained by time-averaging the healthy pulsatile flow rate and scaling accordingly. Percentage values represent the boundary's contribution to the total aortic flow rate. 'Test 0' is a control model, in which heart function is normal and there is no LVAD outflow graft.

	Time-averaged native heart flow rate (L·min^{-1})		Constant magnitude LVAD cannula flow rate (L·min^{-1})	
Test 0	3.192	(100 %)	-	
Test 1	0.958	(30 %)	2.234	(70 %)
Test 2	0.798	(25 %)	2.394	(75 %)
Test 3	0.638	(20 %)	2.553	(80 %)
Test 4	0.479	(15 %)	2.713	(85 %)
Test 5	0.319	(10 %)	2.873	(90 %)
Test 6	0.160	(5 %)	3.032	(95 %)
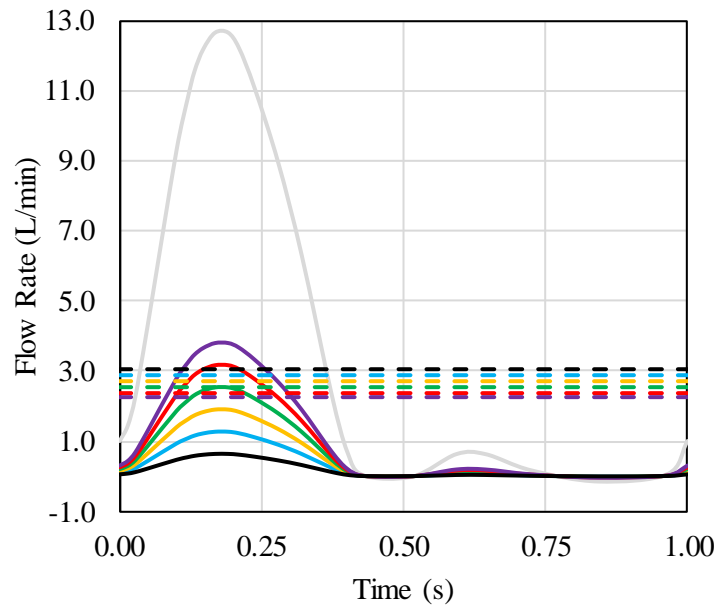
Figure 4.2 – Inlet flow rates profiles adapted from the patient-specific PC-MRI waveforms obtained via LaDisa et al. [63]. Waveforms have been scaled (based on the patient's healthy flow rate) to account for the cardiac output of the patient per test, refer to Table 4.1.

Inlets. For all tests, a uniform velocity profile was imposed at the inlets, refer to Figure 4.2. The assumption of a flat velocity profile at the aortic inlet has been verified by various *in vivo* measurements using different animal models, which have demonstrated that the velocity profile distal to the aortic valve is essentially flat in the AAo and only consists of a weak helical component [49]. For 'Test 0', the patient-specific PC-MRI waveform by LaDisa et al. [63] was applied to the AR. 'Tests 1-6' scaled this AR waveform by 5 to 30 % in increments of 5 % (corresponding to LVAD/AR-FRs between 70 to 95 %). A constant flow rate from the cannula compensated for the unfulfilled total aortic flow to bring total the flow rate for all tests to 3.2 $L \cdot min^{-1}$ (in accordance with the *in vivo* flow rate by LaDisa et al. [63].

Outlets. In order to ensure physiological haemodynamics, the 3D domain is coupled to a three-element Windkessel model in this study using a Fortran subroutine. Refer to Section 1.4.4 for a detailed explanation of the implementation. The Windkessel parameters are given in Table 1.1.

4.2.4 Numerical Procedure

The CFD solver ANSYS-CFX (Version 17.1) was used for the simulations. Blood was defined as a three-dimensional, incompressible and isothermal fluid. Dynamic viscosity and density of the blood are set to 0.004 Pa·s and 1060 kg·m^{-1}, respectively [120]. The maximum Reynolds number, based on the cannula diameter (10 mm) and maximum cannula velocity (zero native heart cardiac output), was calculated to be ≈1750, therefore, a laminar model was used for all simulations. In accordance with similar works, non-Newtonian fluid properties are neglected [53], [54], [86], [140].

A fully implicit second-order backward Euler differencing scheme is used. Each simulation is ran for 4 cardiac cycles (4 s) with a timestep size of 1.25 ms and 10 coefficient loops per timestep, this proved adequate in order to allow the boundary flow rate and pressure waveforms to converge, see Figure 4.3. The results are recorded during the final cardiac cycle. The commercial visualisation tool, Ensight 10.1.6 was used to post-process the results.
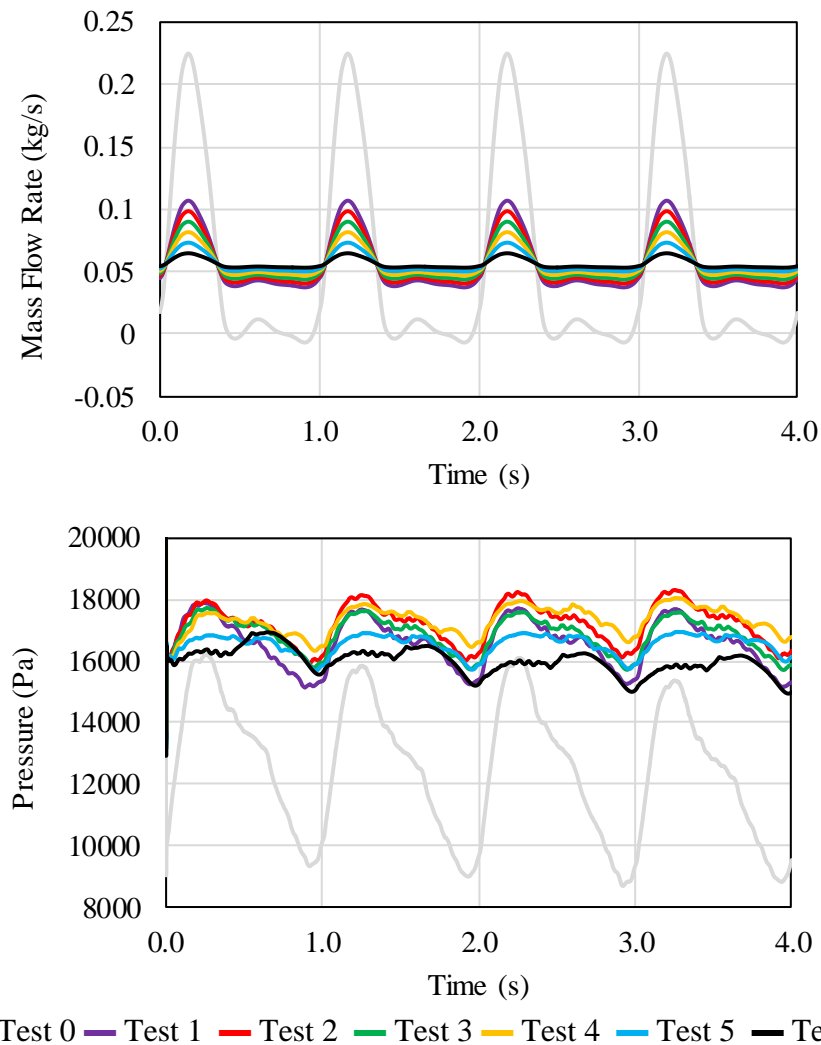
Figure 4.3 – Total mass flow (AR+LVAD) and volume average pressure waveform history of Tests 0-6. The pressure waveforms are sufficiently converged on the fourth period. The volume average pressure waveforms are similar to that produced by the boundary specific waveforms. Therefore, results are recorded during the fourth period. For Test 0, the fourth period results correlate to producing a physiologically realistic blood pressure of 15131/8781 Pa (113/66 mmHg). Initial flow rate is set to zero for all tests. P_n and P_{n-1} are initialised with values of 9240 Pa for Test 0, and 15240 Pa for Tests 1-6.

4.3   Results & Discussion

4.3.1   Introduction

The haemodynamics in 'Test 0' are assumed to be ideal as it is representative of the haemodynamics in a healthy patient without any invasive devices or cardiovascular dysfunction. Therefore, any comparisons will use 'Test 0' as a benchmark. The TAV (including arterial perfusion) and shear stress-based haemodynamic parameters are

70

discussed separately, followed by a brief comparison of what the conclusions would be if a conventional and still common zero-pressure outlet BC were used in this study. Finally, the limitations and future direction of this work will be outlined.

4.3.2 Time-Averaged Velocity

In this section, through a range of LVAD/AR-FRs, the effects of the LVAD implementation on the perfusion of the aortic branches for different levels of HF is examined against Test 0. In order to measure the aortic perfusion, TAFR and TAV are calculated over one cardiac cycle in order to examine the perfusion of vessels and general haemodynamics. Figure 4.4 provides a quantitative approach to assess the TAFR, whilst Figure 4.5 and Figure 4.6 show a more qualitative illustration of TAV using isosurfaces and streamlines, respectively.
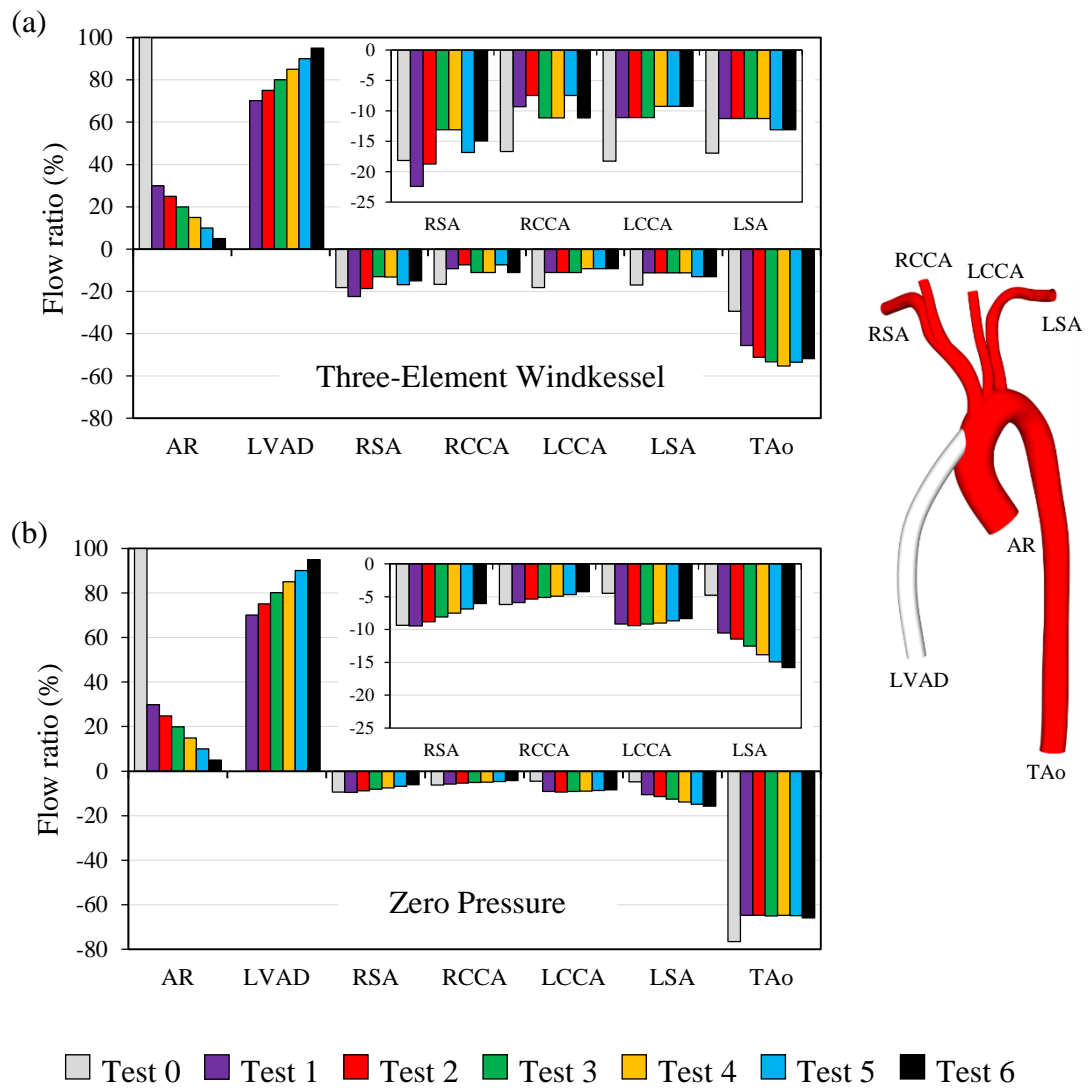
Figure 4.4 – Ratio (%) between the TAFR through the corresponding artery and the total TAFR through the system. Positive and negative ratios represent inlets and outlets, respectively. (a) Simulations that incorporated a three-element Windkessel model at the outlet boundaries. (b) Simulations that implemented a zero-pressure at the outlet boundaries.
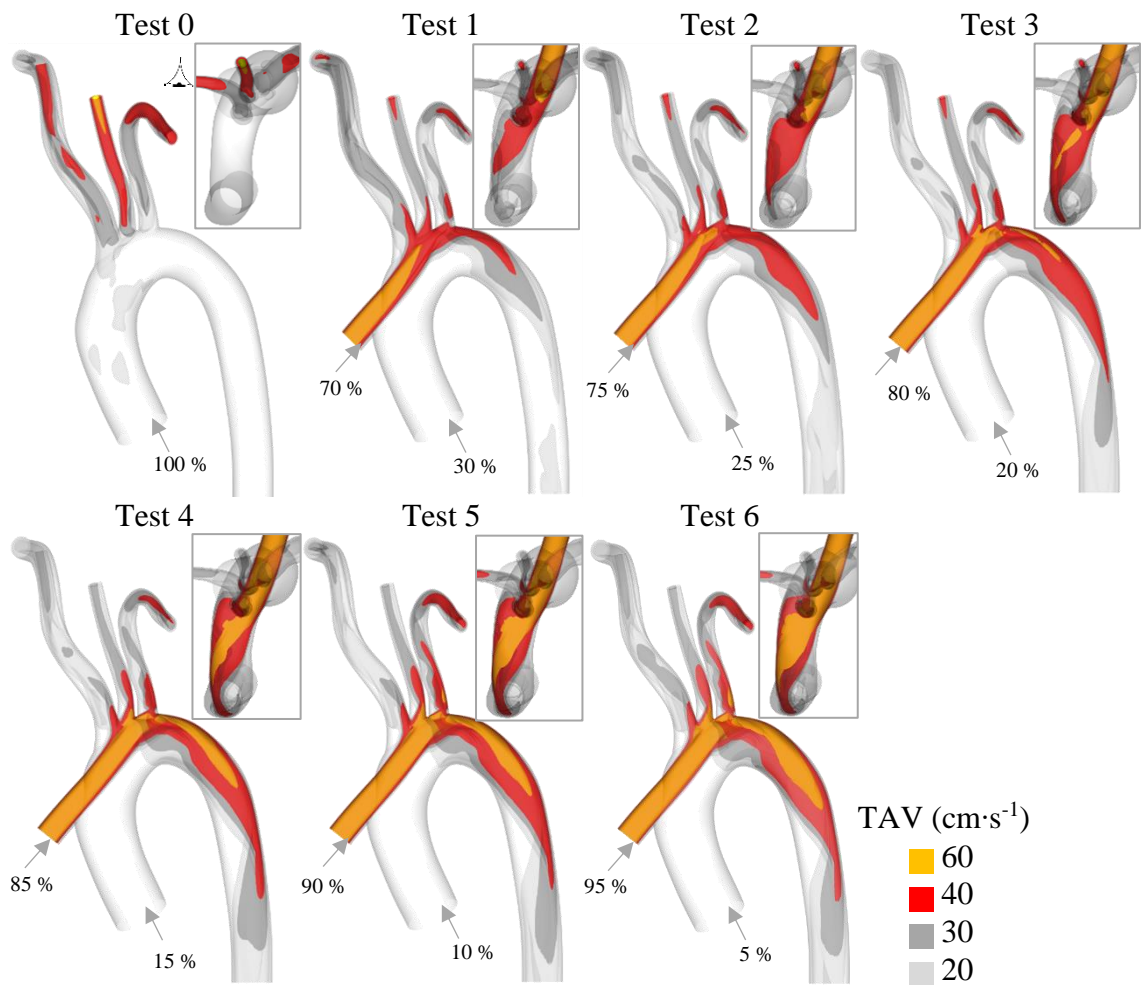
Figure 4.5 – Isosurfaces of TAV within the aortic arch. Four isosurfaces from within the mid-high range of velocity are shown. Percentage values represent the TAFR through the corresponding inlet over one cardiac cycle.
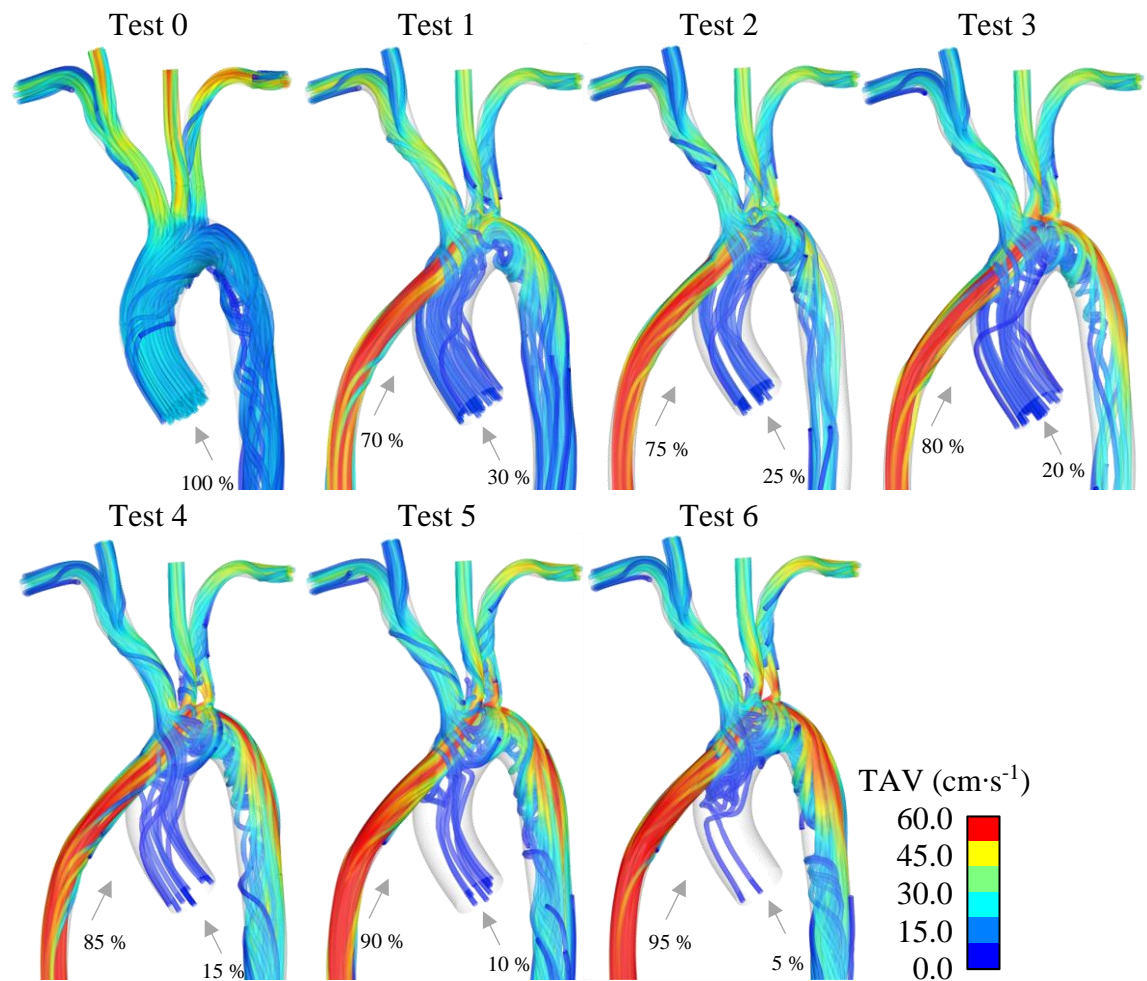
Figure 4.6 – Time-averaged blood flow velocity streamlines coloured by TAV.

The results show that none of the geometries including an LVAD outflow cannula (i.e. 'Tests 1-6') experience normal perfusion; this also supports common findings in the literature [93]–[95].

Subclavian and Carotid Arteries. Outlets RSA, RCCA, LCCA and LSA for 'Tests 1-6' (shown more clearly in an inset in Figure 4.4) all experience an insufficient amount of flow compared to 'Test 0', with the exception of the RSA in Tests 1 and 2. The average perfusion of the subclavian and carotid arteries in most of the tests is approximately 69 % of what is deemed to be healthy. The general drop in flow rate to the subclavian and carotid arteries is mainly due to the jet from the cannula adding a blocking effect to flow from the AR entering the subclavian and carotid arteries. A clear distinction is observed in Figure 4.4 between the left and right carotid and subclavian arteries in relation to their sensitivity to different LVAD/AR-FRs. Specifically, both the LCCA and LSA maintain an almost constant outflow rate, showing minor changes in TAFR percentages for different LVAD/AR-FRs. On the contrary, the RCCA and RSA flow rates produce an irregular pattern as LVAD/AR-FR increases. The fluctuation of the RSA and RCCA flow

rate is mainly due to their close proximity to the anastomosis, hence experiencing more disturbed flow. Whilst the insensitivity of the LCCA and LSA to LVAD/AR-FR is mostly likely due to the three-element Windkessel model creating a stronger auto-regulatory effect on flow due to their smaller diameter (greater proximal and distal resistances).

Aorta. The TAo generally experiences around 176 % of normal TAo perfusion for Tests 1-6. This is due to the underperfusion observed earlier to the subclavian and common carotid arteries, as well as the high velocity cannula jet mainly being directed to the DAo. The level of perfusion to the TAo is closely related to LVAD/AR-FR, increasing from Test 1 to 4, peaking at Test 4, and then beginning to decrease.

It is worth noting that the perfusion experienced in this study should not be assumed to be experienced by all patients. Over a study of 956 patients with the 'HeartMate II' LVAD, the risk of ischemic stroke differed substantially [96]. The abnormal perfusion experienced in this study combined with the unclear pattern of ischemic events leads to the need of more thorough ways to predict the risk of such events on a patient-by-patient basis.

4.3.3 Shear Stress-Based Haemodynamic Parameters

The localisation of various lesions including atherosclerosis and thrombosis have been extensively studied and are shown to be related to different local haemodynamic metrics [72], [73], [75], [108]. These haemodynamic parameters can be directly derived from the flow velocity fields obtained by CFD-based simulation tools. In the present study, these parameters are used as a tool to study whether the haemodynamics are favourable or detrimental to the health of the patients with an LVAD and to help identify some characteristics of disturbed flow that are of pathobiological importance. The wall-based parameters chosen for the present analyses include WSS, Time-Averaged WSS (TAWSS) [78], Oscillatory Shear Index (OSI) [78] and Relative Residence Time (RRT) [77]. These parameters have been chosen because (i) localised distribution of low-WSS and high-OSI strongly correlate with the locations of atheroma [78], (ii) platelet activation may be induced by the combination of large exposure time and high shear stress [80]–[83], and (iii) stagnant and recirculating flow regions can cause platelet aggregation and thrombosis [84]. Figure 4.7 shows the distributions of the above metrics. For a more quantitative comparison, Figure 4.8 shows area-weighted average values of the metrics evaluated over various locations within the aorta model. In what follows, each wall-based haemodynamic metric will be discussed separately.
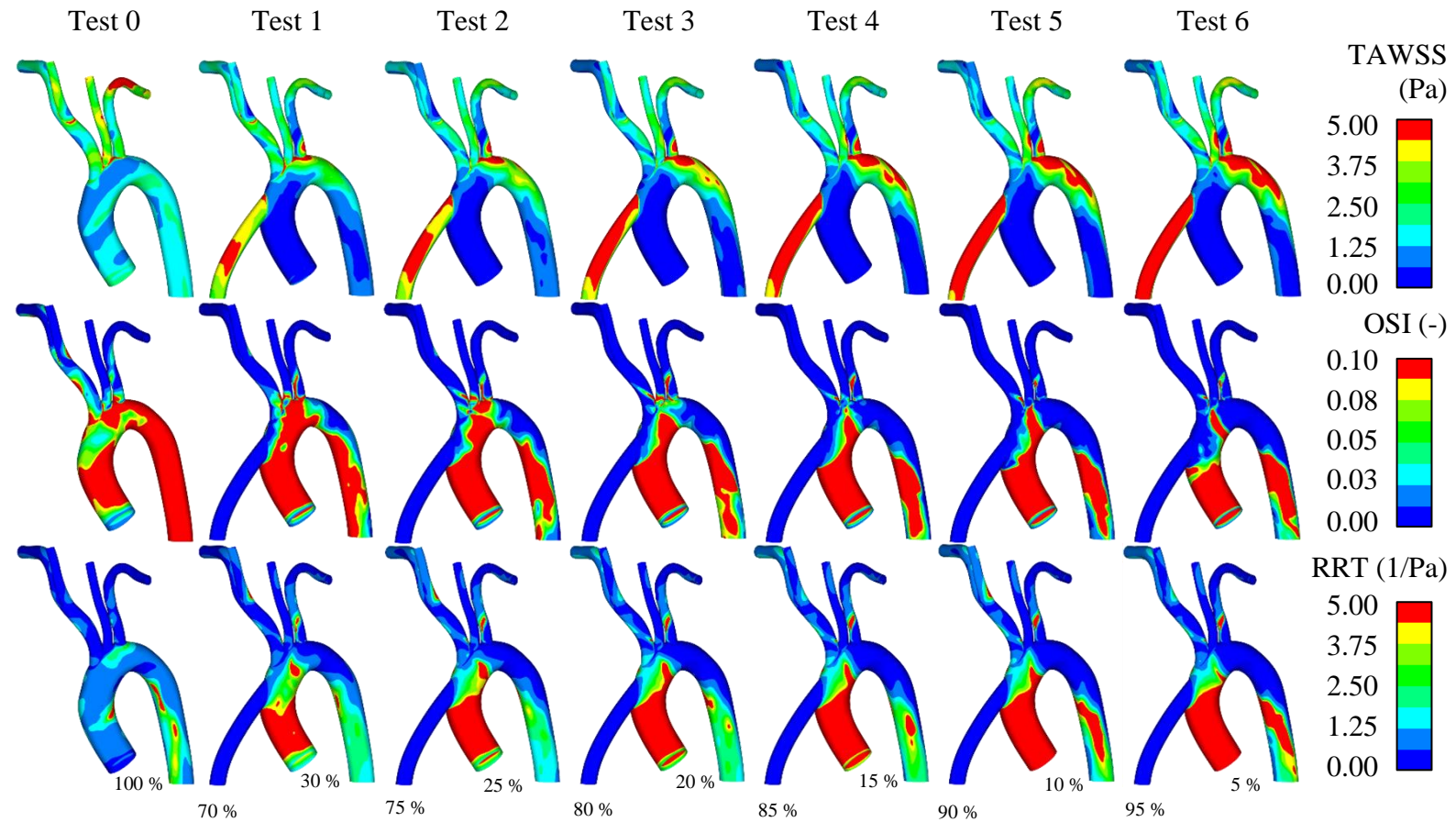
Figure 4.7 - Distributions of different haemodynamic parameters calculated for the aortic arch and descending TAo, viewed from outside the vessel. LVAD/AR-FR increases from left to right (as shown by the percentages).
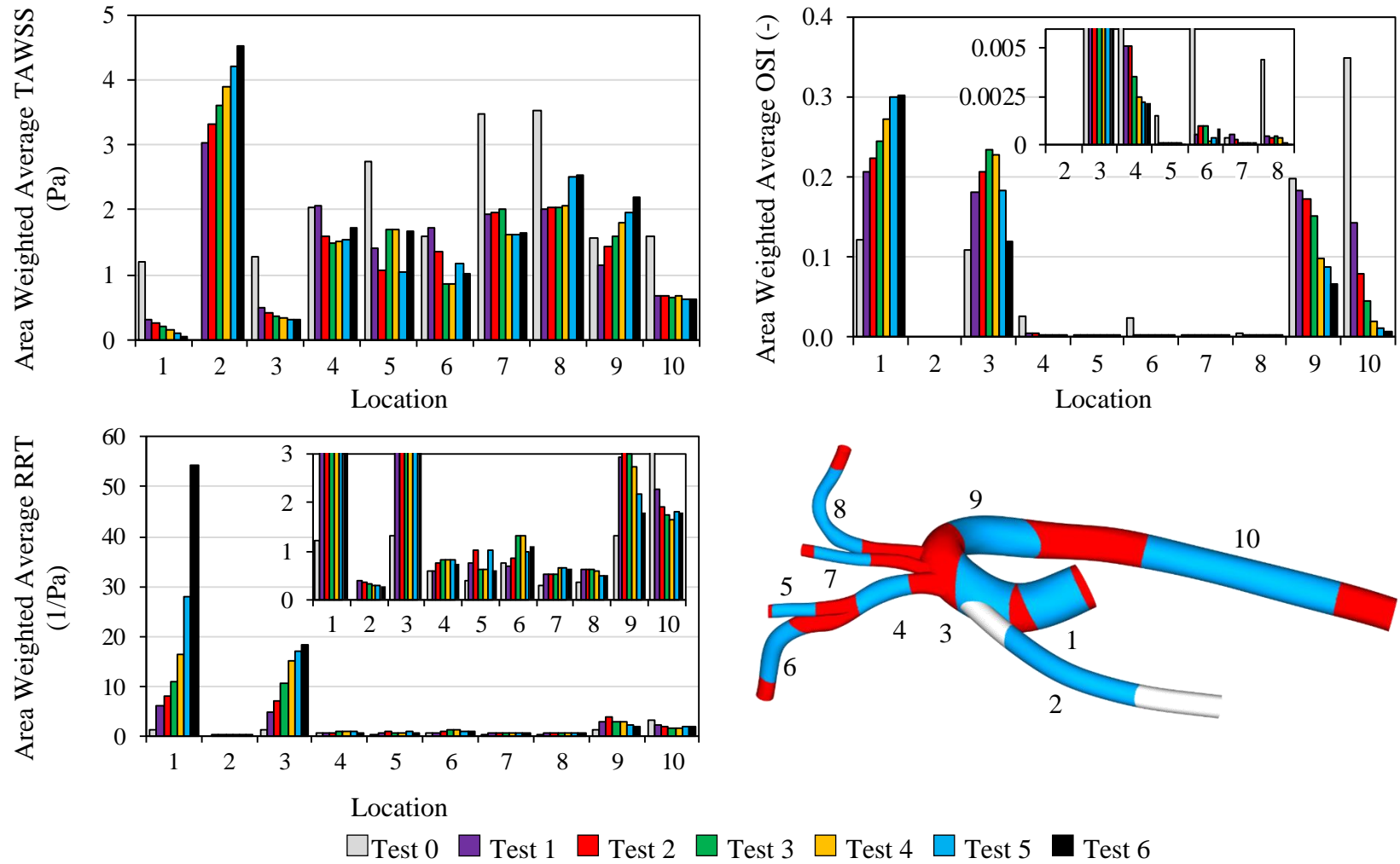
Figure 4.8 – Area-weighted average values of TAWSS, OSI and RRT at ten monitored locations within the geometry. LVAD/AR-FR increases from Test 0 through to Test 6.

Time-Averaged Wall Shear Stress. When comparing 'Test 0' with 'Tests 1-6' in Figure 4.7, the latter all experience much less evenly distributed WSS, with generally higher WSS in aortic arch and DAo, whilst the WSS is lowered in all other locations. This is due to the cannula flow inducing non-physiological haemodynamics and disturbing the WSS distribution [125]. The flow in 'Test 0' may be a typical example of 'form follows function', as the human AAo is said to be insusceptible to atherosclerotic plaque formation [141]. 'Test 0' does not produce these extreme distributions of WSS as the form has likely developed in such a way to maintain a relatively smooth distribution of WSS. Similar to the TAV and TAFR results presented in the previous section, Figure 4.8 shows that different branches exhibit different degrees of sensitivity to increasing the flow from the LVAD.

TAWSS within the subclavian and carotid arteries changed in an irregular manner as LVAD/AR-FR increased (locations 4-8 in Figure 4.8). The TAWSS generally reduced by 22 % within the innominate artery and stayed relatively constant through Test 2 to 6, with the exception of Test 1, which increased slightly (+2 %). Despite the TAWSS within the subclavian and carotid arteries fluctuating as LVAD/AR-FR increases, an overall decrease in TAWSS of 40 % was generally experienced.

The DAo initially experienced a drop in TAWSS of 28 %, but then began experiencing a steady increase in TAWSS of approximately 13 % per test, until equalling the healthy TAWSS at Test 3, and continuing to Test 6 with a relatively constant gradient. Figure 4.5 suggests that the more severe the HF, the larger and more intense the shear stress streak on the DAo becomes due to the higher cannula jet velocity, which is required to maintain adequate overall flow rate. This phenomina is also illustrated by the TAV and streamlines shown in Figure 4.5 and Figure 4.6.

The AAo experienced a relatively linear negative relationship between TAWSS and LVAD-AR-FR. Test 1 experienced a sudden decrease in TAWSS by 62 %, then steadily decreased by ≈3 %. This shows that the AAo is less sensitive to changes in TAWSS by altering the LVAD/AR-FR, but experiences a much lower TAWSS by simply introducing an LVAD into the model.

TAWSS within the TAo in Test 1 initially reduces by 60 %, then remains relatively constant regardless of LVAD/AR-FR.

Oscillatory Shear Index. The subclavian and carotid arteries (as shown in Figure 4.7 and Figure 4.8) all experience much lower OSI compared to Test 0. The innominate artery

experiences a clear negative relationship between OSI and LVAD/AR-FR, this is due to its close proximity to the anastomosis, hence, it experiences a direct effect of the cannula flow rate. The other peripheral arteries however experience an almost zero value of OSI, most likely because, i) continuous flow from the LVAD dominates the pulsatile flow from the AR, and ii) the three-element Windkessel model has a high auto-regulatory effect on the flow within the smaller vessels as previously discussed.

The AAo (location 3) experiences a significant increase in OSI from Test 1-3, peaking at Test 3 (+116 %), and then significantly decreasing again until reaching almost healthy values of OSI at Test 6. Elevated-OSI magnitudes in location 3 indicate a disturbed flow occurring in the aortic arch distal to the cannula attachment point, where the LVAD and AR flows are mixing.

The AR (location 1) experiences the greatest increase of OSI when compared against the reference case, with a strong positive correlation to LVAD/AR-FR. The main reason for such haemodynamic modification is the high velocity flow stream from the cannula tends to block and divert the pulsatile flow from the AR. The above results along with the findings of He & Ku [78] suggest that the AAo may suffer from an increased probability of atheroma development. It is also noted that the extent of this phenomenon is unlikely to be improved by the cannula tip positioning and configuration, based on positioning restrictions.

The DAo and TAo both experienced a negative relationship between LVAD/AR-FR, with the TAo being the most sensitive, the OSI value within the TAo approximately halved each time the LVAD/AR-FR increased.

Relative Residence Time. RRT in the subclavian and carotid arteries slightly increases when compared to Test 0 with no clear correlation to LVAD/AR-FR, this is most likely insignificant however as the values of RRT are minimal.

The AR and AAo (locations 1 and 3) experience significantly elevated RRT with strong correlations to LVAD/AR-FR. The elevated RRT within the AR and AAo is again due to the cannula flow blocking and diverting the pulsatile flow from the AR.

The DAo and TAo experience regions of high RRT streaks which increase in size as LVAD/AR-FR increases (this is shown most evidently in Figure 4.7).

The AR, AAo, DAo and TAo are at serious risk for Tests 5 and 6 as these regions are experiencing significant stagnant and recirculating flow, which can cause platelet aggregation and thrombosis [84].

4.3.4 Effects of Using Conventional Zero Pressure Boundary Condition

Despite more reliable methods existing, it is still common amongst the cardiovascular research community to use simpler outlet BCs such as zero pressure [38], [50], [86], [105]–[109]. Running Tests 0-6 using a conventional zero-pressure BC for all outlets produces significantly different results and misleading conclusions when compared against using a three-element Windkessel model, this is observed by comparing the TAFRs in Figure 4.4a and Figure 4.4b. Using a three-element Windkessel model concludes that the TAFR to the subclavian and carotid arteries is highly irregular and is overall reduced when compared against a healthy patient without an LVAD. Contradictory, when using the zero-pressure BC, the subclavian and carotid arteries were less sensitive to the LVAD/AR-FR and behaved in a much more regular manner. Using the zero-pressure BC also suggests that the LCCA and LSA are over perfused regardless of LVAD/AR-FR, the opposite is however true for the simulations that included a Windkessel model. Perfusion to the TAo using the zero-pressure BC was relatively unaffected by LVAD/AR-FR. This again shows the importance of using a physiologically accurate BC when investigating haemodynamics within the aorta [43], [49], [50], [99], [100], [102].

4.4 Limitations & Future Work

Due to the LVAD and aorta configuration in reality changing vastly from patient to patient, the results of this work only act as an indicator of the importance of incorporating the patient specific LVAD/AR-FR into the patient specific preoperative planning of the optimum cannula angle, design and location. Doing so will improve the effects on the circulatory system post LVAD implantation.

Further studies are required in order to test the value of the LVAD/AR-FR on a wider range of LVAD configurations. Due to the sparsity of relevant data required to conduct a rigorous quantitative study of multiple patient-specific configurations, a more qualitative approach has been taken to assess the significance of the LVAD/AR-FR [45].

Fluid-structure interaction was omitted in this study as it has been shown to have an insignificant effect on the results for similar studies [61], [111]. However, furthering this

work by incorporating fluid-structure interaction may provide some additional insight that was not able to be captured in the present work.

Finally, the outcome of the present study concerning the implantation of LVAD outflow cannula is also applicable to CPB to some degree. However, it is worth noting that the velocity from the cannula returning blood during CPB is often significantly higher than LVADs, thus increasing the risk of dislodging parts of atherosclerotic lesions, creating an emboli, which can ultimately result in stroke [93].

4.5 Summary

A patient-specific aorta model with normal aortic function was used to study the importance of incorporating the severity of HF in the computational preoperative planning of an LVAD configuration. The results were compared against a control model which did not include an LVAD graft and used patient-specific BCs, this model represented healthy aortic haemodynamics. The general irregular behaviour of the subclavian and carotid arteries to LVAD/AR-FR indicates that the perfusion and WSS-based haemodynamic metrics within these arteries cannot be accurately predicted unless the LVAD/AR-FR is incorporated into the computational preoperative planning of the optimal LVAD configuration. The consistently excessive perfusion to the TAo suggests that regardless of LVAD/AR-FR, the TAo will most likely experience adequate perfusion.

CHAPTER 5

GEOMETRICAL ACCURACY ENHANCEMENT OF CORONARY ARTERIES FOR HAEMODYNAMIC SIMULATIONS

5.1 Introduction

Atherothrombosis is the major cause of cardiovascular death and is the leading cause of mortality in the developed world, with most atherosclerotic lesions occurring within the Left Anterior Descending (LAD) coronary artery [12], [14], [143], [144]. Although antithrombotic therapy is considered safe and effective, the morbidity and mortality rate due to atherothrombosis remains too high [143]. Acute myocardial infarction is caused by the sudden rupture or ulcer formation of vulnerable plaque, followed by subsequent thrombosis and significantly restricted blood flow [145]–[147]. Endothelial erosion and rupture are known to be associated with local flow conditions as well as biological factors, with plaques most frequently developing in close proximity to bifurcation sites [13], [14].

CFD is able to offer valuable insight into the local flow conditions within a coronary artery. Using imaging data from patients that have coronary artery pathology, with the use of CFD it is possible to simulate patient-specific haemodynamics within the artery. Comparisons can be made of haemodynamics both with and without pathology included in the geometrical reconstruction. This allows for a before and after pathology comparison, which enables correlations of haemodynamic metrics and risk of coronary pathology to be developed. Developing correlations between haemodynamic metrics and risk of erosion/rupture sites will enable better-tailored treatment for patients diagnosed with coronary artery pathology [14], [45].

Non-invasive visualisation of coronary arteries has significantly improved over the past 20 years [148]. Current non-invasive cardiac imaging techniques include MRA and Computed Tomographic Angiography (CTA). These techniques however are limited in their ability to capture a high-resolution image. This has led to intravascular imaging techniques being developed [147]. Intravascular imaging techniques generally use a catheter with an attached imaging device to capture images of the arterial lumen more accurately. Currently available intravascular imaging techniques include fractional flow reserve; grayscale Intravascular Ultrasound (IVUS); IVUS radiofrequency tissue

characterisation; Optical Coherence Tomography (OCT), the light analogue of IVUS; and near-infrared spectroscopy [149]. In daily clinical practice, these imaging techniques are used to investigate the causes of lesion deposition around a stent, or to decide which plaque is most vulnerable, amongst others [149]. However, researchers have begun using these imaging techniques to further the understanding of CVD pathology.

Researchers have previously attempted to image and reconstruct coronary arteries in preparation for CFD investigation using both non-invasive and intravascular imaging techniques. Slager et al. [150] managed to fuse together IVUS and angiographic information to account for the curved path of the artery. Recent work by Timmins et al. [79] reconstructed a relatively accurate coronary artery model by fusing together MRA views with IVUS image segments using what is known as the ANGUS technique, similar to other work in the literature [76], [151]–[153]. The ANGUS technique involves the stacking of IVUS segments perpendicular to the catheter centreline at specific locations determined by the catheter pullback speed [153]. Timmins et al. [79] observed patients (n=20) with coronary plaque progression over a period of six months. They were able to demonstrate that, in patients with non-obstructive coronary artery disease, regions subjected to low and oscillatory WSS demonstrated progression of atherosclerotic lesions. This study coincides well with the current accepted theory that low and oscillatory shear stress increases risk of atherosclerosis progression [15]–[19]. Despite the valuable work by Timmins et al. [79], the limitation of using IVUS with a relatively low resolution (100 to 200 µm) is apparent as it is not able to accurately capture the details of the vascular wall and modifications [14], [154].

Furthermore, intravascular OCT has emerged as an attractive new imaging technique, which offers superior resolution (10 to 15 µm) that can image both plaques and thrombi with considerably more accuracy than IVUS and angioscopy [14], [147], [154]. Despite IVUS and CTA being able to accurately calculate the haemodynamics within the artery, these techniques are unable to accurately capture the structure of the plaque [155]. Incorporating OCT image segmentations for reconstructing geometry and observing coronary plaque morphology could significantly improve the impact of such studies [156]. Ha et al. [156] has attempted stacking together OCT segments with the major limitation of not accounting for the curvature of the artery within the geometric model. Geometries have also been reconstructed by stacking OCT segments along a centreline (similar to the ANGUS technique), which were used for calculating WSS using CFD

methods [155]. However, work by Toutouzas et al. [155] is limited, as the cross-sections appeared to be simplified as a circle based on the average diameter at each segment, similar to how geometry is reconstructed from MRA images.

<center>(a)   (b)</center>
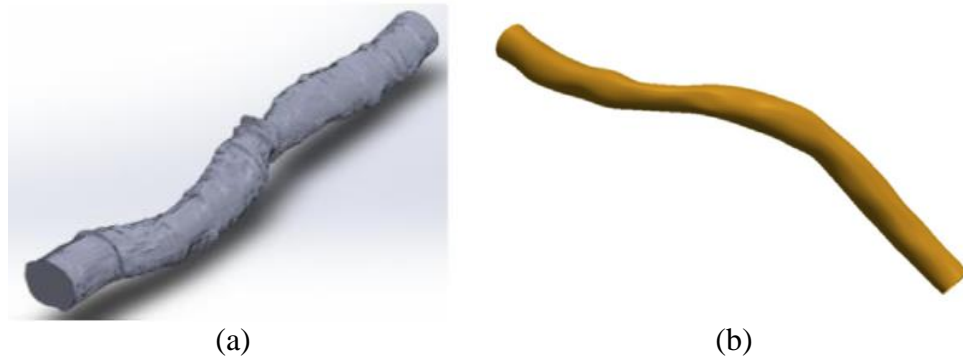
Figure 5.1 – Illustration of the latest in fusing together OCT and MRA images to create a coronary geometry model. (a) OCT stacked along a straight line and lofted together to create a surface [156]. (b) seemingly simplified OCT segments stacked along an angiographic image derived centreline [155].

In light of the above and after reviewing the literature, there appears to be a need to more accurately model the geometry of the coronary artery system in order to perform CFD simulations to correlate haemodynamic metrics with acute disruption/thrombus formation. There is potential for hybrid methods of non-invasive and intravascular imaging techniques to be developed that are able to combine the curvature of the vessel with the accuracy of intravascular imaging in order to accurately represent the vessel lumen, specifically capturing small details and accurate luminal cross sectional curves.

Therefore, the objective of this chapter is to develop a novel non-invasive/intravascular hybrid approach in accurately reconstructing a coronary artery luminal surface, which can be used for CFD studies to predict acute disruption/thrombus formation.

5.2   Method

5.2.1   Geometrical Reconstruction

A single OCT/MRA hybrid geometrical model is reconstructed in this study. Merging OCT segments with MRA data to accurately capture the surface contour as well as the curvature of the model has not been achieved until now. Previous studies have attempted to achieve this but have either not captured the curvature of the artery centreline, or not represented the arterial wall in enough detail [155], [156].

A semi-automated procedure was developed in this work using five software packages. An estimated manual reconstruction time is approximately four days, estimated by extrapolating from the time required to perform repetitive tasks. The automated process developed in this work reduces the reconstruction time per patient to approximately 4 hours. The most significant time reduction is found within Step 5, by automating the stacking of the OCT segments to the centreline of the artery. The details of each step will now be explained separately, and are illustrated in Figure 5.2.
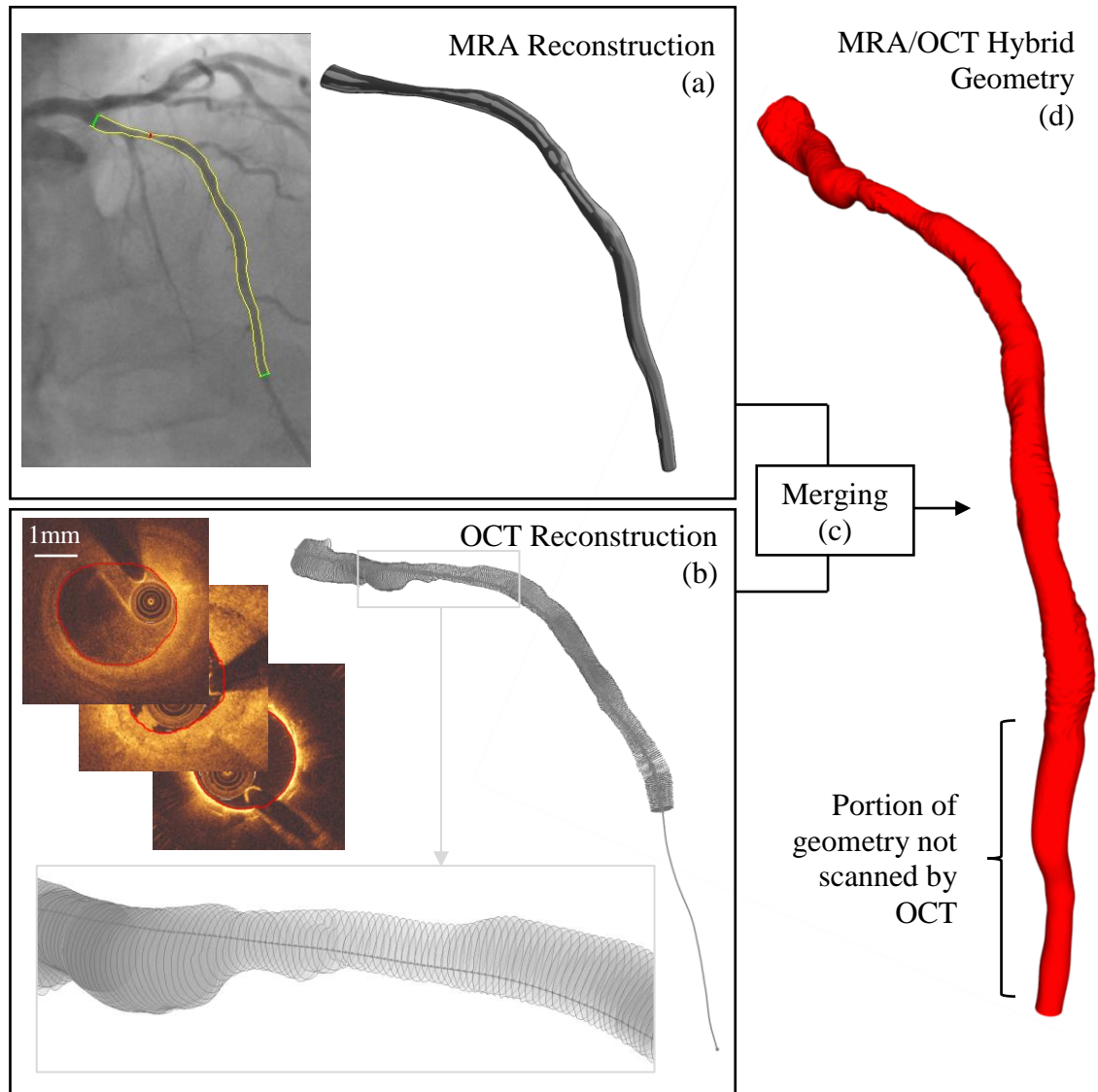
Figure 5.2 – MRA/OCT hybrid coronary artery reconstruction process. (a) 3D reconstruction from MRA data using QAngio XA 3D by Medis (Leiden, Netherlands) (b) OCT segments extracted from QCU-CMS by Medis (Leiden, Netherlands) are stacked along the artery centreline that is extracted from the MRA reconstruction. (c) The OCT segments are lofted together along with the MRA geometry. (d) An MRA/OCT hybrid coronary artery reconstruction, a smooth portion is observed in the distal portion of the artery as a result of the OCT procedure not covering this region.

Step 1. Prior to medical intervention, an MRA scan of the LAD artery was conducted of a 51 year old male diagnosed with a high burden of plaque with tight stenosis and a thrombus. The MRA scan was obtained at University Hospitals Bristol, UK. The medical imaging software QAngio XA 3D by Medis (Leiden, Netherlands) then exported a solid surface geometry into a VTP format.

Approximate completion time = Not applicable, data is already available.

Step 2. A catheter was inserted into the LAD and OCT segmentations of a portion of the LAD were obtained. The Cartesian co-ordinates of the OCT segments were then exported from QCU-CMS by Medis (Leiden, Netherlands) into a large array of data. It is worth noting at this point, that during the OCT imaging process, the imaging device does not record its reference in space whilst it is in movement, and the distance between each OCT segment is dependent on the automated motorised pullback speed of the imaging device. The OCT imaging process not recording its reference in space is one of the main challenges in reconstructing the OCT segments to follow the curvature of the vessel. As alluded to earlier, this has been attempted by Toutouzas et al. [155], however, the accuracy of the arterial surface seems to have been lost in the reconstruction process. *Approximate completion time = Not applicable, data already available.*

Step 3. Microsoft Excel is then combined with a Visual Basic Applications (VBA) script to separate the Cartesian co-ordinates of each OCT segment into separate TXT files.

Approximate completion time = 15 minutes.

Step 4. Vascular Modelling Toolkit (VMTK) is then used to extract the centreline Cartesian co-ordinates of the surface geometry created from MRA imaging. VMTK is also used to convert the solid surface model into a more effective file format (VTP to STL) in preparation for assembling the parts in the CAD package, SOLIDWORKS 2016.

Approximate completion time = 15 minutes.

Step 5. SOLIDWORKS 2016 is then used to assemble the OCT segments to the centreline of the MRA-created geometry. Each OCT segment is first converted into a planar surface with a centre point (used as a reference point in assembly mates to follow) using a VBA script and are individually saved as 'part' files. The Cartesian co-ordinates of the centreline are then imported into an assembly to create a centreline curve. A number of points (equal to the number of obtained OCT segments) are then assigned locations along the centreline. The distance (0.2 mm in this case) between the points is defined by the pullback speed of the OCT imaging process. Various reference planes and constructions points are used during this process which are currently the most time consuming of the whole reconstruction process. Each OCT segment part file is then imported into the assembly one-by-one and mated to its corresponding point on the centreline, a VBA script is again used to automate this otherwise highly time consuming process. The surface of

each segment is constrained to be perpendicular to the centreline at this point. Each segment is then rotated and orientated properly until it accurately represents the true coronary lumen. Neighbouring peripheral arteries observable in the original OCT segmentations are used as reference points for obtaining the correct angle of orientation. Once all segments are mated to the centreline, each OCT segment is then lofted together along with the residual MRA surface which was not covered during the OCT process, this creates a single solid surface which accurately represents the arterial wall. The final geometry is illustrated in Figure 5.3, the smooth and rough surfaces represent the MRA and OCT derived sections, respectively. As can be seen from Figure 5.2 and Figure 5.3, significant discrepancy is found between the smooth MRA portion of the model and the OCT/MRA hybrid portion in their ability to accurately represent the arterial lumen. Following the merging of the MRA and OCT data, flow extensions are affixed to the inlet (one diameter in length) and outlet (seven diameters in length) to allow for flow to fully develop [76], [78], [79], as shown in Figure 5.4. This is to ensure that shear stresses close to the inlet and outlet boundaries are not unusually high. A solid geometry file is then exported in an IGES format, which is now ready for the meshing process.

Approximate completion time = 3 hours 15 minutes.
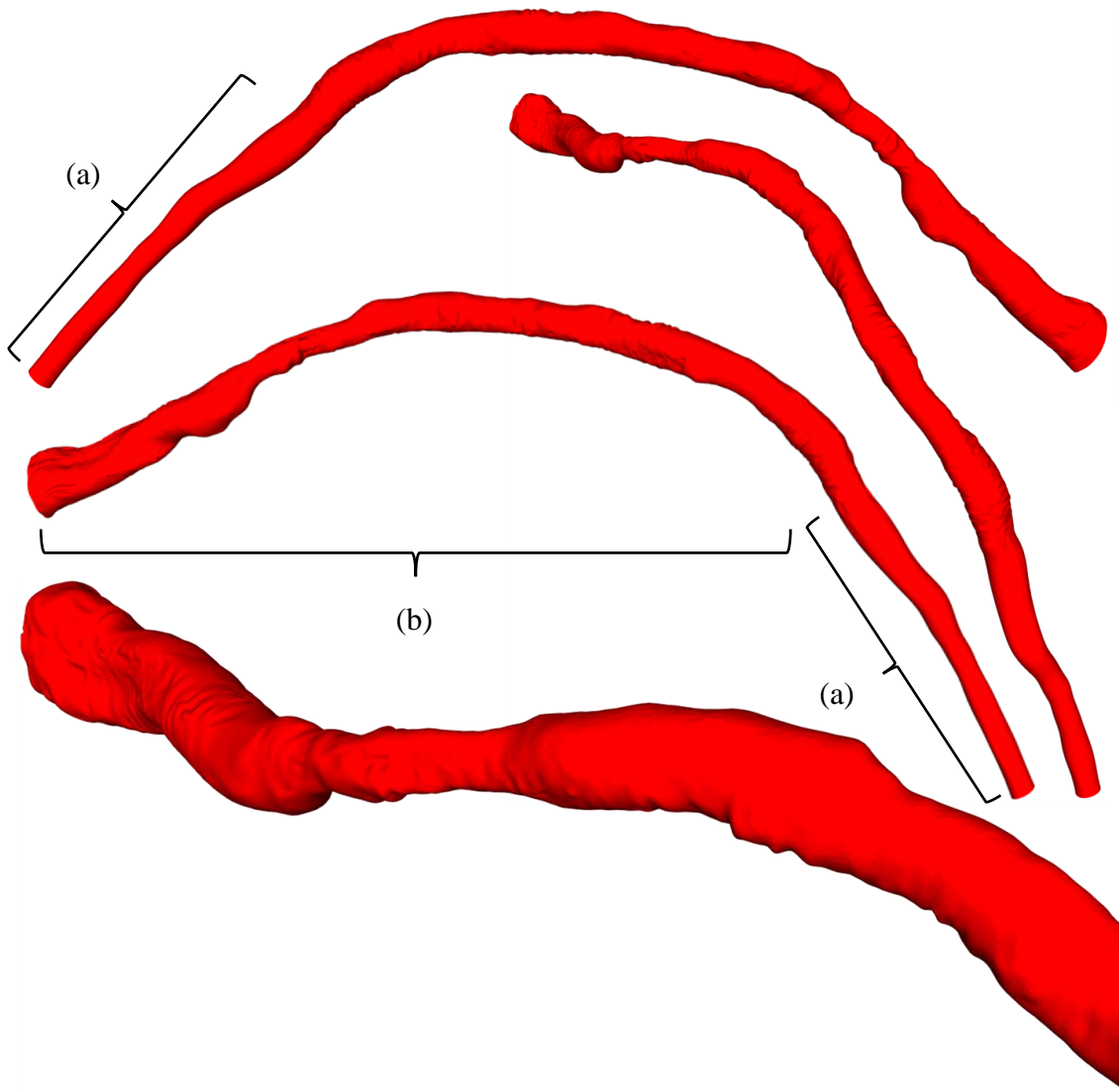
Figure 5.3 – Merged OCT segments with the MRA 3D model to create a realistic curved representation of the luminal surface. The smooth (a) and rough (b) surfaces represent the MRA and OCT derived sections respectively.
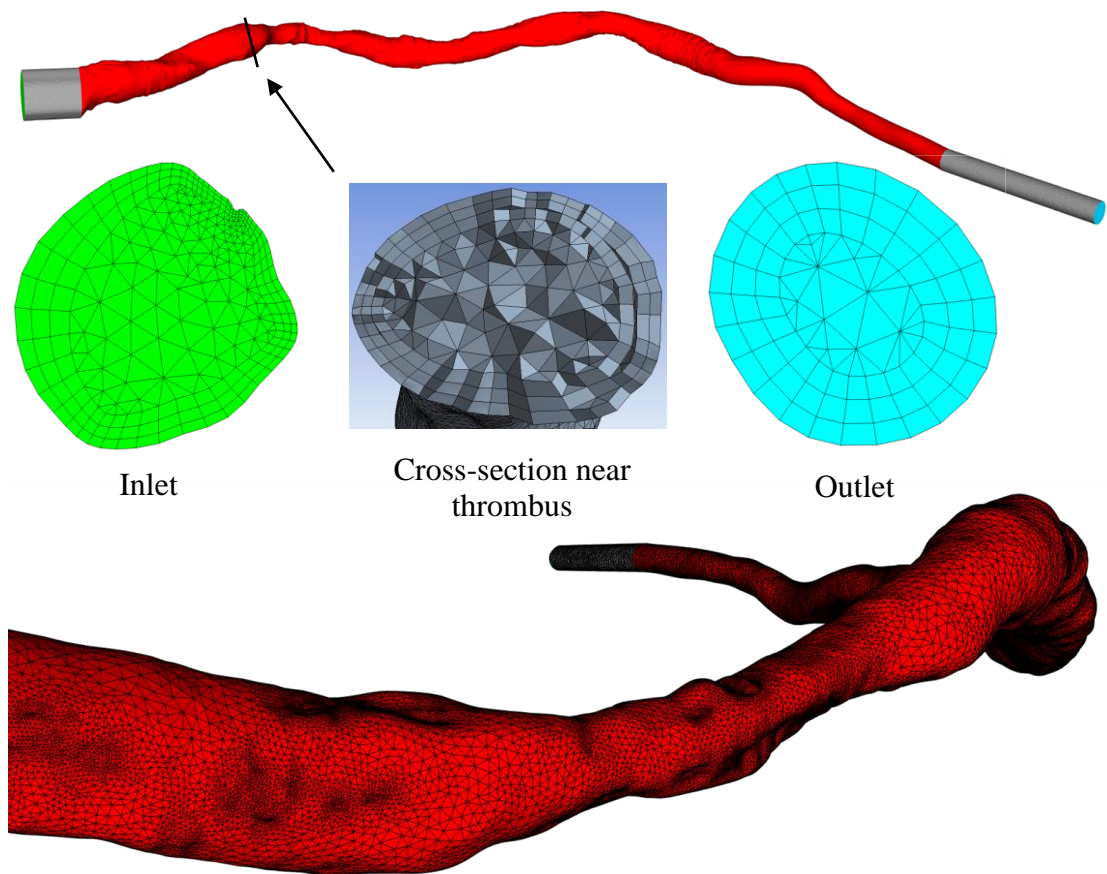
Figure 5.4 – The mesh was based on a finite volume hybrid mesh (≈1 million elements) consisting of tetrahedral elements within the core region and prism layers (3 elements thick) near the wall to allow for large spatial velocity gradients. Extension regions are added to the inlet (one diameter in length) and outlet (seven diameters in length) to allow for flow to properly develop [76], [78], [79].

Unlike methods by Timmins et al. [151] for IVUS image reconstruction, coronary branches were excluded in this study, similar to the work of Ha et al. [156]. Novel methods are still required to include them in the reconstruction of OCT images and are currently a work in progress by the author.

5.2.2 Computational Domain

The geometry was meshed using ANSYS-Meshing (Version 17.1). The mesh was based on a finite volume hybrid mesh consisting of tetrahedral elements within the core region and prism layers (3 elements thick) near the wall to allow for large spatial velocity gradients. In order to ensure the accuracy of the simulations, a series of seven steady-state computations with various mesh refinement levels (ranging from $4.5 \cdot 10^5$ to $1.4 \cdot 10^6$ elements) were conducted to ensure mesh convergence. A velocity of 0.1184 m·s^{-1} was

applied to the inlet (inlet area is $1.13 \cdot 10^{-5}$ m^2) based on the average velocity from the pulsatile waveform of the LAD artery of a patient at rest [157]. A traction free outlet BC was applied to the outlet. Velocity isosurfaces and WSS contours were analysed to investigate mesh convergence. Velocity isosurfaces and WSS contours reduced in discrepancy up until a mesh of ≈1 million elements. Further refinement resulted in insignificant changes to velocity and WSS. Therefore, the mesh of ≈1 million elements was considered adequate and used for the further simulations in this study, similar to the mesh density used by Timmins et al. for a similar study [79].

5.2.3 Numerical Procedure

The CFD solver ANSYS-CFX (Version 17.1) was used for the simulations. Blood was defined as a three-dimensional, incompressible and isothermal fluid. Dynamic viscosity and density of the blood are set to 0.004 Pa·s and 1060 kg·m^{-3}, respectively [120]. The simulation was run for 4 cardiac cycles (4 s) with a timestep size of 1.25 m·s and 10 coefficient loops per timestep, this proved adequate in order to allow the boundary flow rate and pressure waveforms to converge (≈8 hours solution time utilising 16 CPUs). The results are recorded during the final cardiac cycle. The commercial visualisation tool, Ensight 10.1.6 was used to post-process the results.

5.2.4 Boundary Conditions

Inlet. The transient inlet profile for the LAD artery was taken from Kim et al. [157] and applied at the inlet in this study, as shown in Figure 5.5. The profile by Kim et al. was obtained as a result of running a complex coronary artery system simulation with advanced boundary conditions. The simulation incorporated a lumped parameter model (for all coronary artery outlets), three-element Windkessel model (for all aortic peripheral arteries) and an inlet coupled to a lumped parameter heart model. The BCs used by Kim et al. [157] were adjusted to match both the flow distribution and measured brachial artery pulse pressure observed *in vivo* by Stergiopulos et al. [158].
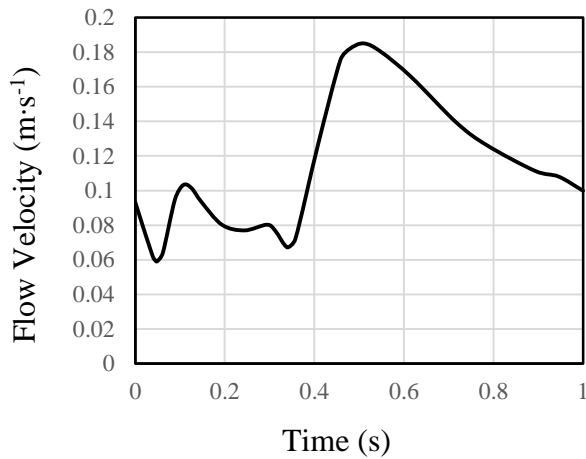
Figure 5.5 − The LAD inlet flow rate profile was taken from Kim et al. [157] and used for the transient simulation. The average velocity of this profile is 0.1184 m·s^{-1} which was used for the steady-state mesh independency tests. The inlet area of the geometry is 1.13·10^{-5} m^2.

Outlet. A zero pressure (traction free) condition is applied at the outlet, similar to recent work in the literature [79]. For a similar study, but with six outlets instead of one, a validation study against invasive intracoronary measurements was performed to check that the zero pressure condition reproduced similar flow to *in vivo* haemodynamics [79]. A zero pressure condition was also used for this study due to the simplicity of the geometry (only one outlet). Including complex outlet BCs would also be unnecessary in this study as this is a preliminary test and there are likely to be other sources of inaccuracy in the model (e.g. removal of the side branches). It is worth reiterating at this point that the focus of this part of the thesis is on the novelty of the geometrical reconstruction method and not on the complexity and physiological accuracy of the haemodynamics. The latter have been discussed in the previous chapters in length.

5.3   Results & Discussion

The TAV and shear stress-based haemodynamic parameters are discussed together in this section. As previously mentioned, the haemodynamics in this study are unlikely to be physiologically accurate due to the number of essential simplifications. However, this study provides an insight into a new advancement in reconstructing coronary arteries for simulation purposes. Finally, the limitations and future direction of this work will be outlined in this section.

It is first important to understand the location of the thrombus within the coronary artery. The thrombus was omitted from the geometrical reconstruction process in order to begin

developing correlations between haemodynamic metrics and likelihood of acute endothelial rupture and thrombus development. The thrombus location was situated in close proximity to the tight stenosis, as shown in Figure 5.6. The thrombus here would also be close to one of the bifurcations if it were included in the model. The right hand side of Figure 5.6 shows the OCT segmentations captured within the thrombus region. The white dashed curved line in these images represent the original vessel wall, which was modelled in this study. The yellow regions inside of the white dashed line represent a developed thrombus. Being able to view the exact shape and location of the thrombus like this is important for developing correlations between local haemodynamics and endothelial rupture and thrombus development.

OCT Segmentations

Thrombus location
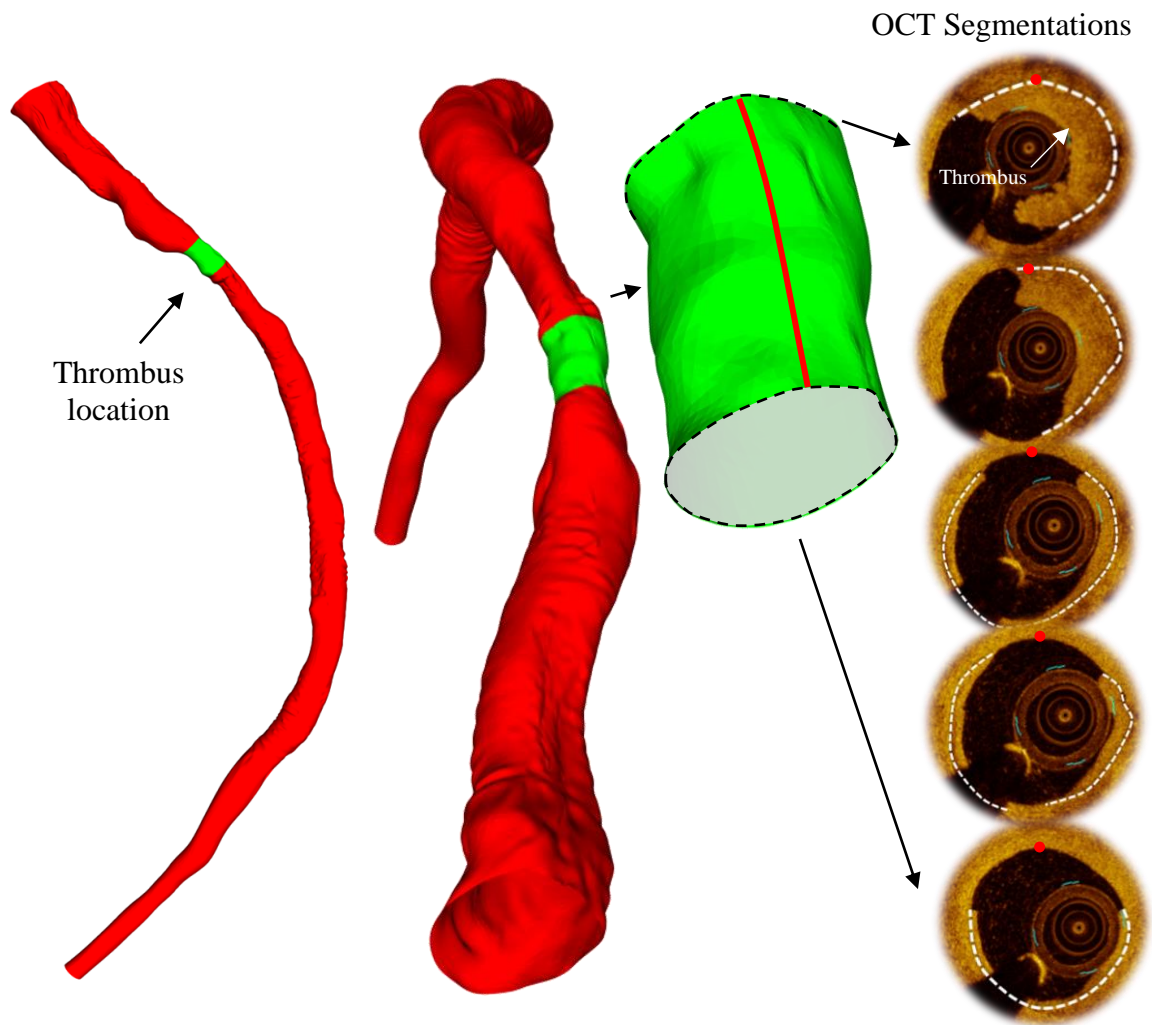
Thrombus

Figure 5.6 – Illustration of the location of the thrombus in this patient (highlighted in green). The accurate profile of the thrombus is observable in the OCT segmentations. The thrombus is situated inside the dashed white curve. Note that the thrombus is not modelled in the simulation. The red line and dots are used as a reference for the orientation of the OCT segments, the red dots are aligned with the red line.

Shear stress-based haemodynamic metrics evaluated over the geometry wall are illustrated in Figure 5.7, the geometry is shown from the front and back views. The location of the thrombus is highlighted by a grey rectangle. It can be seen that the region where the thrombus develops has a much higher WSS distribution compared to the rest of the wall. In Figure 5.6, a spatial mean average WSS evaluated over the region highlighted in green was 18 Pa, which is +150 % the average WSS evaluated over the whole geometry. The average OSI in the thrombus location was also approximately 30 % lower than the rest of the wall, which, in this specific case does not correlate well with the current theory that plaque progression relates to regions of low and oscillatory shear

stress [78], [79]. However, the high WSS is most likely responsible for the presentation of a thrombus. RRT was also recorded to be approximately 66 % less around the thrombus location than the rest of the vessel wall.
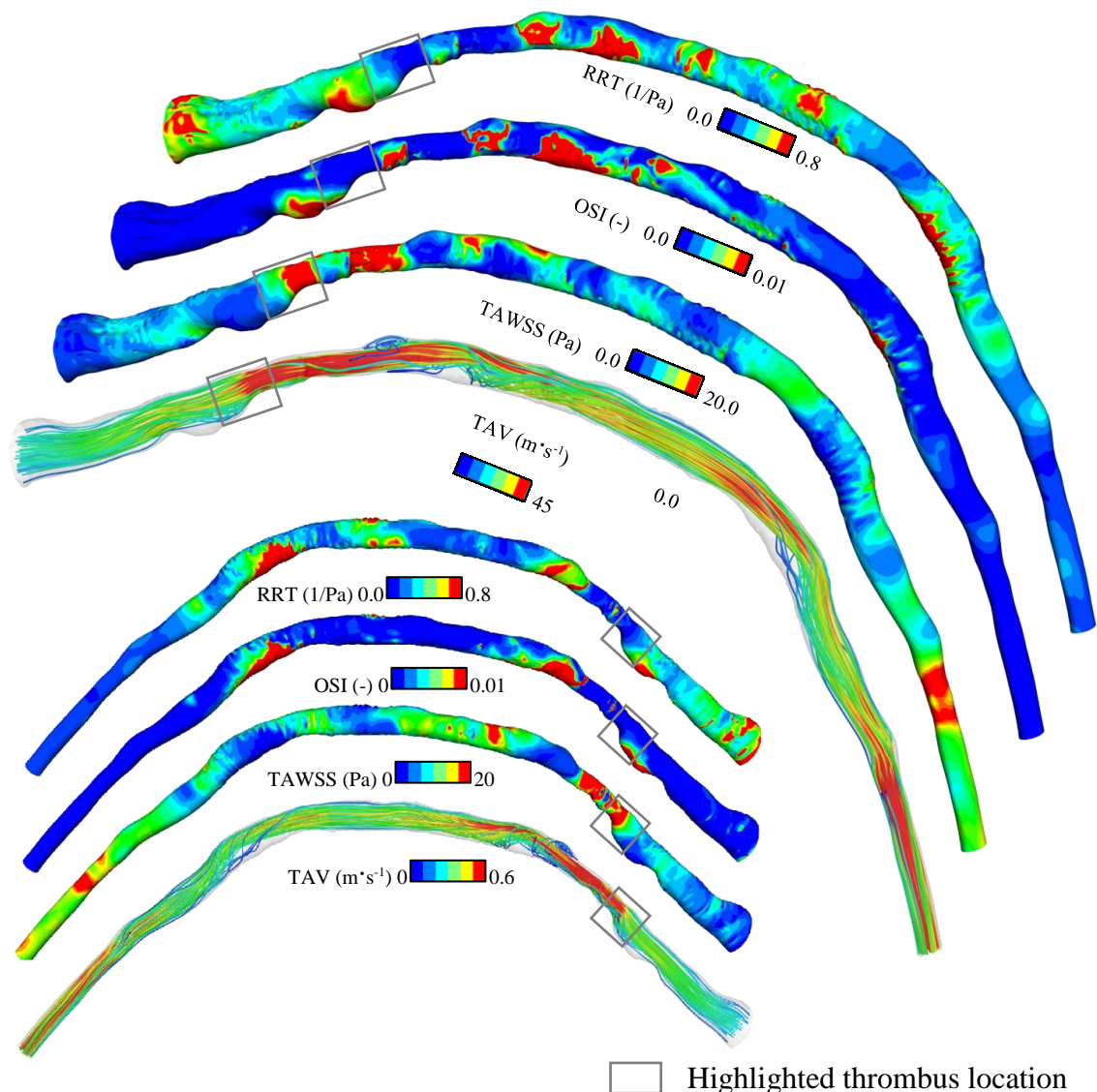
Figure 5.7 – Illustration of the haemodynamic metrics and streamlines recorded from the simulation. The highlighted region (grey box) represents the general location of the thrombus.

By comparing OSI and WSS distributions around the thrombus location in Figure 5.7 with the specific location of the thrombus being known, more specific correlations between these two metrics and the development of a thrombus can be created. The thrombus appears to have developed amongst regions of high WSS, whilst also in a region of significantly low OSI. The location of the thrombus is not unusual as it is located at

the start of the tight stenosis, thus experiencing high flow velocity (refer to Figure 5.7 and Figure 5.8) with resulting high WSS, hence, altering the endothelial wall [159]–[161].

TAV (m·s⁻¹) 0 ▮▮▮▮ 0.6
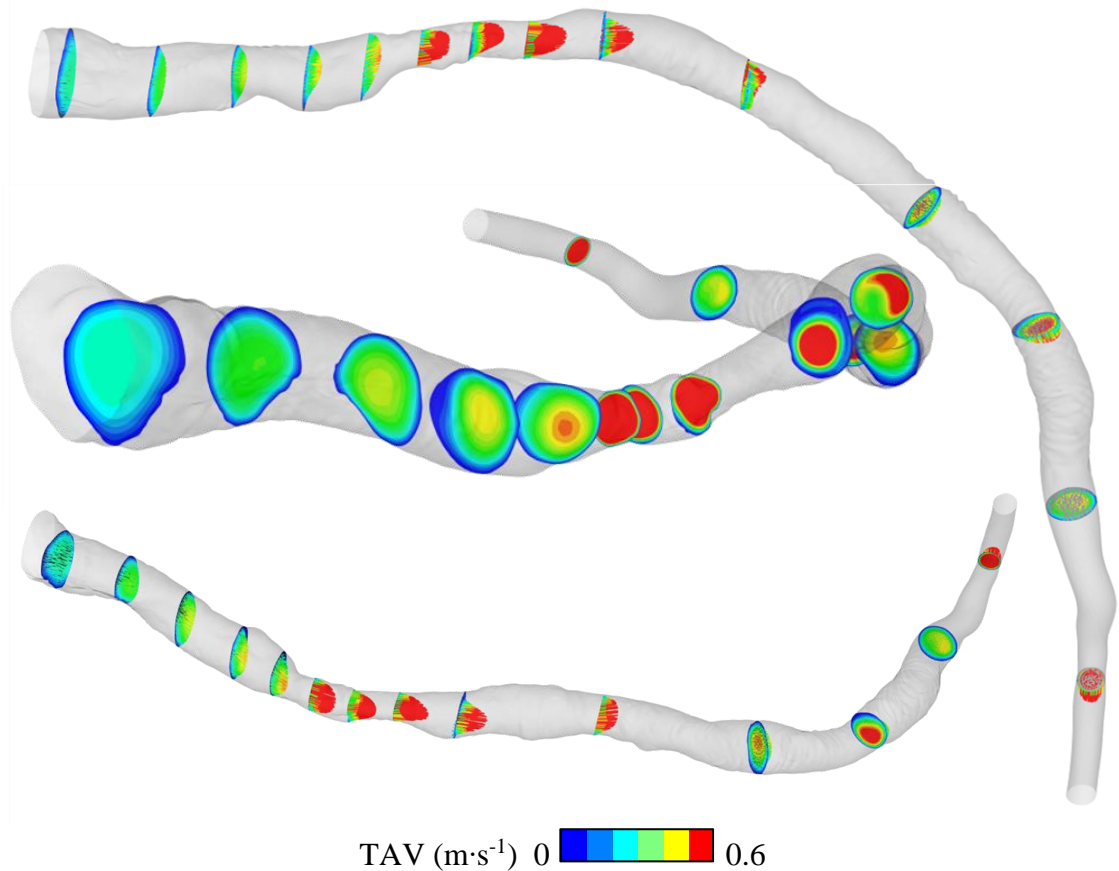
Figure 5.8 – Cross-sectional planes coloured by TAV.

There are a number of important limitations in this current work, which will later be described. Yet, it is a step forward in developing an average trend between local haemodynamics and coronary artery disease risk. The accuracy of the geometrical model created in this work is a significant improvement on previous work [76], [79], [150]–[153], [162]. This new method is able to capture small details in the model as well as accounting for the curvature of the vessel. It also represents significant progress in making the reconstruction process more autonomous, which up until now, has mostly been a manual and time-consuming process [162]. Further developing this methodology will ultimately enable clinicians to be able to identify, at an early stage, regions most at risk of vessel wall modification. This is considered as a step forward towards personalised and patient-specific medical treatment, which currently represents a topic of great interest in this research community [79], [163]–[165]. Therefore, this work serves as the foundation on which a more automated and rigorous study can be developed.

5.4 Limitations & Future Work

Some of the OCT segments were omitted from the reconstruction process so that unphysiological lumps would not be present in the final geometry, and hence unphysiological representations of WSS-based haemodynamic metrics. This was because some OCT segments were partially capturing the peripheral branches and were creating sudden protrusions in the geometry. Smoothing of the OCT segments by fitting a spline between the Cartesian coordinates with a defined tolerance was able to reduce the unusual lumps that were running longitudinally along the geometry. The unusual wave pattern in some locations of the geometry however were more difficult to smoothen out. An automatic smoothing feature to clear up these imperfections in the geometry would be valuable for representing the arterial lumen more accurately.

The reconstruction process presented in this chapter was semi-automated, requiring user input at various stages of the process. In order to make the reconstruction technique useful for processing a large cohort of data, the process should be designed such that it requires as little user input as possible.

Further reconstruction time reductions can be obtained by optimising the efficiency of performing Step 5 described in Section 5.2.1. This can be done conducting this step on a machine optimised for such a process in terms of hardware, as well as improving the efficiency of the code which automates the process.

Unlike methods by Timmins et al. [151] for IVUS image reconstruction, coronary branches were excluded in this study. Hence, a zero pressure outlet BC was used for this study due to the simplicity of the geometry. Further development of an automated process that is able to account for the peripheral branches and incorporate more physiologically accurate BCs is crucial for studying the local haemodynamics effectively. Future studies may also benefit from incorporating the whole coronary artery tree in order to impose more advanced and well accepted lumped parameter outlet BC models [52], [157], [166].

A patient-specific velocity inlet profile was unavailable for this study, hence a more generic profile was incorporated into the simulations. Future studies should incorporate patient-specific flow profiles in order to produce more realistic flow conditions.

A timestep independency study was not carried out for this specific study, however, the timestep size was deemed adequate as it is smaller than those used by similar work found in the literature [79], [151].

It is currently challenging to incorporate biochemical models into CFD simulations [167], therefore, the biochemical factors that are involved with CVDs have been ignored in this work.

Now that it is proven possible to represent the coronary artery with such accuracy, work is in progress to address the limitations described above and to apply the process to a larger cohort of data.

5.5   Summary

Correlating local haemodynamics with risk of coronary artery diseases has been a challenge to date. In the present study, a novel reconstruction method was developed which combines OCT segmentations of the coronary artery lumen with the centreline obtained from MRA imaging. The main contribution of this method was its ability to eliminate the manual and time consuming process of stacking the OCT segments on the MRA derived centreline. The method developed in this work is able to reduce the reconstruction time from approximately 4 days to approximately 4 hours. Despite the number of limitations to the work, the developed methodology is already a significant step from what is currently available. Future work will account for the multiple outlets a coronary vessel may have, be more automated, and incorporate more physiologically accurate BCs.

CHAPTER 6

CONCLUSIONS, LIMITATIONS & FUTURE WORK

Each chapter will now be concluded separately. Each aim of the thesis will then be addressed in terms of limitations and potential for future work.

6.1 Conclusions

6.1.1 Chapter 2

It is widely recognised that in CFD simulations, prescribing different BCs at boundaries can significantly affect the solutions of the equations governing blood flow, and hence the metrics related to CVDs [43], [49], [100]. In this chapter, using advanced CFD codes and through comparison with *in vivo* data, the impact of various inlet and outlet BCs on predicting the localisation of CVDs were assessed for an accurately-represented rabbit aorta configuration. This work enables both specialist and non-specialist CFD practitioners to gain a better understanding of the commonly-used BCs and their effects and limitations on a subject-specific complex cardiovascular model. The results and discussions also provided an insight into how significant the effects of these outlet BCs are on typical WSS-based hemodynamic metrics.

One of the main findings to emerge from the present study was that prescribing a transient simulation and a fully-developed flow at the inlet are not required when the focus is only on the flow within the aorta and around the intercostal branches. Therefore, simulations can be simplified significantly in studies concerning the lesions within the aorta including abdominal aortic aneurysm, aortic atherosclerosis and type B aortic dissection. Another important finding from this research was that assuming the widely-accepted low WSS theory of Caro et al. [18], it was found that the ML-based outlet BC returns the most physiologically accurate results, when compared against *in vivo* data.

6.1.2 Chapter 3

The impact of various commonly used outlet BCs on predicting the localisation of CVDs were assessed for an accurately-represented human female aorta configuration. As a continuation from Chapter 2, this work further enables CFD practitioners to gain a better understanding of the commonly-used outlet BCs and their effects and limitations on a

subject-specific cardiovascular model. Three outlet BCs were investigated, traction free, ML and the three-element Windkessel model. The results were compared against the Windkessel model as it is now widely accepted as being accurate in capturing the downstream conditions of the cardiovascular system [104]. The results suggest that, i) only when investigating TAWSS, the traction free BC will produce similar distributions to the more advanced three-element Windkessel BC, ii) with the exception of TAWSS, the shear stress based haemodynamics metric distributions varied significantly from test to test, suggesting that the traction free and ML BCs should be avoided whenever possible, iii) OSI was the most affected by the prescribed outlet BC, with the three-element Windkessel producing negligible OSI within the subclavian and carotid arteries compared to the other BCs, and significantly more pronounced axial streaks within the TAo, iv) the three-element Windkessel is better able to capture stagnant and recirculating flow than the other two BCs due to the freedom it allows the flow at the outlets.

6.1.3 Chapter 4

A patient-specific aorta model with normal aortic function was used to study the importance of incorporating the severity of HF in the computational preoperative planning of an LVAD configuration. The results were compared against a control model which did not include an LVAD graft and used patient-specific BCs, this model represented healthy aortic haemodynamics.

The results show that in terms of overall perfusion, the smaller vessels (RSA, RCCA, LCCA, LSA) responded in an irregular manner as LVAD/AR-FR increased, with a general deficiency of perfusion by approximately 31 %. Whilst the larger vessel's (aortic arch and TAo) perfusion response was generally more linear and predictable, with a general increase of 76 %. Moreover, similar patterns are experienced when comparing OSI, RRT and TAWSS. The fundamental reasons for these discrepancies in behaviour is mainly due to, i) the jet from the cannula blocking flow to the aortic arch branches (RSA, RCCA, LCCA and LSA), ii) the aortic arch branches better auto-regulating flow rate due to their smaller diameter, iii) the entrances of the aortic branches experiencing highly disturbed flow due to their close proximity to the anastomosis.

The general irregular behaviour of the subclavian and carotid arteries to LVAD/AR-FR indicates that the perfusion and WSS-based haemodynamic metrics within these arteries cannot be accurately predicted unless the LVAD/AR-FR is incorporated into the computational preoperative planning of the optimal LVAD configuration. The

consistently excessive perfusion to the TAo suggests that regardless of LVAD/AR-FR, the TAo will most likely experience adequate perfusion. Incorporating LVAD/AR-FR whenever possible into the preoperative planning process, will aid in more accurately improving the effects on the circulatory system post LVAD implantation.

6.1.4   Chapter 5

Correlating local haemodynamics with risk of coronary artery diseases has been a challenge to date. This is due to the difficulties associated with accurately reconstructing 3D geometries which are to be used in CFD investigations. In the present study, a novel reconstruction method was developed which combines OCT segmentations of the coronary artery lumen with the centreline obtained from MRA imaging. Accounting for the curvature of the vessel as well as incorporating the high resolution of OCT imaging to reconstruct a 3D geometry has not been achieved until now, and holds significant value to understanding coronary pathology. Despite the number of limitations to the work presented, the developed methodology is regardless a significant improvement from what is currently available. Future work will account for the multiple outlets a coronary vessel may have, be more automated, and incorporate more physiologically accurate BCs. This will allow for the automatic processing of a large cohort of data in order to begin developing a strong correlation between local coronary haemodynamics and the risk of endothelial rupture and thrombus development

The reconstruction methods developed in this project can also be advanced to other applications where more accurate representations of the cardiovascular system is needed. The use of OCT imaging in cardiovascular applications is still relatively new and has had limited applicability until now. This work shows potential in advancing the accuracy of reconstructing a wider spread of cardiovascular geometries in future research.

6.2   Limitations & Future Work

General limitations of the thesis:

- The biological factors that are associated with coronary artery diseases were omitted from this thesis as they are not within the scope of this work. Simulating the interaction between biochemical reactions and haemodynamics is currently too complex to incorporate into simulations, and is most often ignored in cardiovascular CFD simulations. Also, in accordance with similar work, non-

Newtonian blood properties have been neglected throughout the thesis [53], [54], [86], [140].

- Fluid-structure interaction in this area of research is concerned with the added pumping effect created by blood vessels in the cardiac cycle. Fluid-structure interaction requires significant amounts of computational power and solution time, and as a result has been ignored throughout the thesis.

Specific limitations and future work related to the objectives of the thesis will now be given.

Objectives 1 to 3 were generally to analyse the impact various types of computational BCs can have on computational haemodynamic investigations of CVDs. The limitations and future work associated with the work conducted to complete these objectives include:

- Various outlet BC models which are accepted as more physiologically accurate have been ignored during this study. Namely the structured tree model [47], complex Windkessel model [117] and multiscale models [118]. Despite these models being able to further reduce modelling error, they are often complex to incorporate into simulations and have therefore been omitted from this study.

- The future direction of this work involves comparing commonly used outlet BCs against these more advanced outlet BC models. As well as extending the investigation to a diverse range of human aorta configurations in order to improve the relevance of this work.

- Due to LVAD and aorta configurations in reality changing vastly from patient to patient, the results of this work only act as an indicator of the importance of incorporating the patient-specific LVAD/AR-FR into the patient-specific preoperative planning of the optimum cannula angle, design and location. Doing so will improve the effects on the circulatory system post LVAD implantation.

- Further studies are required in order to test the value of the LVAD/AR-FR on a wider range of LVAD configurations. Due to the sparsity of relevant data required to conduct a rigorous quantitative study of multiple patient-specific configurations [45], a more qualitative approach has been taken to assess the significance of the LVAD/AR-FR.

Objective 4 was to develop a novel geometrical reconstruction method for the accurate 3D representation of coronary arteries, which are to be used for associating

haemodynamic metrics with coronary artery diseases. The limitations and future work associated with the work conducted to complete this objectives include:

- During the reconstruction process of the coronary artery, a number of non-optimal methods were incorporated. A number of OCT slices were omitted in order to avoid unwanted protrusions from the geometry. Unphysiological lumps were also created that ran longitudinally along the geometry which were not fixed.

- The reconstruction process was semi-automated, requiring user input at various stages of the process. In order to make the reconstruction technique useful for processing a large cohort of data, the process should be designed such that it requires as little user input as possible.

- Contrary to methods by Timmins et al. [151] for IVUS image reconstruction, coronary branches were excluded in this study. Hence, a zero pressure outlet BC was used for this study due to the simplicity of the geometry. Further development of an automated process that is able to account for the peripheral branches and incorporate more physiologically accurate BCs is crucial for effectively studying the local haemodynamics. Future studies may also benefit from incorporating the whole coronary artery tree in order to impose more advanced and well accepted lumped parameter outlet BC models [52], [157], [166].

- A patient-specific velocity inlet profile was unavailable for this study, hence a replacement, more generic profile was incorporated into the simulations. Future studies should incorporate patient-specific flow profiles in order to produce more realistic flow conditions.

- A timestep independency study was not undergone for this specific study, however, the timestep size was deemed adequate as it is smaller than those used by similar work found in the literature [79], [151].

REFERENCES

[1] M. Nichols, N. Townsend, P. Scarborough, and M. Rayner, *European cardiovascular disease statistics*, 2012th ed. Brussels, European Society of Cardiology: European Heart Netwrok AISBL, 2012.

[2] X. Li, P. Fang, Y. Li, Y.-M. Kuo, A. J. Andrews, G. Nanayakkara, C. Johnson, H. Fu, H. Shan, F. Du, N. E. Hoffman, D. Yu, S. Eguchi, M. Madesh, W. J. Koch, J. Sun, X. Jiang, H. Wang, and X. Yang, "Mitochondrial reactive oxygen species mediate lysophosphatidylcholine-induced endothelial cell activation," *Arterioscler. Thromb. Vasc. Biol.*, vol. 36, no. 6, pp. 1090–1100, 2016.

[3] G. Peach, M. Griffin, J. K.G., M. M. Thompson, and R. J. Hinchliffe, "Diagnosis and management of peripheral arterial disease," *BMJ*, vol. 345, p. e5208, 2012.

[4] E. Braunwald, "Heart Failure," *JACC. Heart Fail.*, vol. 1, no. 1, pp. 1–20, Feb. 2013.

[5] N. Townsend, K. Wickramasinghe, P. Bhatnagar, K. Smolina, M. Nichols, J. Leal, R. Luengo-Fernandez, and M. Rayner, "Coronary heart disease statistics 2012 edition," *London Br. Hear. Found.*, vol. 19, 2012.

[6] K. H. Fraser, T. Zhang, M. E. Taskin, B. P. Griffith, and Z. J. Wu, "A quantitative comparison of mechanical blood damage parameters in rotary ventricular assist devices: Shear stress, exposure time and hemolysis index.," *J. Biomech. Eng.*, vol. 134, no. 8, p. 081002/11, Aug. 2012.

[7] K. H. Fraser, M. E. Taskin, B. P. Griffith, and Z. J. Wu, "The use of computational fluid dynamics in the development of ventricular assist devices," *Med. Eng. Phys.*, vol. 33, no. 3, pp. 263–280, Apr. 2011.

[8] A. D. Lucas and D. R. Greaves, "Atherosclerosis: Role of chemokines and macrophages," *Expert Rev. Mol. Med.*, vol. 3, no. 25, pp. 1–18, Nov. 2001.

[9] H. Ha, D. Hwang, W. R. Choi, J. Baek, and S. J. Lee, "Fluid-dynamic optimal design of helical vascular graft for stenotic disturbed flow," *PLoS One*, vol. 9, no. 10, p. e111047, 2014.

[10] D. N. Ku, "Blood flow in arteries," *Annu. Rev. Fluid Mech.*, vol. 29, no. 1, pp.

399–434, Jan. 1997.

[11] E. Braunwald, D. P. Zipes, and P. Libby, "The vascular biology of atherosclerosis," in *Heart Disease: A Textbook of Cardiovascular Medicine*, 6th Editio., E. Braunwald, Ed. Philadelphia: W.B. Saunders Company, 2001, pp. 1–1086.

[12] A. M. Malek, S. L. Alper, and S. Izumo, "Hemodynamic shear stress and its role in atherosclerosis," *Jama*, vol. 282, no. 21, pp. 2035–2042, 1999.

[13] F. J. Rybicki, S. Melchionna, D. Mitsouras, A. U. Coskun, A. G. Whitmore, M. Steigner, L. Nallamshetty, F. G. Welt, M. Bernaschi, M. Borkin, J. Sircar, E. Kaxiras, S. Succi, P. H. Stone, and C. L. Feldman, "Prediction of coronary artery plaque progression and potential rupture from 320-detector row prospectively ECG-gated single heart beat CT angiography: Lattice Boltzmann evaluation of endothelial shear stress," *Int. J. Cardiovasc. Imaging*, vol. 25, no. 2, pp. 289–299, Jan. 2009.

[14] S. J. White, A. C. Newby, and T. W. Johnson, "Endothelial erosion of plaques as a substrate for coronary thrombosis," *Thromb. Haemost.*, vol. 115, no. 3, pp. 1–11, 2016.

[15] Y. S. Chatzizisis, M. Jonas, A. U. Coskun, R. Beigel, B. V Stone, C. Maynard, R. G. Gerrity, W. Daley, C. Rogers, E. R. Edelman, C. L. Feldman, and P. H. Stone, "Prediction of the localization of high-risk coronary atherosclerotic plaques on the basis of low endothelial shear stress: An intravascular ultrasound and histopathology natural history study.," *Circulation*, vol. 117, no. 8, pp. 993–1002, Feb. 2008.

[16] E. Wellnhofer, J. Osman, U. Kertzscher, K. Affeld, E. Fleck, and L. Goubergrits, "Flow simulation studies in coronary arteries--impact of side-branches," *Atherosclerosis*, vol. 213, no. 2, pp. 475–81, Dec. 2010.

[17] S. Chien, "Mechanotransduction and endothelial cell homeostasis: The wisdom of the cell," *Am. J. Physiol. Heart Circ. Physiol.*, vol. 292, no. 3, pp. H1209–H1224, Mar. 2007.

[18] C. G. Caro, N. J. Cheshire, and N. Watkins, "Preliminary comparative study of small amplitude helical and conventional ePTFE arteriovenous shunts in pigs," *J. R. Soc. Interface*, vol. 2, no. 3, pp. 261–266, Jun. 2005.

[19]   V. Peiffer, S. J. Sherwin, and P. D. Weinberg, "Does low and oscillatory wall shear stress correlate spatially with early atherosclerosis? A systematic review," *Cardiovasc. Res.*, vol. 99, no. 2, pp. 242–250, 2013.

[20]   W. Koenig and N. Khuseyinova, "Biomarkers of atherosclerotic plaque instability and rupture," *Arterioscler. Thromb. Vasc. Biol.*, vol. 27, no. 1, pp. 15–26, 2007.

[21]   B. Furie and B. C. Furie, "Mechanisms of thrombus formation," *N. Engl. J. Med.*, vol. 359, no. 9, pp. 938–949, 2008.

[22]   C. Schmid, H. Welp, S. Klotz, H. a Baba, M. J. Wilhelm, and H. H. Scheld, "Outcome of patients surviving to heart transplantation after being mechanically bridged for more than 100 days," *J. Hear. Lung Transplant.*, vol. 22, no. 9, pp. 1054–1058, Sep. 2003.

[23]   M. J. Wilhelm, D. Hammel, C. Schmid, A. Rhode, T. Kaan, M. Rothenburger, J. Stypmann, M. Schäfers, C. Schmidt, H. a Baba, and H. H. Scheld, "Long-term support of 9 patients with the DeBakey VAD for more than 200 days," *J. Thorac. Cardiovasc. Surg.*, vol. 130, no. 4, pp. 1122–1129, Oct. 2005.

[24]   C. Schmid, M. Jurmann, D. Birnbaum, T. Colombo, V. Falk, G. Feltrin, A. Garatti, M. Genoni, G. Gerosa, P. Göttel, J. Gummert, R. Halfmann, D. Hammel, E. Hennig, F. Kaufmann, M. Lanfranconi, B. Meyns, F. Mohr, J. Müller, D. Nikolov, K. Rucinskas, H.-H. Scheld, F.-X. Schmid, M. Schneider, V. Sirvydis, R. Tandler, E. Vitali, D. Vlasselaers, M. Weyand, M. Wilhelm, and R. Hetzer, "Influence of inflow cannula length in axial-flow pumps on neurologic adverse event rate: Results from a multi-center analysis," *Journal of Heart and Lung Transplantation*, vol. 27, no. 3. pp. 253–260, 2008.

[25]   C. Schmid, T. D. T. Tjan, C. Etz, C. Schmidt, F. Wenzelburger, M. Wilhelm, M. Rothenburger, G. Drees, and H. H. Scheld, "First clinical experience with the Incor left ventricular assist device," *J. Hear. Lung Transplant.*, vol. 24, no. 9, pp. 1188–94, Sep. 2005.

[26]   P. Hochareon, K. B. Manning, A. A. Fontaine, J. M. Tarbell, and S. Deutsch, "Correlation of in vivo clot deposition with the flow characteristics in the 50 cc penn state artificial heart: A preliminary Study," *ASAIO J.*, vol. 50, no. 6, pp. 537–542, 2004.

[27]   K. H. Fraser, T. Zhang, M. Taskin, Ertan, B. Friffith, P, and J. Z. Wu,

"Computational fluid dynamics analysis of thrombosis potential in left ventricular assist device drainage cannulae," *ASAIO J.*, vol. 56, no. 3, pp. 157–163, 2010.

[28] BioNinja, "Causes and Consequences of Coronary Thrombosis," 2017. [Online]. Available: http://ib.bioninja.com.au/options/option-d-human-physiology/d4-the-heart/heart-disorders.html. [Accessed: 20-Jul-2007].

[29] J. A. Moore, B. K. Rutt, S. J. Karlik, K. Yin, and C. R. Ethier, "Computational blood flow modeling based on in vivo measurements," *Ann. Biomed. Eng.*, vol. 27, no. 5, pp. 627–640, 1999.

[30] C. A. Taylor, M. T. Draney, J. P. Ku, D. Parker, B. N. Steele, K. Wang, and C. K. Zarins, "Predictive medicine: Computational techniques in therapeutic decision-making," *Comput. Aided Surg.*, vol. 4, no. 5, pp. 231–247, 1999.

[31] C. A. Taylor, T. J. R. Hughes, and C. K. Zarins, "Finite element modeling of blood flow in arteries," *Comput. Methods Appl. Mech. Eng.*, vol. 158, no. 1–2, pp. 155–196, 1998.

[32] Q. Long, X. Y. Xu, B. Ariff, S. A. Thom, A. D. Hughes, and A. V. Stanton, "Reconstruction of blood flow patterns in a human carotid bifurcation: a combined CFD and MRI study," *J. Magn. Reson. Imaging*, vol. 11, no. 3, pp. 299–311, Mar. 2000.

[33] D. A. Steinman, "Image-based computational fluid dynamics modeling in realistic arterial geometries," *Ann. Biomed. Eng.*, vol. 30, no. 4, pp. 483–497, 2002.

[34] F. J. H. Gijsen, J. J. Wentzel, A. Thury, B. Lamers, J. C. H. Schuurbiers, P. W. Serruys, and A. F. van der Steen, "A new imaging technique to study 3-D plaque and shear stress distribution in human coronary artery bifurcations in vivo.," *J. Biomech.*, vol. 40, no. 11, pp. 2349–2357, Jan. 2007.

[35] B. T. Tang, C. P. Cheng, M. T. Draney, N. M. Wilson, P. S. Tsao, R. J. Herfkens, and C. a Taylor, "Abdominal aortic hemodynamics in young healthy adults at rest and during lower limb exercise: quantification using image-based computer modeling.," *Am. J. Physiol. Heart Circ. Physiol.*, vol. 291, no. 2, pp. H668–H676, 2006.

[36] M. Alimohammadi, O. Agu, S. Balabani, and V. Díaz-Zuccarini, "Development of a patient-specific simulation tool to analyse aortic dissections: Assessment of

mixed patient-specific flow and pressure boundary conditions," *Med. Eng. Phys.*, vol. 36, no. 3, pp. 275–284, 2014.

[37]   M. Alimohammadi, J. M. Sherwood, M. Karimpour, O. Agu, S. Balabani, and V. Díaz-Zuccarini, "Aortic dissection simulation models for clinical support: fluid-structure interaction vs. rigid wall models," *Biomed. Eng. Online*, vol. 14, no. 1, pp. 1–16, 2015.

[38]   Z. Cheng, C. Juli, N. B. Wood, R. G. J. Gibbs, and X. Y. Xu, "Predicting flow in aortic dissection: Comparison of computational model with PC-MRI velocity measurements," *Med. Eng. Phys.*, vol. 36, no. 9, pp. 1176–1184, 2014.

[39]   J. R. Cebral, M. A. Castro, J. E. Burgess, R. S. Pergolizzi, M. J. Sheridan, and C. M. Putman, "Characterization of cerebral aneurysms for assessing risk of rupture by using patient-specific computational hemodynamics models," *Am. J. Neuroradiol.*, vol. 26, no. 10, pp. 2550–2559, 2005.

[40]   L. Der Jou, G. Wong, B. Dispensa, M. T. Lawton, R. T. Higashida, W. L. Young, and D. Saloner, "Correlation between lumenal geometry changes and hemodynamics in fusiform intracranial aneurysms," *Am. J. Neuroradiol.*, vol. 26, no. 9, pp. 2357–2363, 2005.

[41]   M. Shojima, M. Oshima, K. Takagi, R. Torii, M. Hayakawa, K. Katada, A. Morita, and T. Kirino, "Magnitude and role of wall shear stress on cerebral aneurysm: Computational fluid dynamic study of 20 middle cerebral artery aneurysms," *Stroke*, vol. 35, no. 11, pp. 2500–2505, 2004.

[42]   D. A. Vorp, "Biomechanics of abdominal aortic aneurysms," *J. Biomech.*, vol. 40, no. 9, pp. 1887–1902, 2009.

[43]   C. A. Taylor and C. A. Figueroa, "Patient-specific modeling of cardiovascular mechanics.," *Annu. Rev. Biomed. Eng.*, vol. 11, no. 1, pp. 109–134, Jan. 2009.

[44]   H. Do, A. A. Owida, W. Yang, and Y. S. Morsi, "Numerical simulation of the haemodynamics in end-to-side anastomoses," *Int. J. Numer. Methods Fluids*, vol. 67, no. 5, pp. 638–650, 2011.

[45]   P. D. Morris, A. Narracott, H. von Tengg-Kobligk, D. A. Silva Soto, S. Hsiao, A. Lungu, P. Evans, N. W. Bressloff, P. V Lawford, D. R. Hose, and J. P. Gunn, "Computational fluid dynamics modelling in cardiovascular medicine," *Heart*, vol.

102, no. 1, pp. 1–11, 2015.

[46]   M. K. Mokhtar, F. Mohamed, M. N. Zamri, M. S. Sunar, and S. J. H. Chand, "A review on fluid simulation method for blood flow representation," in *Medical Imaging Technology: Reviews and Computational Applications*, Springer Singapore, 2015, pp. 129–141.

[47]   M. S. Olufsen, C. S. Peskin, W. Y. Kim, E. M. Pedersen, A. Nadim, and J. Larsen, "Numerical simulation and experimental validation of blood flow in arteries with structured-tree outflow conditions," *Ann. Biomed. Eng.*, vol. 28, no. 11, pp. 1281–1299, 2000.

[48]   I. E. Vignon-Clementel, C. A. Figueroa, K. E. Jansen, and C. A. Taylor, "Outflow boundary conditions for 3D simulations of non-periodic blood flow and pressure fields in deformable arteries.," *Comput. Methods Biomech. Biomed. Engin.*, vol. 13, no. 5, pp. 625–640, 2010.

[49]   A. D. Caballero and S. Laín, "A review on computational fluid dynamics modelling in human thoracic aorta," *Cardiovasc. Eng. Technol.*, vol. 4, no. 2, pp. 103–130, 2013.

[50]   J. Y. Moon, D. C. Suh, Y. S. Lee, Y. W. Kim, and J. S. Lee, "Considerations of blood properties, outlet boundary conditions and energy loss approaches in computational fluid dynamics modeling," *Neurointervention*, vol. 9, no. 1, pp. 1–8, 2014.

[51]   C. D. Murray, "The physiological principle of minimum work: I. The vascular system and the cost of blood volume," *Procedings Natl. Acad. Sci.*, vol. 12, no. 3, pp. 207–214, 1926.

[52]   C. A. Taylor, T. A. Fonte, and J. K. Min, "Computational fluid dynamics applied to cardiac computed tomography for noninvasive quantification of fractional flow reserve: Scientific basis," *J. Am. Coll. Cardiol.*, vol. 61, no. 22, pp. 2233–2241, 2013.

[53]   P. E. Vincent, A. M. Plata, A. A. E. Hunt, P. D. Weinberg, and S. J. Sherwin, "Blood flow in the rabbit aortic arch and descending thoracic aorta," *J. R. Soc. Interface*, vol. 8, no. 65, pp. 1–12, 2011.

[54]   V. Peiffer, E. M. Rowland, S. G. Cremers, P. D. Weinberg, and S. J. Sherwin,

"Effect of aortic taper on patterns of blood flow and wall shear stress in rabbits: association with age.," *Atherosclerosis*, vol. 223, no. 1, pp. 114–121, Jul. 2012.

[55] N. Shahcheraghi, H. A. Dwyer, A. . Cheer, A. . Barakat, and T. Rutaganira, "Unsteady and three-dimensional simulation of blood flow in the human aortic arch," *J. Biomech. Eng.*, vol. 124, no. 4, pp. 378–387, 2002.

[56] V. Peiffer, S. J. Sherwin, and P. D. Weinberg, "Computation in the rabbit aorta of a new metric - the transverse wall shear stress - to quantify the multidirectional character of disturbed blood flow," *J. Biomech.*, vol. 46, no. 15, pp. 2651–2658, Oct. 2013.

[57] A. I. Barakat, R. P. Marini, and C. K. Colton, "Measurement of flow rates through aortic branches in the anesthetized rabbit.," *Lab. Anim. Sci.*, vol. 47, no. 2, pp. 184–189, 1997.

[58] N. Westerhof, J. W. Lankhaar, and B. E. Westerhof, "The arterial windkessel," *Med. Biol. Eng. Comput.*, vol. 47, no. 2, pp. 131–141, 2009.

[59] M. Capoccia, "Development and characterization of the arterial windkessel and its role during left ventricular assist device assistance," *Artif. Organs*, vol. 39, no. 8, pp. E138–E153, 2015.

[60] T. A. S. Kaufmann, K. C. Wong, T. Schmitz-Rode, and U. Steinseifer, "Mimicking of cerebral autoregulation by flow-dependent cerebrovascular resistance: A feasibility study," *Artif. Organs*, vol. 36, no. 4, pp. E97-101, Apr. 2012.

[61] A. G. Brown, Y. Shi, A. Marzo, C. Staicu, I. Valverde, P. Beerbaum, P. V. Lawford, and D. R. Hose, "Accuracy vs. computational time: Translating aortic simulations to the clinic," *J. Biomech.*, vol. 45, no. 3, pp. 516–523, 2012.

[62] J. F. LaDisa, Jr., C. Alberto Figueroa, I. E. Vignon-Clementel, H. Jin Kim, N. Xiao, L. M. Ellwein, F. P. Chan, J. A. Feinstein, and C. A. Taylor, "Computational simulations for aortic coarctation: representative results from a sampling of patients," *J. Biomech. Eng.*, vol. 133, no. 9, p. 91008, 2011.

[63] J. F. J. LaDisa, R. J. Dholakia, A. C. Figueroa, I. E. Vignon-clementel, F. P. Chan, M. M. Samyn, J. R. Cava, C. A. Taylor, and J. A. Feinstein, "Computational simulations demonstrate altered wall shear stress in aortic coarctation patients treated by resection with end-to-end anastomosis," *Congential Hear. Dis.*, vol. 6,

no. 5, pp. 432–443, 2011.

[64]   J. Alastruey, N. Xiao, H. Fok, T. Schaeffter, and C. A. Figueroa, "On the impact of modelling assumptions in multi-scale, subject-specific models of aortic haemodynamics," *J. R. Soc. Interface*, vol. 13, no. 119, pp. 1–17, 2016.

[65]   M. Rojczyk, Z. Ostrowski, W. Adamczyk, B. Melka, D. Bandoła, M. Gracka, A. Knopek, A. Golda, and A. J. Nowak, "CFD analysis of blood flow within aorta of patient with coarctation of aorta," *J. Phys. Conf. Ser.*, vol. 37, no. 3A, pp. 43–55, 2016.

[66]   W. Yang, J. A. Feinstein, and I. E. Vignon-Clementel, "Adaptive outflow boundary conditions improve post-operative predictions after repair of peripheral pulmonary artery stenosis," *Biomech. Model. Mechanobiol.*, vol. 15, no. 5, pp. 1–9, 2016.

[67]   V. Gostuski, I. Pastore, G. R. Palacios, G. V. Diez, H. M. Moscoso-Vasquez, and M. Risk, "Time domain estimation of arterial parameters using the Windkessel model and the Monte Carlo method," *J. Phys. Conf. Ser.*, vol. 705, no. 1, p. 12028, 2016.

[68]   G. Arbia, I. Vignon-Clementel, T.-Y. Hsia, and J.-F. Gerbeau, "Modified Navier-Stokes equations for the outflow boundary conditions in hemodynamics," *Eur. J. Mech. - B/Fluids*, vol. 60, pp. 175–188, 2016.

[69]   M. Catanho, "Model of Aortic Blood Flow Using the Windkessel Effect," 2012.

[70]   P. Segers, E. R. Rietzschel, M. L. De Buyzere, N. Stergiopulos, N. Westerhof, L. M. Van Bortel, T. Gillebert, and P. R. Verdonck, "Three-and-four-element Windkessel models: Assessment of their fitting performance in a large cohort of healthy middle-aged individuals," *Proc. Inst. Mech. Eng. Part H J. Eng. Med.*, vol. 222, no. 4, pp. 417–428, 2008.

[71]   A. Keshmiri and K. Andrews, "Vascular flow modelling using computational fluid dynamics," in *Handbook of Vascular Biology Techniques*, M. Slevin and G. McDowell, Eds. Springer Netherlands, 2015, pp. 343–361.

[72]   D. A. Steinman, "Image-based computational fluid dynamics: A new paradigm for monitoring hemodynamics and atherosclerosis," *Curr. Drug Targets - Cardiovasc. Haematol. Disord.*, vol. 4, no. 2, pp. 183–197, 2004.

[73]   J. P. Archie, S. Hyun, C. Kleinstreuer, P. W. Longest, G. A. Truskey, and J. R. Buchanan, "Hemodynamic parameters and early intimal thickening in branching blood vessels," *Critical Reviews in Biomedical Engineering*, vol. 29, no. 1. pp. 1–64, 2001.

[74]   A. Keshmiri, A. Ruiz-Soler, M. McElroy, and F. Kabinejadian, "Numerical investigation on the geometrical effects of novel graft designs for peripheral artery bypass surgery," *Procedia CIRP*, vol. 49, pp. 147–152, 2016.

[75]   D. N. Ghista and F. Kabinejadian, "Coronary artery bypass grafting hemodynamics and anastomosis design: a biomedical engineering review," *Biomed. Eng. Online*, vol. 12, no. 129, pp. 1–28, Jan. 2013.

[76]   H. Samady, P. Eshtehardi, M. C. McDaniel, J. Suo, S. S. Dhawan, C. Maynard, L. H. Timmins, A. A. Quyyumi, and D. P. Giddens, "Coronary artery wall shear stress is associated with progression and transformation of atherosclerotic plaque and arterial remodeling in patients with coronary artery disease," *Circulation*, vol. 124, no. 7, pp. 779–788, 2011.

[77]   S.-W. Lee, L. Antiga, and D. A. Steinman, "Correlations among indicators of disturbed flow at the normal carotid bifurcation," *J. Biomech. Eng.*, vol. 131, no. 6, p. 061013/7, Jun. 2009.

[78]   X. He and D. N. Ku, "Pulsatile flow in the human left coronary artery bifurcation: Average conditions," *J. Biomech. Eng.*, vol. 118, no. 1, pp. 74–82, 1996.

[79]   L. H. Timmins, D. S. Molony, P. Eshtehardi, C. Mcdaniel, J. N. Oshinski, D. P. Giddens, and H. Samady, "Oscillatory wall shear stress is a dominant flow characteristic affecting lesion progression patterns and plaque vulnerability in patients with coronary artery disease," *J. R. Soc. Interface*, vol. 14, no. 127, p. 20160972, 2017.

[80]   J. D. Hellums, "Whitaker lecture: Biorheology in thrombosis research," *Ann. Biomed. Eng.*, vol. 22, no. 5, pp. 445–455, 1993.

[81]   J. M. Ramstack, L. Zuckerman, and L. F. Mockros, "Shear-induced activation of platelets," *J. Biomech.*, vol. 12, no. 2, pp. 113–125, 1979.

[82]   L. J. Wurzinger, R. Opitz, and H. Eckstein, "Mechanical bloodtrauma. An overview," *Angeiologie*, vol. 38, no. 3, pp. 81–97, 1986.

[83] L. Wurzinger, R. Optiz, M. Wolf, and H. Schmid-Schonbein, "Shear induced platelet activation - A critical reappraisal," *Biorheology*, vol. 22, no. 5, pp. 399–413, 1985.

[84] S. Cito, M. D. Mazzeo, and L. Badimon, "A review of macroscopic thrombus modeling methods," *Thromb. Res.*, vol. 131, no. 2, pp. 116–124, 2013.

[85] K. S. Cunningham and A. I. Gotlieb, "The role of shear stress in the pathogenesis of atherosclerosis," *Lab. Investig.*, vol. 85, no. 1, pp. 9–23, 2005.

[86] G. Janiga, P. Berg, S. Sugiyama, K. Kono, and D. A. Steinman, "The computational fluid dynamics rupture challenge 2013 — Phase I : Prediction of rupture status in intracranial aneurysms," *Am. J. Neuroradiol.*, vol. 36, no. 3, pp. 530–536, 2015.

[87] C. G. Caro, J. M. Fitz-Gerald, and R. C. Schroter, "Atheroma and arterial wall shear observation, correlation and proposal of a shear dependent mass transfer mechanism for atherogenesis," *Proc. R. Soc. London. Ser. B. Biol. Sci.*, vol. 177, no. 1046, pp. 109–159, 1971.

[88] D. N. Ku, D. P. Giddens, C. K. Zarins, and S. Glagov, "Pulsatile flow and atherosclerosis in the human carotid bifurcation. Positive correlation between plaque location and low oscillating shear stress," *Arterioscler. Thromb. Vasc. Biol.*, vol. 5, no. 3, pp. 293–302, May 1985.

[89] U. Olgac, D. Poulikakos, S. C. Saur, H. Alkadhi, and V. Kurtcuoglu, "Patient-specific three-dimensional simulation of LDL accumulation in a human left coronary artery in its healthy and atherosclerotic states.," *Am. J. Physiol. Heart Circ. Physiol.*, vol. 296, pp. H1969–H1982, 2009.

[90] H. A. Himburg, D. M. Grzybowski, A. L. Hazel, J. A. LaMack, X.-M. Li, and M. H. Friedman, "Spatial comparison between wall shear stress measures and porcine arterial endothelial permeability," *Am. J. Physiol. - Hear. Circ. Physiol.*, vol. 286, no. 5, pp. H1916–H1922, 2004.

[91] Y. Hoi, Y. Q. Zhou, X. Zhang, R. M. Henkelman, and D. A. Steinman, "Correlation between local hemodynamics and lesion distribution in a novel aortic regurgitation murine model of atherosclerosis," *Ann. Biomed. Eng.*, vol. 39, no. 5, pp. 1414–1422, 2011.

[92] Z. Cheng, C. Riga, J. Chan, M. Hamady, N. B. Wood, N. J. W. Cheshire, Y. Xu, and R. G. J. Gibbs, "Initial findings and potential applicability of computational simulation of the aorta in acute type B dissection," *J. Vasc. Surg.*, vol. 57, no. 2 Suppl, p. 35S–43S, 2013.

[93] P. G. Menon, J. F. Antaki, A. Undar, and K. Pekkan, "Aortic outflow cannula tip design and orientation impacts cerebral perfusion during pediatric cardiopulmonary bypass procedures," *Ann. Biomed. Eng.*, vol. 41, no. 12, pp. 2588–2602, Dec. 2013.

[94] T. A. S. Kaufmann, M. Hormes, M. Laumen, D. L. Timms, T. Linde, T. Schmitz-Rode, A. Moritz, O. Dzemali, and U. Steinseifer, "The impact of aortic/subclavian outflow cannulation for cardiopulmonary bypass and cardiac support: A computational fluid dynamics study.," *Artif. Organs*, vol. 33, no. 9, pp. 727–732, Sep. 2009.

[95] M. Laumen, T. Kaufmann, D. Timms, P. Schlanstein, S. Jansen, S. Gregory, K. C. Wong, T. Schmitz-Rode, and U. Steinseifer, "Flow analysis of ventricular assist device inflow and outflow cannula positioning using a naturally shaped ventricle and aortic branch," *Artif. Organs*, vol. 34, no. 10, pp. 798–806, Oct. 2010.

[96] A. J. Boyle, U. P. Jorde, B. Sun, S. J. Park, C. A. Milano, O. H. Frazier, K. S. Sundareswaran, D. J. Farrar, and S. D. Russell, "Pre-operative risk factors of bleeding and stroke during left ventricular assist device support: An analysis of more than 900 heartmate II outpatients," *J. Am. Coll. Cardiol.*, vol. 63, no. 9, pp. 880–888, 2014.

[97] B. P. Griffith, R. L. Kormos, H. S. Borovetz, K. Litwak, J. F. Antaki, V. L. Poirier, and K. C. Butler, "HeartMate II left ventricular assist system: from concept to first clinical use," *Ann. Thorac. Surg.*, vol. 71, no. 3, pp. S116–S120, Mar. 2001.

[98] S. Cito, A. J. Geers, M. P. Arroyo, V. R. Palero, J. Pallarés, A. Vernet, J. Blasco, L. San Román, W. Fu, A. Qiao, G. Janiga, Y. Miura, M. Ohta, M. Mendina, G. Usera, and a. F. Frangi, "Accuracy and reproducibility of patient-specific hemodynamic models of stented intracranial aneurysms: Report on the virtual intracranial stenting challenge 2011," *Ann. Biomed. Eng.*, vol. 43, no. 1, pp. 154–167, 2015.

[99] S. Cito, J. Pallarés, and A. Vernet, "Sensitivity analysis of the boundary conditions

in simulations of the flow in an aortic coarctation under rest and stress conditions," in *Statistical Atlases and Computational Models of the Heart. Imaging and Modelling Challenges*, vol. 8330, Springer Berlin Heidelberg, 2014, pp. 74–82.

[100] U. Morbiducci, D. Gallo, D. Massai, F. Consolo, R. Ponzini, L. Antiga, C. Bignardi, M. a Deriu, and A. Redaelli, "Outflow conditions for image-based hemodynamic models of the carotid bifurcation: Implications for indicators of abnormal flow.," *J. Biomech. Eng.*, vol. 132, no. 9, p. 91005, 2010.

[101] U. Morbiducci, R. Ponzini, D. Gallo, C. Bignardi, and G. Rizzo, "Inflow boundary conditions for image-based computational hemodynamics: Impact of idealized versus measured velocity profiles in the human aorta," *J. Biomech.*, vol. 46, no. 1, pp. 102–109, 2013.

[102] D. Gallo, G. De Santis, F. Negri, D. Tresoldi, R. Ponzini, D. Massai, M. A. Deriu, P. Segers, B. Verhegghe, G. Rizzo, and U. Morbiducci, "On the use of in vivo measured flow rates as boundary conditions for image-based hemodynamic models of the human aorta: Implications for indicators of abnormal flow," *Ann. Biomed. Eng.*, vol. 40, no. 3, pp. 729–741, 2012.

[103] A. Quarteroni, A. Veneziani, and C. Vergara, "Geometric multiscale modeling of the cardiovascular system, between theory and practice," *Comput. Methods Appl. Mech. Eng.*, vol. 302, no. 1, pp. 193–252, 2016.

[104] Y. Shi, P. Lawford, and R. Hose, "Review of zero-D and 1-D models of blood flow in the cardiovascular system," *Biomed. Eng. Online*, vol. 10, no. 1, p. 33, 2011.

[105] E. K. Shang, D. P. Nathan, R. M. Fairman, J. E. Bavaria, R. C. Gorman, J. H. Gorman, and B. M. Jackson, "Use of computational fluid dynamics studies in predicting aneurysmal degeneration of acute type B aortic dissections," *J. Vasc. Surg.*, vol. 62, no. 2, pp. 279–284, 2015.

[106] C. Karmonik, S. Partovi, M. Loebe, B. Schmack, A. Ghodsizad, M. R. Robbin, G. P. Noon, K. Kallenbach, M. Karck, M. G. Davies, A. B. Lumsden, and A. Ruhparwar, "Influence of LVAD cannula outflow tract location on hemodynamics in the ascending aorta: A patient-specific computational fluid dynamics approach.," *ASAIO J.*, vol. 58, no. 6, pp. 562–567, 2012.

[107] C. Karmonik, S. Partovi, M. Loebe, B. Schmack, A. Weymann, A. Lumsden, M. Karch, and A. Ruhparwar, "Computational fluid dynamics in patients with

continuous-flow left ventricular assist device support show hemodynamic alterations in the ascending aorta," *J. Thorac. Cardiovasc. Surg.*, vol. 147, no. 4, pp. 1326–1333, 2014.

[108] F. Kabinejadian, M. McElroy, A. Ruiz-Zoler, H. L. Leo, M. Slevin, L. Badimon, and A. Keshmiri, "Numerical assessment of novel helical/spiral grafts with improved hemodynamics for distal graft anastomoses," *PLoS One*, vol. 11, no. 11, p. e0165892, 2016.

[109] M. McElroy, A. Ruiz-Soler, and A. Keshmiri, "Left ventricular assist devices: Impact of flow ratios on the localisation of cardiovascular diseases using computational fluid dynamics," *Procedia CIRP*, vol. 49, no. 1, pp. 163–169, 2016.

[110] J. Alastruey, J. H. Siggers, V. Peiffer, D. J. Doorly, and S. J. Sherwin, "Reducing the data: Analysis of the role of vascular geometry on blood flow patterns in curved vessels," *Phys. Fluids*, vol. 24, no. 3, p. 031902/24, 2012.

[111] J. E. Moore Jr, S. E. Maier, D. N. Ku, and P. Boesiger, "Hemodynamics in the abdominal aorta: A comparison of in vitro and in vivo measurements," *J. Appl. Physiol.*, vol. 76, no. 4, pp. 1520–1527, Apr. 1994.

[112] F. Kabinejadian and D. N. Ghista, "Compliant model of a coupled sequential coronary arterial bypass graft: effects of vessel wall elasticity and non-newtonian rheology on blood flow regime and hemodynamic parameters distribution," *Med. Eng. Phys.*, vol. 34, no. 7, pp. 860–872, Sep. 2012.

[113] A. P. Avolio, M. F. O'rourke, K. Mang, P. T. Bason, and B. S. Gow, "A comparative study of pulsatile arterial hemodynamics in rabbits and guinea pigs.," *Am. J. Physiol.*, vol. 230, no. 4, pp. 868–875, 1976.

[114] S. G. Cremers, S. J. Wolffram, and P. D. Weinberg, "Atheroprotective effects of dietary L-arginine increase with age in cholesterol-fed rabbits.," *Br. J. Nutr.*, vol. 105, no. 10, pp. 1439–1447, 2011.

[115] J. Xiang, A. H. Siddiqui, and H. Meng, "The effect of inlet waveforms on computational hemodynamics of patient-specific intracranial aneurysms," *J. Biomech.*, vol. 47, no. 16, pp. 3882–3890, 2014.

[116] A. J. Geers, I. Larrabide, H. G. Morales, and A. F. Frangi, "Comparison of steady-state and transient blood flow simulations of intracranial aneurysms.," in

Engineering in Medicine and Biology Society: 32nd Annual International Conference of the IEEE, 2010, pp. 2622–2625.

[117] T. Du, D. Hu, and D. Cai, "Outflow boundary conditions for blood flow in arterial trees," *PLoS One*, vol. 10, no. 5, p. e0128597, 2015.

[118] K. Lagana, G. Dubini, F. Migliavacca, R. Pietrabissa, G. Pennati, A. Veneziani, and A. Quarteroni, "Multiscale modelling as a tool to prescribe realistic boundary conditions for the study of surgical procedures," *Biorheology*, vol. 39, no. 3,4, pp. 359–364, 2002.

[119] A. Kazakidi, S. J. Sherwin, and P. D. Weinberg, "Effect of reynolds number and flow division on patterns of haemodynamic wall shear stress near branch points in the descending thoracic aorta," *J. R. Soc. Interface*, vol. 6, no. 35, pp. 539–548, 2008.

[120] A. F. Osorio, R. Osorio, A. Ceballos, R. Tran, W. Clark, E. A. Divo, I. R. Argueta-Morales, A. J. Kassab, and W. M. DeCampli, "Computational fluid dynamics analysis of surgical adjustment of left ventricular assist device implantation to minimise stroke risk," *Comput. Methods Biomech. Biomed. Engin.*, vol. 16, no. 6, pp. 622–638, 2013.

[121] A. K. Menon, A. Götzenich, H. Sassmannshausen, M. Haushofer, R. Autschbach, and J. W. Spillner, "Low stroke rate and few thrombo-embolic events after HeartMate II implantation under mild anticoagulation," *Eur. J. Cardio-Thoracic Surg.*, vol. 42, no. 2, pp. 319–323, 2012.

[122] T. A. S. Kaufmann, P. Schlanstein, A. Moritz, and U. Steinseifer, "Development of a hemodynamically optimized outflow cannula for cardiopulmonary bypass," *Artif. Organs*, vol. 38, no. 11, pp. 972–978, Feb. 2014.

[123] J. K. White, A. Jagannath, J. Titus, R. Yoneyama, J. Madsen, and A. K. Agnihotri, "Funnel-tipped aortic cannula for reduction of atheroemboli," *Ann. Thorac. Surg.*, vol. 88, no. 2, pp. 551–557, Aug. 2009.

[124] P. G. Menon, N. Teslovich, C.-Y. Chen, A. Undar, and K. Pekkan, "Characterization of neonatal aortic cannula jet flow regimes for improved cardiopulmonary bypass," *J. Biomech.*, vol. 46, no. 2, pp. 362–372, Jan. 2013.

[125] K. May-Newman, B. Hillen, and W. Dembitsky, "Effect of left ventricular assist

device outflow conduit anastomosis location on flow patterns in the native aorta.," *Am. Soc. Artif. Intern. Organs*, vol. 52, no. 2, pp. 132–139, 2006.

[126] K. D. May-Newman, B. K. Hillen, C. S. Sironda, and W. Dembitsky, "Effect of LVAD outflow conduit insertion angle on flow through the native aorta.," *J. Med. Eng. Technol.*, vol. 28, no. 3, pp. 105–109, 2004.

[127] J. Bhama, C. Eckert, K. Lockard, A. Shiose, C. Bermudez, J. Teuteberg, R. Ramani, M. Simon, V. Badhwar, and R. Kormos, "Does LVAD inflow cannula position contribute to the development of pump thrombosis requiring device exchange?," *J. Am. Coll. Cardiol.*, vol. 61, no. 10, p. E719, Mar. 2013.

[128] K. A. Ammar, M. M. Umland, C. Kramer, N. Sulemanjee, M. F. Jan, B. K. Khandheria, J. B. Seward, and T. E. Paterick, "The ABCs of left ventricular assist device echocardiography : a systematic approach," *Eur. Hear. J. – Cardiovasc. Imaging*, vol. 13, no. 11, pp. 885–899, 2012.

[129] M. Dalby, N. Banner, P. Tansley, L. Grieve, J. Partridge, and M. Yacoub, "Left ventricular function during support with an asynchronous pulsatile left ventricular assist device," *J. Hear. Lung Transplant.*, vol. 22, no. 3, pp. 292–300, 2003.

[130] C. Karmonik, S. Partovi, B. Schmack, A. Weymann, M. Loebe, G. P. Noon, P. Piontek, M. Karck, A. B. Lumsden, and A. Ruhparwar, "Comparison of hemodynamics in the ascending aorta between pulsatile and continuous flow left ventricular assist devices using computational fluid dynamics based on computed tomography images," *Artif. Organs*, vol. 38, no. 2, pp. 142–148, Feb. 2014.

[131] C. Ong, S. Dokos, B. Chan, E. Lim, A. Al Abed, N. A. Bin Abu Osman, S. Kadiman, and N. H. Lovell, "Numerical investigation of the effect of cannula placement on thrombosis," *Theor. Biol. Med. Model.*, vol. 10, no. 35, pp. 1–14, Jan. 2013.

[132] A. Assmann, A. Benim, G. Fethi, P. Lux, P. Akhyari, U. Boeken, F. Joos, P. Feindt, and A. Lichtenberg, "Pulsatile extracorporeal circulation during on-pump cardiac surgery enhances aortic wall shear stress," *J. Biomech.*, vol. 45, no. 1, pp. 156–163, 2012.

[133] M. Brandfonbrener, M. Landowne, and N. W. Shock, "Changes in cardiac output with age.," *Circulation*, vol. 12, no. 4, pp. 557–566, 1955.

[134] J. Garbade, H. B. Bittner, M. J. Barten, and F. Mohr, "Current trends in implantable left ventricular assist devices," *Cardiol. Res. Pract.*, vol. 2011, no. Article ID 290561, pp. 1–9, 2011.

[135] A. C. W. Baldwin, E. Sandoval, G. V Letsou, H. R. Mallidi, W. E. Cohn, and O. H. Frazier, "Surgical approach to continuous-flow left ventricular assist device explantation: A comparison of outcomes," *J. Thorac. Cardiovasc. Surg.*, vol. 151, no. 1, pp. 192–198, 2015.

[136] L. A. Smith, L. T. Yarboro, and J. L. W. Kennedy, "Left ventricular assist device implantation strategies and outcomes," *J. Thorac. Dis.*, vol. 7, no. 12, pp. 2088–2096, 2015.

[137] T. A. S. Kaufmann, S. D. Gregory, M. R. Busen, G. D. Tansley, and U. Steinseifer, "Development of a numerical pump testing framework," *Artif. Organs*, vol. 38, no. 9, pp. 783–790, 2014.

[138] W. D. Clark, B. A. Eslahpazir, I. R. Argueta-Morales, A. J. Kassab, E. A. Divo, and W. M. DeCampli, "Comparison between bench-top and computational modelling of cerebral thromboembolism in ventricular assist device circulation," *Cardiovasc. Eng. Technol.*, vol. 6, no. 3, pp. 242–255, 2015.

[139] M. B. Farag, C. Karmonik, F. Rengier, M. Loebe, M. Karck, H. von Tengg-Kobligk, A. Ruhparwar, and S. Partovi, "Review of recent results using computational fluid dynamics simulations in patients receiving mechanical assist devices for end-stage heart failure," *Methodist Debakey Cardiovasc. J.*, vol. 10, no. 3, pp. 185–189, 2014.

[140] F. Iori, L. Grechy, R. W. Corbett, W. Gedroyc, N. Duncan, C. G. Caro, and P. E. Vincent, "The effect of in-plane arterial curvature on blood flow and oxygen transport in arterio-venous fistulae," *Phys. Fluids*, vol. 27, no. 3, p. 31903, 2015.

[141] X. Liu, A. Sun, Y. Fan, and X. Deng, "Physiological significance of helical flow in the arterial system and its potential clinical applications," *Ann. Biomed. Eng.*, vol. 43, no. 1, pp. 3–15, Aug. 2014.

[142] R. Hobbs and A. Boyle, "Disease Management," *Cleveland Clinic*, 2014. [Online]. Available: http://www.clevelandclinicmeded.com/medicalpubs/diseasemanagement/cardiology/heart-failure/.

[143] J. F. Viles-Gonzalez, V. Fuster, and J. J. Badimon, "Atherothrombosis: A widespread disease with unpredictable and life-threatening consequences," *Eur. Heart J.*, vol. 25, no. 14, pp. 1197–1207, 2004.

[144] M. J. Davies and A. C. Thomas, "Plaque fissuring - The cause of acute myocardial infarction, sudden ischaemic death, and crescendo angina.," *Br. Heart J.*, vol. 53, no. 4, pp. 363–373, 1985.

[145] R. Virmani, F. D. Kolodgie, A. P. Burke, A. Farb, and S. M. Schwartz, "Lessons from sudden coronary death: A comprehensive morphological classification scheme for atherosclerotic lesions," *Atheroscler. Thromb. Vasc. Biol.*, vol. 20, no. 5, pp. 1262–1275, 2000.

[146] E. Falk, "Plaque rupture with severe pre-existing stenosis precipitating coronary thrombosis. Characteristics ofcoronary atherosclerotic plaques underlying fatal occlusive thrombi," *Br. Heart J.*, vol. 50, no. 2, pp. 127–134, 1983.

[147] T. Kubo, T. Imanishi, S. Takarada, A. Kuroi, S. Ueno, T. Yamano, T. Tanimoto, Y. Matsuo, T. Masho, H. Kitabata, K. Tsuda, Y. Tomobuchi, and T. Akasaka, "Assessment of culprit lesion morphology in acute myocardial infarction. ability of optical coherence tomography compared with intravascular ultrasound and coronary angioscopy," *J. Am. Coll. Cardiol.*, vol. 50, no. 10, pp. 933–939, 2007.

[148] D. A. Bluemke, S. Achenbach, M. Budoff, T. C. Gerber, B. Gersh, L. D. Hillis, W. G. Hundley, W. J. Manning, B. F. Printz, M. Stuber, and P. K. Woodard, "Noninvasive coronary artery imaging magnetic resonance angiography and multidetector computed tomography angiography," *Circulation*, vol. 118, no. 5, pp. 586–606, 2008.

[149] G. S. Mintz, "Clinical utility of intravascular imaging and physiology in coronary artery disease," *J. Am. Coll. Cardiol.*, vol. 64, no. 2, pp. 207–222, 2014.

[150] C. J. Slager, J. J. Wentzel, J. C. H. Schuurbiers, J. A. F. Oomen, J. Kloet, R. Krams, C. Von Birgelen, W. J. Van Der Giessen, P. W. Serruys, and P. J. De Feyter, "True 3-dimensional reconstruction of coronary arteries in patients by fusion of angiography and IVUS (ANGUS) and its quantitative validation," *Circulation*, vol. 102, no. 5, pp. 511–517, 2000.

[151] L. H. Timmins, D. S. Molony, P. Eshtehardi, M. C. McDaniel, J. N. Oshinski, H. Samady, and D. P. Giddens, "Focal association between wall shear stress and

clinical coronary artery disease progression," *Ann. Biomed. Eng.*, vol. 43, no. 1, pp. 94–106, 2014.

[152] M. Laban, J. A. Oomen, C. J. Slager, J. J. Wentzel, R. Krams, J. C. H. Schuurbiers, A. den Beer, C. von Birgelen, P. W. Serruys, and P. J. de Feijter, "ANGUS: A new approach to three-dimensional reconstruction of coronary vessels by combined use of angiography and intravascular ultrasound," in *Computers in Cardiology 1995*, 1995, vol. 95, pp. 325–328.

[153] A. Wahle, P. M. Prause, S. C. DeJong, and M. Sonka, "Geometrically correct 3-D reconstruction of intravascular ultrasound images by fusion with biplane angiography--methods and validation," *IEEE Trans. Med. Imaging*, vol. 18, no. 8, pp. 686–699, 1999.

[154] R. Waksman, H. Kitabata, F. Prati, M. Albertucci, and G. S. Mintz, "Intravascular ultrasound versus optical coherence tomography guidance," *J. Am. Coll. Cardiol.*, vol. 62, no. 17, pp. S32–S40, 2013.

[155] K. Toutouzas, Y. S. Chatzizisis, M. Riga, A. Giannopoulos, A. P. Antoniadis, S. Tu, Y. Fujino, D. Mitsouras, C. Doulaverakis, I. Tsampoulatidis, V. G. Koutkias, K. Bouki, Y. Li, I. Chouvarda, G. Cheimariotis, N. Maglaveras, I. Kompatsiaris, S. Nakamura, J. H. C. Reiber, F. Rybicki, H. Karvounis, C. Stefanadis, D. Tousoulis, and G. D. Giannoglou, "Accurate and reproducible reconstruction of coronary arteries and endothelial shear stress calculation using 3D OCT: Comparative study to 3D IVUS and 3D QCA," *Atherosclerosis*, vol. 240, no. 2, pp. 510–519, 2015.

[156] J. Ha, J.-S. Kim, J. Lim, G. Kim, S. Lee, J. S. Lee, D.-H. Shin, B.-K. Kim, Y.-G. Ko, D. Choi, Y. Jang, and M.-K. Hong, "Assessing computational fractional flow reserve from optical coherence tomography in patients with intermediate coronary stenosis in the left anterior descending artery," *Circ. Cardiovasc. Interv.*, vol. 9, no. 8, p. e003613, 2016.

[157] H. J. Kim, I. E. Vignon-Clementel, C. A. Figueroa, K. E. Jansen, and C. A. Taylor, "Developing computational methods for three-dimensional finite element simulations of coronary blood flow," *Finite Elem. Anal. Des.*, vol. 46, no. 6, pp. 514–525, 2010.

[158] N. Stergiopulos, P. Segers, and N. Westerhof, "Use of pulse pressure method for

estimating total arterial compliance in vivo," *Am. J. Physiol.*, vol. 276, no. 2, pp. H424–H428, 1999.

[159] S. Lehoux, B. Esposito, R. Merval, and A. Tedgui, "Differential regulation of vascular focal adhesion kinase by steady stretch and pulsatility," *Circulation*, vol. 111, no. 5, pp. 643–649, 2005.

[160] D. Lu and G. S. Kassab, "Role of shear stress and stretch in vascular mechanobiology," *J. R. Soc. Interface*, vol. 8, no. 63, pp. 1379–1385, 2011.

[161] C. K. Thodeti, B. Matthews, A. Ravi, A. Mammoto, K. Ghosh, A. L. Bracha, and D. E. Ingber, "TRPV4 channels mediate cyclic strain-induced endothelial cell reorientation through integrin-to-integrin signaling," *Circ. Res.*, vol. 104, no. 9, pp. 1123–1130, 2009.

[162] E. Wellnhofer, L. Goubergrits, U. Kertzscher, and K. Affeld, "In-vivo coronary flow profiling based on biplane angiograms: influence of geometric simplifications on the three-dimensional reconstruction and wall shear stress calculation," *Biomed. Eng. Online*, vol. 5, no. 1, p. 39, Jan. 2006.

[163] C. V. Bourantas, H. M. Garcia-Garcia, R. Torii, Y.-J. Zhang, M. Westwood, T. Crake, and P. W. Serruys, "Vulnerable plaque detection: an unrealistic quest or a feasible objective with a clinical value?," *Heart*, vol. 102, no. 8, pp. 581–589, 2016.

[164] D. Barber and D. Hose, "Automatic segmentation of medical images using image registration: Diagnostic and simulation applications," *J. Med. Eng. Technol.*, vol. 29, no. 2, pp. 53–63, 2005.

[165] F. Zhao and X. Xie, "An verview of interactive medical image segmentation," *Ann. BMVA*, vol. 2013, no. 7, pp. 1–22, 2013.

[166] J. S. Coogan, J. D. Humphrey, and C. A. Figueroa, "Computational simulations of hemodynamic changes within thoracic, coronary, and cerebral arteries following early wall remodeling in response to distal aortic coarctation," *Biomech. Model. Mechanobiol.*, vol. 12, no. 1, pp. 79–93, 2013.

[167] A. L. Marsden, Y. Bazilevs, C. C. Long, and M. Behr, "Recent advances in computational methodology for simulation of mechanical circulatory assist devices," *Wiley Interdiscip. Rev. Syst. Biol. Med.*, vol. 6, no. 2, pp. 169–188, 2014.

APPENDIX A

PUBLICATIONS & PRESENTATIONS

Publications

- **M. McElroy**, A. Keshmiri, "Impact of using conventional inlet/outlet boundary conditions on haemodynamic metrics in a subject-specific rabbit aorta," Part H: Journal of Engineering in Medicine, (In press).

- F. Kabinejadian, **M. McElroy**, A. Ruiz-Zoler, H. L. Leo, M. Slevin, L. Badimon, and A. Keshmiri, "Numerical assessment of novel helical/spiral grafts with improved hemodynamics for distal graft anastomoses," *PLoS One*, vol. 11, no. 11, p. e0165892, 2016.

- **M. McElroy**, A. Ruiz-Soler, and A. Keshmiri, "Left ventricular assist devices: Impact of flow ratios on the localisation of cardiovascular diseases using computational fluid dynamics," *Procedia CIRP*, vol. 49, no. 1, pp. 163–169, 2016.

- A. Keshmiri, A. Ruiz-Soler, **M. McElroy**, and F. Kabinejadian, "Numerical investigation on the geometrical effects of novel graft designs for peripheral artery bypass surgery," *Procedia CIRP*, vol. 49, pp. 147–152, 2016.

Presentations

- **M. McElroy**, A. Xenakis, and A. Keshmiri, "Impact of heart failure severity on preoperative planning of ventricular assist device configurations," 5th International Conference on Computational and Mathematical Biomedical Engineering, University of Pittsburgh, Pittsburgh, United States, 10th-12th April, 2017.

- **M. McElroy**, A. Keshmiri, and S. Cito, "Uncertainty quantification of boundary conditions for cfd simulations of a rabbit aorta," Computational Fluid Dynamics in Medicine and Biology II conference, Albufeira, Portugal, 30th August-4th September, 2015.

- **M. McElroy**, "Engineering analysis & development of therapeutic devices for cardiovascular diseases," 7th MMU Post-Graduate Research Conference, Manchester, UK, 4th November, 2014.

- **M. McElroy**, A. Keshmiri, F. Kabinejadian, "Numerical investigation of spiral-induced flow in end-to-side graft anastomosis," Manchester Metropolitan University Research Conference, Manchester, UK, 3rd July, 2014.